INTERFACIAL CHARGE TRANSFER PROCESSES IN QUANTUM DOT SOLAR CELLS

Ph.D. THESIS

by

UPENDRA KUMAR VERMA

**DEPARTMENT OF ELECTRONICS AND COMMUNICATION ENGINEERING
INDIAN INSTITUTE OF TECHNOLOGY ROORKEE
ROORKEE−247 667 (INDIA)
JULY, 2019**

INTERFACIAL CHARGE TRANSFER PROCESSES IN QUANTUM DOT SOLAR CELLS

A THESIS

Submitted in partial fulfilment of the requirements for the award of the degree

of

DOCTOR OF PHILOSOPHY

in

ELECTRONICS AND COMMUNICATION ENGINEERING

by

UPENDRA KUMAR VERMA

DEPARTMENT OF ELECTRONICS AND COMMUNICATION ENGINEERING
INDIAN INSTITUTE OF TECHNOLOGY ROORKEE
ROORKEE−247 667 (INDIA)
JULY, 2019

INDIAN INSTITUTE OF TECHNOLOGY ROORKEE

STUDENT'S DECLARATION

I hereby certify that the work presented in the thesis entitled **"INTERFACIAL CHARGE TRANSFER PROCESSES IN QUANTUM DOT SOLAR CELLS"** is my own work carried out during a period from July, 2014 to August, 2019 under the supervision of Dr. Brijesh Kumar, Assistant Professor, Department of Electronics and Communication Engineering, Indian Institute of Technology Roorkee, Roorkee.

The matter presented in the thesis has not been submitted for the award of any other degree of this or any other Institute.
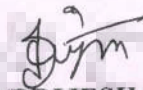
Dated: 30|12|2019

(UPENDRA KUMAR VERMA)

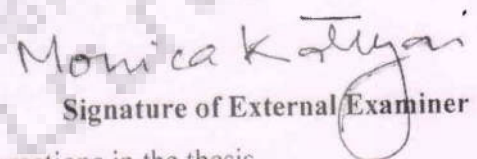## SUPERVISOR'S DECLARATION

This is to certify that the above mentioned work is carried out under my supervision.
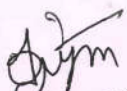
Dated: 30|12|19

(BRIJESH KUMAR)

The Ph.D. Viva-Voce Examination of **Mr. Upendra Kumar Verma**, Research Scholar, has been held on **December 30, 2019.**
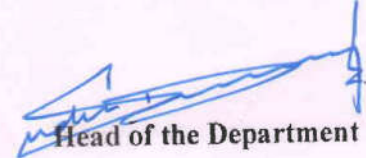
Chairman, SRC

Signature of External Examiner

This is to certify that the student has made all the corrections in the thesis.

Signature of Supervisor
Dated: December 30, 2019

Head of the Department

ABSTRACT

Quantum dots (QDs) are extensively used in photovoltaic devices due to their unique properties: bandgap tunability, capability of multiple exciton generation, up/down wavelength conversion. The improvement in device performance is attributed to the enhancement in optical absorption, quantum efficiency, and reduction in thermalization losses. Good optical, as well as electrical properties of the QDs, are essential for efficient device operation. Charge transport and carrier recombination in the QDs are the key processes that affect the device performance and these processes can be easily tuned during the synthesis of QDs and fabrication of the device.

In this work, current-voltage characteristics in bilayer heterojunction diodes are studied (effects of energy barriers, layer thicknesses, etc.) and separated into three working regimes based on the energy band diagram of the device. Subsequently, a model for multilayer quantum dot organic solar cells has been developed that explores the impact of electronic processes (carrier recombination, tunneling, injection, etc.) in QDs on the current-voltage (J-V) characteristic of the solar cells. Solar cell characteristics can be controlled by the quantum dot layers. The bimolecular recombination coefficient of QDs is a prime factor that controls the open-circuit voltage without any significant reduction in short circuit current. To verify our proposed model, various core-shell QDs have been fabricated and its interlayer is inserted between the donor and acceptor layer in the device. The addition of QDs has improved the optical absorption in the device resulting in an increase in photo-current/short circuit current density and open-circuit voltage of the solar cell but the current-voltage characteristics show an s-shaped curve in the fourth quadrant which results in drastically reduced fill factor. The reason behind the appearance of s-kink in experimentally obtained J-V characteristic of QD solar cells has been analyzed with the model. According to the model, the capture/emission time and tunneling rate coefficient in QDs are individually responsible for degradation in device performance via an undesirable s-shaped J-V characteristic of hybrid organic/inorganic quantum dot solar cells. Thus, injection/extraction rate, tunneling among QDs and recombination in QDs are essential factors that are required to be optimized for efficient QD solar cells. The structural and energetic disorders at various interfaces, surface properties of QDs, fabrication process, etc. must be taken into consideration to achieve an efficient device.

ACKNOWLEDGMENT

TABLE OF CONTENTS

Title	Page No.

Title	Page No.

LIST OF FIGURES

LIST OF TABLES

Chapter 1

Introduction and Literature Review

1. Organic Photovoltaics

A solar cell is a device that converts sunlight into electricity directly. The photovoltaic market has been increasing very rapidly with growing in contribution to the total energy demand of the world. Still, the contribution of solar cell technology to total energy supply is very low due to high cost of energy conversion with solar cell technology as compared to the conventional source of energy. Therefore, new technologies, novel materials instead of conventional materials (silicon, GaAs, etc.) for photovoltaics have been adopted in order to reduce the solar cell production cost. Researchers have moved towards a new technology based on organic materials. Their low-cost and ease of processing of organic devices makes them a promising alternative to the current inorganic technologies. Organic materials have very large absorption coefficient so required thickness of the active layer is reduced to few hundred nanometers which is much less than the thickness of active layer in conventional silicon solar cells. So materials cost is greatly reduced in organic photovoltaics. Using various fabrication techniques, production speeds up to several meters square per second can be achieved. With the roll to roll fabrication process, about 10^5 m^2 of a film can be prepared in a day. The production of organic photovoltaic devices can be achieved in large quantities and is many times cheaper than the conventional inorganic photovoltaic technology. The new generation photovoltaic devices based on organic materials have unique advantages such as large-area production, mechanically flexible substrates, etc [1-5].

Organic photovoltaic (OPV) technology utilizes organic semiconductors. Organic semiconductors show absorption and emission of light in the visible range and conductivity that able to drive various semiconducting devices like light-emitting devices, solar cells, transistors, etc. The molecules in organic solids are weakly bound by Van-der-Waals force. This weak bonding force and low dielectric constant ($< 5\varepsilon_0$) are the key reasons for the strange physical, electrical, and optical properties of the organic semiconductors. Generally, the bandgap of organic semiconductors is in the range of 2-5 eV so intrinsic carrier concentration is negligible at room temperature and electron-hole pairs generated by thermal or optical excitation are bound by Coulomb interaction due to their low dielectric constant. The bound electron-hole

pair is known as exciton and needs additional energy equal to its binding energy which varied from 0.1-1.0 eV for dissociation into free carriers.

1.1. Electrical conductivity in organic semiconductors

Intrinsic carrier concentration in polymer and other organic small molecules is negligible and the materials are insulating in nature. Thus, charge injected from an electrode, intentional/unintentional doping, excess carriers due to photo/thermal excitation, etc. are responsible for electrical conductivity in organic semiconductors. Weak electronic coupling among the organic molecules also causes the absence of continuous energy bands. Hence, charge carriers are localized on organic molecules. These charge carriers move from one molecule to another via hopping mechanism. Delocalized electrons and presence of the conjugated system in the molecule are essential requirements for the conduction of charge in organic semiconductors.

a. Delocalization of electron and conjugation system

According to Pauli's exclusion principle, quantum numbers are redistributed when multiple atoms come closer and closer to form a molecule by combining atomic orbitals to form new orbitals which are called molecular orbitals. The first step to this molecular orbitals formation is hybridization. Each atom participating in molecule formation using covalent bonds undergoes hybridization [6].
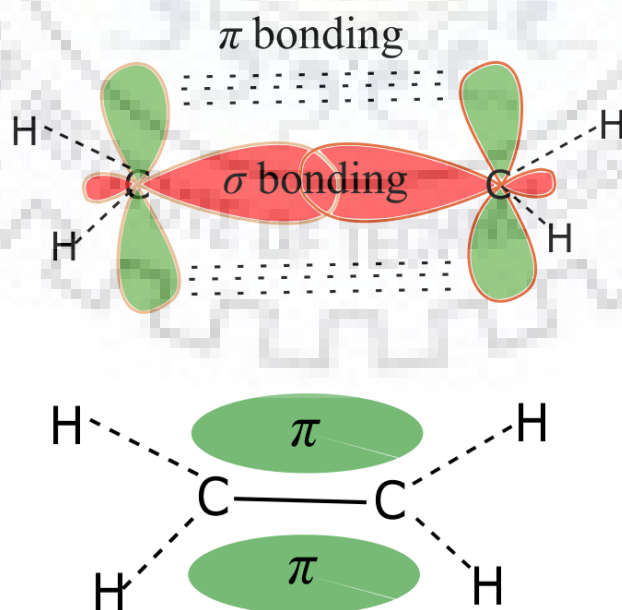
Figure 1.1 σ and π bonding in a C_2H_4 molecule.

In the case of sp^2 hybridization of the carbon atom, it forms three sigma bonds with other carbon atoms. Electrons involved in σ-bond are tightly held compared to the π-bond. This enables electrons in the π-bond to be able to leave the molecule easily under excitation. The π-electron network forms a cloud of electrons as shown in Fig. 1.1. Electrons are free to move in this cloud.

Conduction in organic molecules or polymers is due to the presence of π-bonds in carbon chain with alternating single and double bonds as shown in Fig. 1.2. The conjugation is a necessary condition for organic material to conduct electricity. It allows the circulation of charge across the molecules in a system of multiple molecules bunched together to form an organic solid. The charge on the organic molecule creates structural disorder around it which is known as polaron and acts as a charge carrier in organic semiconductors. The motion is randomly directed in all directions but in the presence of an external electric field applied across the system, it is directed in a specific direction and conducts electricity [7].
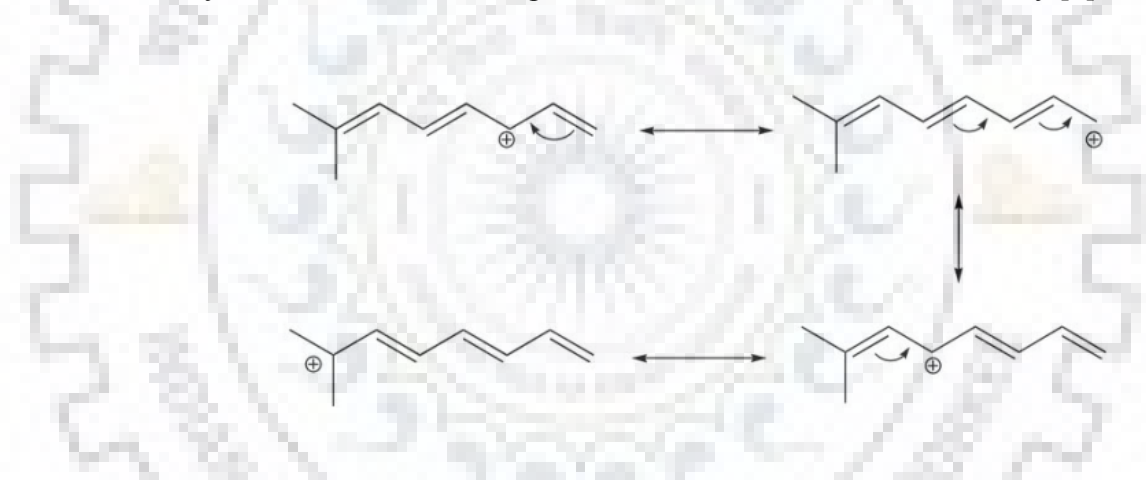
Figure 1.2 Conjugated systems: Movement of π-bonds.

2. Organic Solar Cells

Organic solar cells are achieved by sandwiching the active layer of organic semiconductors between two electrodes of different work functions. This difference in work function provides driving force to the charge transport in the organic solar cells. Depending on the active layer, organic solar cells are classified as single layer, bilayer heterojunction, and bulk heterojunction solar cell. Photovoltaic operation in organic solar cells is slightly different as compared to inorganic solar cells due high binding energy of excitons.

2.1. Working Principle and Current-Voltage Characteristic

In Fig. 1.3 (a), the schematic of bilayer heterojunction solar cell and corresponding energy band diagram are shown. When the device is illuminated with solar spectrum, the

3

photons of sufficient energy are absorbed in the active material (donor) and electrons are excited to first excited state called lowest unoccupied molecular orbital (LUMO) and leave holes at highest occupied molecular orbital (HOMO) level. But, the low dielectric constant of organic semiconductors results in a strong electrical attraction between excited electron and hole instead of generation of free electron and hole. The bound pair of excited electron and hole is called an exciton. These excitons diffuse and reach the interface of donor and acceptor material. The abrupt change in electron affinity at heterojunction causes dissociation of excitons into free carriers. The electron is transferred to the LUMO of acceptor and hole remains at the HOMO of the donor. Now, these free carriers are swept by the electric field created by work function difference of electrode materials, collected at the respective electrode, and generate a current in an external circuit.
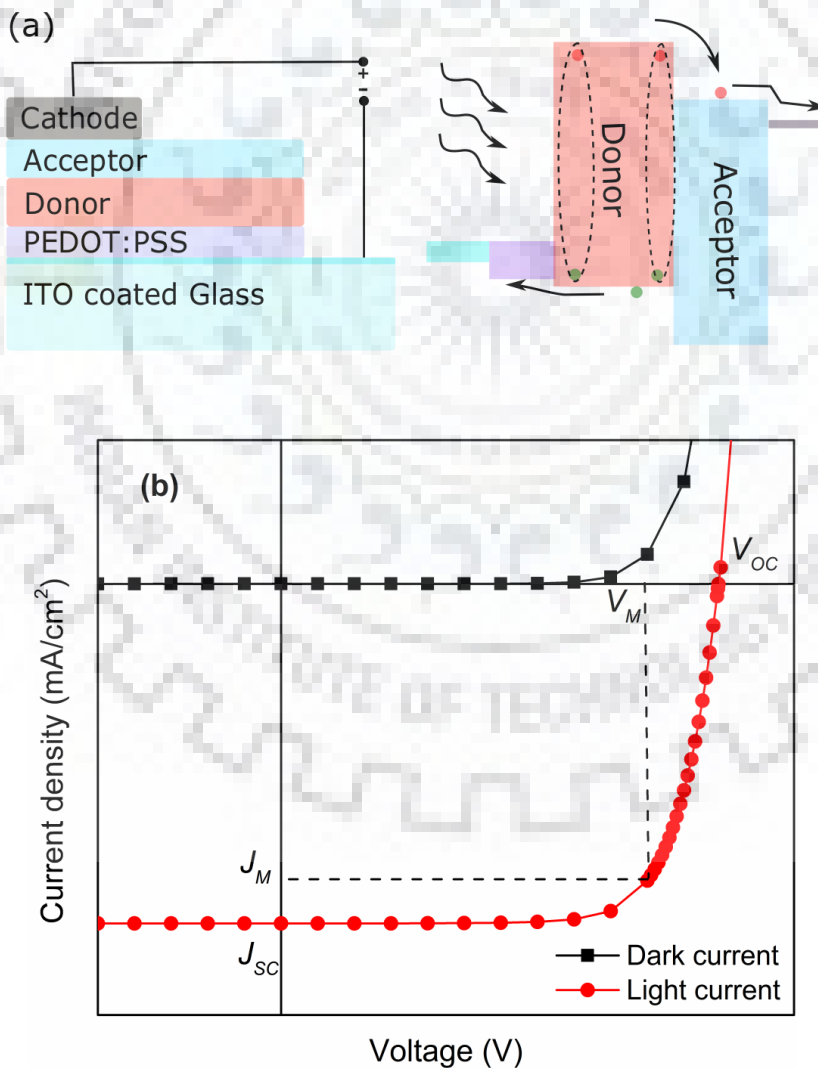
Figure 1.3 (a) Schematic of bilayer heterojunction solar cell and photovoltaic operation (b) current-voltage characteristics under dark and illuminated condition is shown.

The current-voltage characteristic of a solar cell is shown in Fig. 1.3 (b). The current-voltage plot in the dark condition is a diode characteristic. It shifts downward on illuminating the device. The shifting is proportional to the illumination intensity. The terminology used to estimate device performance is known as solar cell parameters. The terms are defined as

- Open-circuit voltage (V_{OC}) is the voltage across the solar cell when the current is zero.
- The short-circuit current (J_{SC}) is the current through the solar cell when voltage across the cell is zero.
- Fill factor (*FF*) is a measure of squareness of the J-V curve of solar cells and defined as:

$$FF = \frac{V_M \times J_M}{V_{OC} \times J_{SC}}$$

- Power conversion efficiency (η) of a solar cell is defined as:

$$\eta = \frac{V_{OC} \times J_{SC} \times FF}{Optical\ power\ (in)}$$

- External quantum efficiency (EQE) is a measure of the fraction of incident photons at a particular wavelength that are collected as free charge carriers at the electrodes.

$$EQE = \frac{No.\ of\ Electrons\ collected\ at\ electrodes}{No.\ of\ incident\ photons}.$$

2.2. Performance Improving Strategies

Organic solar cells (OSCs) in the early days were developed with a single active layer sandwiched between electrodes with different work functions. These devices were exhibit very low (<1%) conversion efficiency. The main reason behind it was poor exciton dissociation efficiency into free carriers. But, the introduction of concept of bilayer heterojunction and bulk heterojunction in the active region improved the device efficiency many times as compared to the single-layer device by improving exciton dissociation efficiency and minimizing the exciton recombination respectively. Thus, improvement in device architecture, fabrication techniques, and use of novel materials are the basic parameters to achieve efficient devices and more than 10% power conversion efficiency has been achieved [8-11].

The performance of an organic solar cell is highly dependent on the interface between the different layers. In organic solar cells, there are mainly two types of interfaces, one, between the organic and electrode material and second, between organic donor and acceptor

5

materials. The interfacial material (inserted between the electrodes and organic layers) plays a major role in charge extraction and stability of the device [12]. The interface between donor and acceptor layer directly affects the exciton dissociation process, geminate and bimolecular recombination process at the heterojunction. So, it should be optimized and its properties should be well understood for the design of high-performance organic solar cells.

Insertion of a high dielectric material layer in OSC improves performance due to improvement in the surface charge accumulation and collection [12]. Hsiao *et al.* performed a C-V analysis on solar cells after inserting a thin film of high dielectric material in solar cells and found a higher surface polarization of dielectric thin film cause a decrease in the surface-charge accumulation at the electrode interface. When they used high dielectric material PFN (poly[(9,9-dioctyl-2,7-fluorene)-alt-(9,9-bis(3′-(N,N- dimethylamino) propyl)-2,7-fluorene)]) in PTB7:PC71BM (poly([4,8-bis[(2-ethylhexyl)oxy]benzo[1,2-b:4,5-b']-dithiophene-2,6-diyl][3-Fluoro-2-[(2-ethylhexyl)carbonyl]thieno-[3,4-b]thiophenediyl]): [6,6]-phenyl-C71-butyric acid methyl ester) blend to enhance the surface-charge collection in ITO/PFN/PTB7: PC71BM/MoO$_3$/Ag device structure, the PCE reached up to 8.7%.

In 2015, T. Goh *et al.* [13] used P3HT (Poly-(3 hexylthiophene-2,5-diyl)) as a ternary acceptor in PTB7:PC71BM blend and studied the effects of concentration of P3HT in ternary blend organic solar cells. They observed significant improvement in PCE from 7.08% to 8.63%. P3HT (2.1eV) is wider bandgap polymer than PTB7 (1.7eV). Excitons generated in P3HT are efficiently transferred to the PTB7 via Forster resonant energy transfer mechanism. The maximum absorption coefficient for P3HT is at approximately 500 nm and for PTB7 at 700 nm, so the overall absorption range is increased. Time-resolved photoluminescence (TRPL) spectroscopy shows an improvement in exciton lifetime with increasing concentration of P3HT in the active layer.

The ternary blend concept is extended to high-efficiency photodetectors. W. L. Xu *et al.* [14] fabricated the photodetector using P3HT: PC71BM and PTB7 used as a ternary element. UV-Vis absorption spectra of PTB7 and emission spectra of P3HT overlapping showed efficient Forster resonant energy transfer from P3HT to PTB7. The time delay measured by time-resolved photoluminescence spectroscopy showed reduction with increasing concentration of PTB7 and hence on/off ratio improved in ternary blend structures.

The dual donor blend based organic solar cell shows enhanced performance due to improvement in morphology and reduction in trap density. S. Chand *et al.* [15] compared the

performance of bulk heterojunction solar cells based on PTB7: PC71BM. They added poly [N-9''-hepta-decanyl-2,7-carbazole-alt-5,5-(4',7'-di-2-thienyl-2',1',3'benzothiadiazole)] (PCDTBT) as second donor material. They correlated mobility, trap density, morphology, and PCE and found that the increase in PCE was due to a reduction in trap density on adding dual donor material and the transition of charge carriers at the heterojunction from donor to acceptor level became favorable due to tuning of energy levels.

Hashimoto *et al*. [16] explored the effect of interfacial properties on the performance of an organic photovoltaic device. In their work, films of P3HT and PCBM were connected to each other by a film transfer method. The surface roughness is the main issue in this method so the film is transferred without disturbing their surfaces. Surface segregated monolayer (SSM) modified layers provide better interface quality and tuning of surface dipole moment. J-V characteristics of bilayer organic photovoltaic devices fabricated by the SSM method with interfacial dipole moments selected to align the energy levels at the heterojunction clarify that the device performance is highly dependent on the direction of dipole moment at the heterojunction. They also explored the effect of annealing on the performance of solar cells. Annealing of the active layers causes improvement in PCE due to better contact between P3HT and PCBM layers.

Electrode interfaces and donor-acceptor interface do not individually affect the performance of the device; instead, it is affected by the dynamic coupling between these interfaces as shown by magneto-photocurrent studies. The dynamic coupling behavior was studied by W. Ting *et al*. in 2015 [17]. In this work, two bulk heterojunction solar cells were fabricated with electrode interfaces of ZnO and PFN (an organic ferroelectric material) and compared. Magneto-photocurrent and capacitance-voltage (C-V) measurements have been performed on the devices. Photocurrent in both devices was changed with the magnetic field at different rates on the specifically biased conditions. Here, spin-dependent recombination was changed on applying the magnetic field due to changing the singlet-triplet excitons ratio. The bias required to eliminate the change in magneto-photocurrent was different for ZnO and PFN. C-V measurements proved that high dipole moment at interface requires high biasing to eliminate the change in magneto-photocurrent. Hence, the dipole moment at the interface affected the charge dissociation at the donor-acceptor interface.

Real-time exciton dissociation dynamics was studied by Ginger *et al*. [18] using time-resolved electrostatic force microscopy. In this method, the device heterojunction was excited

with pulsed laser and excitons were created in the active layer. These excitons were dissociated into free carriers and cause charging in the sample; hence, the charging rate was used to study the real-time exciton dissociation dynamics. It is useful for probing weak subgap excitations in nanostructured materials solar cells.

A radiative ternary material N,N′-Bis(3-methylphenyl)-N,N′-diphenylbenzidine (TPD) absorbs radiation in the range of 300 nm to 400 nm and radiates in the range of $400 - 450$ nm. This emitted radiation overlaps with the absorption spectra of P3HT; hence the addition of TPD enhances the overall absorption range which results in higher power conversion efficiency. Here, TPD works as a frequency converting element; it converts a high-frequency photon to a low-frequency photon. From the absorption and emission spectra of TPD and P3HT, it is clear that high energy photons are converted into low energy photons and these low energy photons are absorbed in P3HT donor material [19].

Thus, improvement in device architecture, fabrication techniques, and use of novel materials provide favorable conditions like efficient exciton transfer and dissociation into free carriers, reduction in recombination rates, enhancing the absorption spectral range.

2.3. Exciton Dissociation Process

Exciton dissociation process at the donor-acceptor interface is not yet clearly understood due to its complex nature. Excitons at the interface dissociate into free carriers via several charge transfer states as shown in Fig. 1.4. The nature of the charge transfer states is highly dependent on material, morphology and fabrication techniques, etc. [20].
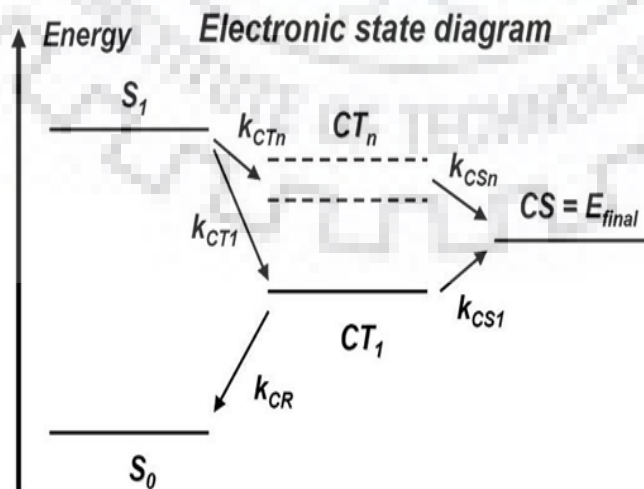
Figure 1.4 Charge transfer states at the donor-acceptor interface between bound exciton and charge-separated state.

8
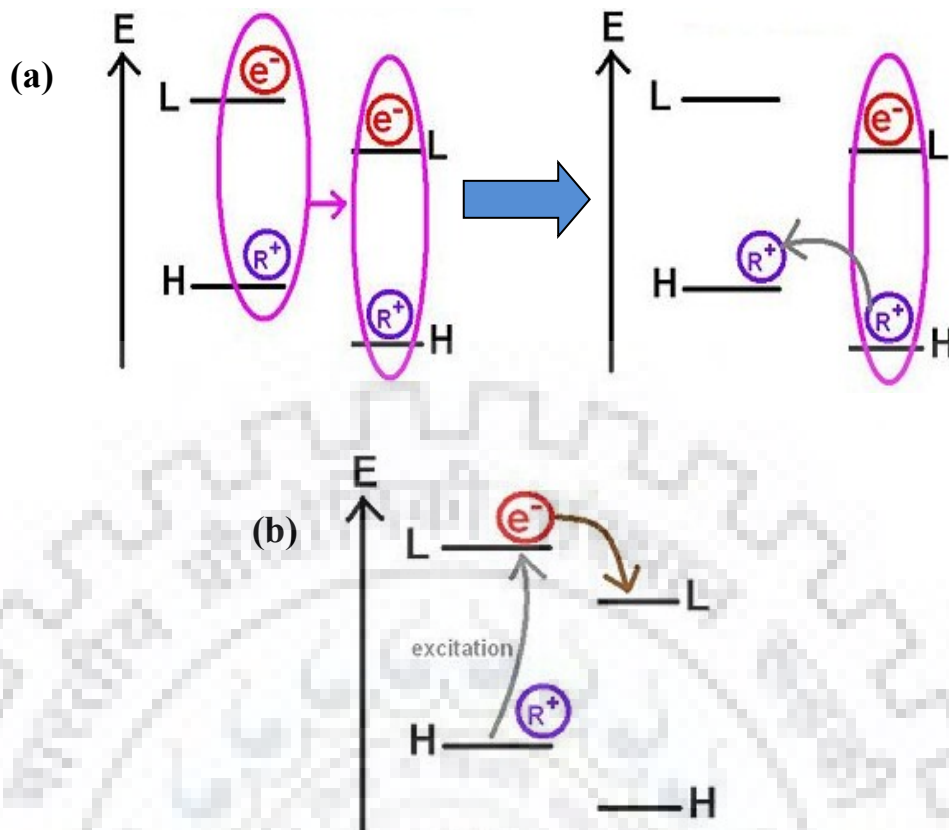
Figure1.5 Exciton dissociation processes (a) via exciton transfer and (b) direct dissociation by electron exchange at the donor-acceptor interface.

As shown in Fig.1.5, there are two mechanisms to explain exciton dissociation process. The first one is graphically shown by 'a'. In which, an exciton (or energy) is first transferred from donor to acceptor material then it dissociates into free carriers. The hole is transferred to the HOMO level of donor material from the HOMO level of acceptor layer and electron remains at the LUMO level of the acceptor. While in the second one (shown by 'b'), the electron is directly transferred to the LUMO level of acceptor material from the LUMO level of the donor layer.

The power conversion efficiency of an organic solar cell is mainly limited by the recombination of charge carriers via charge transfer exciton or charge transfer states. Hallermann *et al.* [21] correlated the recombination rate via charge transfer states with short circuit current in a solar cell. By PL measurements, it has been observed that at higher PL intensity, the short circuit current is lower. This should be obvious as higher PL intensity is due to the high recombination rate of excitons which leads to lower J_{SC}.

In addition, it is observed that the performance of a solar cell can be improved by adding the inorganic thin films of nanoparticles, ferroelectric materials, etc. at the various interfaces. It is also found that on inserting a thin insulator layer at the donor-acceptor interface, efficiency is improved. This is mainly due to the high dielectric constant of inorganic materials which reduces the exciton binding energy and it dissociates easily (low energy). But, tuning of energy barriers at the interface is also required for efficient device performance so nanoparticles can be used because the bandgap of a nanoparticle is dependent on their particle size [22-27].

There are many simulation tools that help in parameter optimization, cell architecture design, and many more other studies but numerical analysis of organic and inorganic material is quite complicated. For the numerical analysis of organic and inorganic semiconducting devices, the drift-diffusion model is widely used [28]. It provides satisfactory information at the lower computational cost. In inorganic semiconducting devices, mobility is much higher than the organic semiconductors so conventional relations are not blindly applicable to organic devices. Thus, simple diode models cannot be used.

Low mobility of charge carriers limits the operation of organic solar cells and characteristic parameters are changed, so power conversion efficiency cannot be predicted with available models for inorganic solar cells [29-41]. Further, due to the low dielectric constant of organic semiconductors, the photo-generation of free charges is not quite simple as in inorganic solar cells. Exciton dissociation and charge transfer process is a very complex process and not well understood yet [42-43]. There is a controversy about the exciton dissociation. Numbers of papers are available that show the donor-acceptor interface is very important to achieve efficient photovoltaic devices but how charge and energy transfer at interface takes place and which mechanism is dominant is not clearly understood. There are various intermediate processes involved between the photon absorption and generation of photocurrent. U. Wurfel *et al.* [44] concluded that a lot of precautions are necessary to carry a numerical analysis of organic solar cells. They showed that the effect of charge transport on the various parameters of the device and proven conventional relations were not valid for the organic solar cells. All invalidities were arising due to the low carrier mobility in organic semiconductors. Some extra inputs were needed to predict the performance of an organic solar cell that was ignored or approximated in conventional devices.

3. Quantum Dots

Theoretically, quantum dots are 0-dimensional point particles having discrete energy levels like an atom, but, in practice, these are the tiny particles of size few nanometers. The energy states of bulk materials form a continuous band structure, while the quantum dots/nanoparticles, the energy states start becoming quantized on confining the motion of electrons in all three directions. The density of states of bulk materials and various quantum structures are shown in Fig. 1.6. The continuous bands in bulk semiconductors are considered as overlapping of discrete energy levels of all atoms in a crystalline lattice. As the size of a QD is decreased, the energy bands are no longer continuous. The energy gap between the energy levels is increased and causes energy states like an atom [45-48].
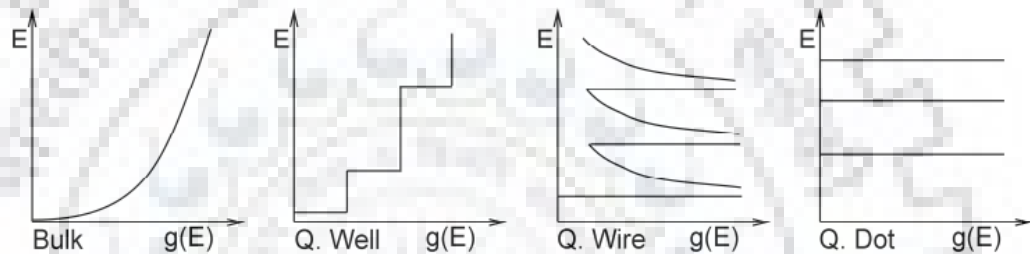
Figure 1.6 The density of states of bulk semiconductor, quantum well, quantum wire and quantum dot.

The quantum effects are observed when particle size is of the order of Bohr radius. Bohr radius can be defined from Bohr's model of a hydrogen atom. Bohr's radius is the size of a bound electron-hole pair for most semiconductors. The exciton Bohr radius is the critical size at which material properties are defined by quantum confinement instead of bulk properties. Thus, tiny particles of semiconductors with size (typically few nanometers) comparable to the Bohr radius show the quantum properties. So, bandgap of the quantum dots can be easily tuned with the size of QD due to increasing energy level splitting with decreasing size. This result can be predicted using a quantum mechanical solution of "particle in a box" theory. The bandgap of quantum dots is always greater than that of bulk material and it increases as we reduce the particle size.

3.1. Synthesis of Nanoparticles

The process of nanoparticle synthesis can be divided into three phases: (a) nucleation phase (b) growth period, and (c) termination of the reaction. The nucleation phase is the duration in which reactant concentration is higher than the nucleation threshold. In this duration, quantum dots nucleate and reactant concentration in the reaction chamber drops

below the threshold concentration. After that, the nucleated QDs start to grow. Upon reaching the desired size, the reaction is forced to stop [49-50].

There are numbers of ways to synthesize the quantum dots which are categorized into two parts:

- Vapor phase synthesis

In this process, the vapor of required materials is allowed to condense in a controlled manner to achieve the desired sized QDs. Ways of forming vapors of materials are further categorized in several synthesis processes on the basis of energy sources such as using pulsed laser, spark discharge, ion sputtering, thermal/non-thermal plasma, etc. These processes generally used in the synthesis of elemental (Si, Ge, and other metallic) quantum dots [51-53].

- Liquid phase synthesis

Liquid phase synthesis is a commonly used technique for the preparation of quantum dots. The precursor solution of the required materials is allowed to react in a reaction chamber. The precursors are put together (non-injection technique) or injected sequentially (injection technique) in the chamber. The concentration and timing are the common controlling parameters to achieve the desired size of quantum dots.

The injection technique provides mono-dispersed nanoparticles with high quantum efficiency. For many applications, mono-dispersity of quantum dots is desired to achieve a sharp luminescence peak. Thus, in the emission spectra of quantum dots, mono-dispersity controls full-width half maxima, quantum yield responsible for intensity, and wavelength defined by the bandgap (size) of quantum dots [54-56].

3.2. Role of Quantum Dots in Solar cells

Different sizes of quantum dots have the corresponding absorption in different regions of the solar spectrum. Thus, generally, quantum dots in a solar cell are integrated to enhance the absorption spectra of the cell. Applications of quantum dots in solar cells are not limited to enhancement in absorption in the cell [57-59]. Narrow-band-gap QDs, such as CdS, CdSe, PbS, etc. have unique advantages in solar cell applications. Quantum dots have large extinction coefficients due to the quantum confinement effect and large intrinsic dipole moments which lead to efficient charge separation. Quantum dots also exhibit the unique capability of multiple exciton generation (MEG). In MEG, a single photon is able to produce multiple excitons

depending on the energy of photon and bandgap of QDs. Thus, the internal quantum efficiency is greater than unity. Efficient charge transfer from QDs to the conduction band of acceptor material is required and depends on the energy band alignment at the interface. The band alignment can be achieved by tuning the lowest unoccupied molecular orbital and highest occupied molecular orbital energy levels in the QDs by controlling their size. QDs reduce the thermalization losses; promote multi exciton generation on the cost of single photon. It can create an intermediate band and enhance the absorption of low energy photons. Thus, the QDs are beginning to be widely used in solar cells as an efficient alternative for dye in dye-sensitized solar cells (DSSCs). These cells are called QD sensitized solar cells (QDSSC) [60-64].

QDs can alter the dynamics of carrier recombination, mobility, injection rates, etc. in the device which can lead to enhanced device performance [65-73]. Furthermore, QDs are also used as a stability improving agent in organic solar cells. Chuang *et al.* fabricated ZnO/PbS quantum dot solar cell at room temperature by all solution processing which overcame the major challenges of low efficiency, high-temperature fabrication and poor ambient stability by choosing proper ligand which provided better band alignment of the quantum dots in the device. The reported device efficiency was 8.55% and the J-V characteristics were almost unchanged over 150 days of non-encapsulated devices stored in the air [74]. Thus, QDs can be used as a promising candidate for the tuning of the performance of the solar cells. The recombination rate in QDs, injection/extraction rate at the QD interfaces, and tunneling among the QDs are the essential parameters that can be modified according to the requirements of the device. The recombination rate can be controlled by changing the doping of nanoparticles. Injection/extraction rates are highly dependent on the interface quality (surface roughness, energetic disorder etc.). The transport among the QDs is controlled by choosing an appropriate capping agent.

S. Gustavsson *et al.* [75] and D. Weinmann *et al.* [76] have done an exhaustive study on microscopic single-electron transport through the QDs at low temperatures. The field dependence on charge transport in nanoparticles (nanowire, nanotubes, etc.) is studied by Verma *et al.* [77-79]. Very few mathematical models have been developed to deal with the charge transport in QDs at room temperature for device applications.

4. Motivation

Solar energy is the most promising renewable energy among the other sources due to its abundant availability on the earth surface. It is many thousands of times of the world's current demand for energy. On the other hand, fossil fuel-based energy conversion depends on the limited resources which may lose in few years. Burning fossil fuels produces carbon dioxide which acts as a greenhouse gas and results in climate change (Global warming).

Organic solar cells have advantages over the inorganic solar cells such as low cost by high throughput roll-to-roll printing, low-temperature deposition techniques, non-toxic material, mechanically flexible and lightweight devices, and low consumption of active materials. But, there are few challenges such as stability in an ambient, short lifetime, and low power conversion efficiency; so, quality research is needed to be carried out. The generation of free carriers is an excitonic process. It is quite different from free carrier generation in inorganic semiconductors. Dissociation of exciton at the donor-acceptor interface is a very complex process and it is still not clear what exactly happens. The lack of clarity about charge and energy transfer processes at the donor-acceptor interface (the key process) in organic solar cells and the effects of inserting the inorganic/organic intermediate layers at donor-acceptor interfaces on charge transfer processes motivate research in this direction.

5. Structure of the Dissertation

- Chapter 2 introduces the analysis of bilayer heterojunction diodes in which different regimes of current-voltage characteristics based on the energy band diagram of the device and various physical parameters are studied that affect the device characteristics.

- Chapter 3 deals with the modeling of quantum dots solar cells and analysis of effects of charge transport and carrier recombination in the quantum dots on the solar cell characteristics.

- Chapter 4 details the fabrication techniques of various quantum dots and related solar cells.

- Chapter 5 contains an analysis of s-shaped current-voltage characteristics obtained from the fabricated quantum dot solar cells (chapter 4) with the help of the proposed model (chapter 3).

- Chapter 6- conclusion and scope for future work.

Chapter 2

Current-Voltage Characteristics of Bilayer Heterojunction Diodes

1. Introduction

Organic light-emitting diodes (OLEDs) and organic photovoltaic cells (OPVs) are widely accepted organic semiconductor devices. Modern organic semiconductor devices give efficient performance due to enhancement in key mechanisms for a particular application by introducing the multilayered structure of the device [80-83]. In previous papers, numerous charge transport models are proposed in the operating range of a single layer device by the incorporation of various charge transport processes such as Child's law, trap-charge limited, recombination, and injection based conduction, etc. [84-88]. In addition, the device structure of the OLEDs and OPVs is almost the same but the mode of operations is different. Generally, OLEDs are operated above the build-in-potential (V_{bi}) and OPVs having open circuit voltage approximately near the build-in-potential and operate below V_{bi} [89]. Thus, the models are not directly applicable to the multilayered devices due to additional effects of charge blocking/accumulation at the heterojunction interfaces. Hence, analysis of a model is needed which predicts the electric characteristics of OLEDs/OPVs.

Low carrier mobility, formation of the metal/organic interface, injection processes, charge transport, effects of doping, recombination near organic/organic interfaces and undoped amorphous semiconductor with very low intrinsic carrier concentration create complications in the modeling of an organic device as compared to inorganic p-n junction diodes [90-91]. Inorganic p-n junction physics can be applied in the modeling of heterojunction organic diodes by considering the effects of metal-organic interface barrier, organic-organic interface barrier, equilibrium carrier distribution, etc. Thus, a model based on energy band theory has features to predict the current-voltage characteristic of the heterojunction organic diodes. In the analysis, the material parameters like carrier mobility, carrier lifetimes, dielectric constant, etc. are assumed to be constant.
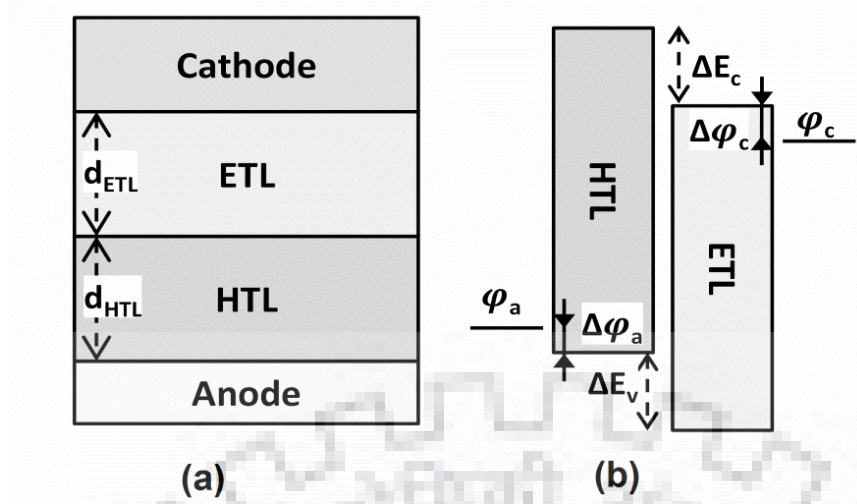
Figure 2.1 (a) Device schematic of a bilayer heterojunction diode and (b) corresponding energy band alignment of individual layers.

In this chapter, a p-n junction diode like model is developed to predict the current-voltage characteristics in a heterojunction organic diode on the basis of energy band theory and material specifications. The developed model is analyzed in order to understand the charge transport phenomenon and affecting parameters like metal-organic, organic-organic interfaces, mobility, layer thickness, etc. and is compared with the analytical solution of governing transport equations in a heterojunction organic diode by considering the drift-diffusion approximation with Boltzmann statistic of carrier injection in amorphous materials and validated with experimental current-voltage data of an OLED and OPV.

2. Charge Transport Model

2.1. Transport equations

The drift-diffusion approximation is used to describe the charge transport in each transport layer. It is described by a set of continuity equations for holes and electrons and Poisson's equation as follows:

$$\frac{\partial p}{\partial t} = -\frac{1}{q} \cdot \frac{\partial J_p}{\partial x} - R + G \tag{1a}$$

$$\frac{\partial n}{\partial t} = \frac{1}{q} \cdot \frac{\partial J_n}{\partial x} - R + G \tag{1b}$$

$$\frac{\partial^2 \psi}{\partial^2 x} = -\frac{q}{\varepsilon}(N_d - N_a + p - n) \tag{1c}$$

where,

$$J_p = -qD_p \frac{\partial p}{\partial x} - qp\mu_p \frac{\partial \psi}{\partial x} \tag{1d}$$

$$J_n = qD_n \frac{\partial n}{\partial x} - qn\mu_n \frac{\partial \psi}{\partial x} \tag{1e}$$

The generation rate is assumed to be zero under dark. Recombination in the transport layers is modeled by Shockley-Read-Hall recombination. Assuming trap centers are at intrinsic energy level, the recombination rate is given by,

$$R = \frac{pn - n_i^2}{\tau_p(n+n_i) + \tau_n(p+n_i)} \tag{2}$$

2.2. Boundary conditions

Device schematic of the bilayer organic diode is shown in Fig. 2.1 (a). The active material is sandwiched between two electrodes of different work functions. Generally, a hetero-junction of hole transport layer (HTL) and electron transport layer (ETL) is considered as an active layer and a transparent indium tin oxide (ITO) is used as an anode while aluminum (Al) as a cathode. The HTL and ETL have thickness d_{HTL} and d_{ETL} and the energy offset between their highest occupied molecular orbital (HOMO) and lowest unoccupied molecular orbital (LUMO) levels are ΔE_v and ΔE_c respectively. The energy barriers at metal-organic interfaces, $\Delta\varphi_a$ (at the anode) and $\Delta\varphi_c$ (at the cathode), are the difference between anode/cathode work functions (φ_a and φ_c) and HOMO/LUMO levels of HTL and ETL respectively [92].

The organic semiconductors are generally undoped and carrier concentrations at the electrode-organic interfaces can be obtained by Gaussian distribution of carriers. So, the following relations have been considered as the boundary conditions for our calculations

At the anode:

$$p(0) = N_v exp\left(-\frac{\Delta\varphi_a}{kT}\right) \tag{3a}$$

$$n(0) = N_c exp\left(-\frac{E_{g\_htl} - \Delta\varphi_a}{kT}\right) \tag{3a}$$

$$\psi(0) = V_a \tag{3c}$$

And at the cathode:

$$p(L) = N_v exp\left(-\frac{E_{g_{etl}} - \Delta\varphi_c}{kT}\right) \tag{3d}$$

$$n(L) = N_c exp\left(-\frac{\Delta\varphi_c}{kT}\right) \quad\quad (3e)$$

$$\psi(L) = \frac{\varphi_a - \varphi_c}{q} \quad\quad (3f)$$

where V_a is the applied bias, kT/q is the thermal potential.

A simulated current-voltage characteristic is obtained by simultaneous solution of transport equations under the above boundary conditions.

3. Current-Voltage Characteristic Model

3.1. Equilibrium carrier concentration

The energy band diagram is shown in Fig. 2.1 (b) and the built-in-potential (V_{bi}) is the work function difference of the anode and cathode [87, 93].

$$V_{bi} = \frac{\varphi_a - \varphi_c}{q} \quad\quad (4)$$

Organic semiconductors are generally undoped and have a negligible number of intrinsic charge carriers, thus a constant electric field ($E = V_{bi}/d$) is present inside the device. The charge concentration at the metal/semiconductor interface is found according to the Gaussian statistics. Hence, carrier distribution in the device can be obtained by solving the continuity equation [94-95]

$$D_p \frac{\partial^2 p}{\partial x^2} - \mu_p E \frac{\partial p}{\partial x} - \frac{p}{\tau_p} = \frac{\partial p}{\partial t} \quad\quad (5)$$

where, p is the hole concentration in the device and D_p, μ_p, and τ_p are the diffusion coefficient, mobility and lifetime for hole respectively.

The continuity equation for holes (Eq. 5) can be solved in steady-state with the following boundary conditions

$$p(0) = N_v exp\left(-\frac{\Delta\varphi_a}{kT}\right) \quad\quad (6a)$$

$$p(\infty) = 0 \quad\quad (6b)$$

where, N_v is the density of states in the valence band (HOMO level) of HTL and kT is the thermal energy in eV. Here, zero (0) stands for metal/organic interface at the anode. Thus, the hole concentration is

$$p(x) = N_v exp\left(-\frac{\Delta\varphi_a}{kT}\right) exp\left\{-\frac{1}{2}\left(\frac{\mu_p E}{D_p} + \sqrt{\left(\frac{\mu_p E}{D_p}\right)^2 + \left(\frac{2}{\sqrt{D_p \tau_p}}\right)^2}\right)\right\} x \tag{7}$$

Now, putting $\frac{\mu_p}{D_p} = \frac{q}{kT}$ and the diffusion length $L_p = \sqrt{D_p \tau_p}$, (7) is further simplified as

$$p(x) = N_v \exp\left(-\frac{\Delta\varphi_a}{kT}\right) \exp\left\{-\frac{1}{2}\frac{qE}{kT}\left(1 + \sqrt{1 + \left(\frac{\frac{2}{L_p}}{\frac{qE}{kT}}\right)^2}\right)\right\} x \tag{8}$$

The term $\left(\frac{2}{L_p}/\frac{qE}{kT}\right)^2 \ll 1$, so on taking approximation, the equation is rewritten as

$$p(x) = N_v \exp\left(-\frac{\Delta\varphi_a}{kT}\right) \exp\left(-\frac{qE}{kT}x\right). \tag{9}$$

Thus, hole distribution in HTL is

$$p(x) = N_v \exp\left(-\frac{\Delta\varphi_a}{kT}\right) \exp\left(-\frac{qE}{kT}x\right) \tag{10a}$$

and in ETL is

$$p(x) = N_v \exp\left(-\frac{\Delta\varphi_a + \Delta E_v}{kT}\right) \exp\left(-\frac{qE}{kT}x\right). \tag{10b}$$

The electron distribution can be found in a similar way.

3.2. Reverse and below flat band applied bias (Regime I)

As the organic semiconductors are undoped, whole active layer is depleted and injected carriers decay exponentially. On applying a reverse bias voltage, it shifts the majority carrier concentration towards the electrode and current in the device is limited by carrier generation-

recombination process in the effective depletion region. The generation current can be obtained by integrating the recombination rate over the depletion width (*W*) and written as [95]

$$J_{gen} = -\frac{qn_iW}{2\tau_0} .$$

(11)

In the organic semiconductor diodes, many factors such as low carrier mobility, trap state distribution, organic/organic interface barrier, etc. affect charge transport in a non-linear fashion so recombination current equation is

$$J_{rec} = J_{r0}\left[\exp\left(\frac{qV_a}{\eta_r kT}\right) - 1\right]$$

(12)

where, recombination saturation current density $J_{r0} \approx J_{gen}$ and ideality factor $\eta_r \approx 2$ are the fitting parameters.

3.3. Flat band to the threshold voltage (Regime II)

At the applied bias equal to the built-in-potential, the flat band condition is reached and the electric field in the device is reduced to zero thus, carrier concentrations are constant throughout HTL and ETL separately and are obtained by (Eq. 10) on taking *E=0*. It is seen that majority carrier accumulate at the organic-organic interface with further applied forward bias and the minority carrier diffusion from the interface to electrode becomes similar to the carrier diffusion in the neutral region of a p-n junction diode. The steady-state continuity equation (Eq. 5) for holes in ETL is

$$D_p\frac{\partial^2 p}{\partial x^2} - \frac{p}{\tau_p} = 0 .$$

(13)

In the same way, as for the p-n junction diode, the diffusion equation (Eq. 13) can be solved for the boundary condition $p(0) = N_v exp\left(-\frac{\Delta\varphi_a + \Delta E_v - q(V_a - V_{bi})/\eta}{kT}\right)$, we get the current

$$J_{diff} = J_s\left[\exp\left(\frac{q(V_a - V_{bi})}{\eta kT}\right) - 1\right].$$

(14)

22

Where, for a long base p-n junction diode, the saturation current density is given by the relation [94]

$$J_s = qn_i^2 \left[\frac{D_p}{N_d L_p} + \frac{D_n}{N_a L_n} \right], \tag{15}$$

and D, L are the diffusion coefficient and diffusion length and N_d, N_a are the donor and acceptor doping concentrations respectively.

In relation, the term $\frac{n_i^2}{N_d}$ and $\frac{n_i^2}{N_a}$ are the equilibrium hole and electron concentration in *n-type* and *p-type* regions respectively thus, it can be replaced by the hole and electron concentration in the ETL and HTL under flat band condition. Hence, (Eq. 15) can be modified as

$$J_s = q \left[N_v \exp\left(-\frac{\Delta\varphi_a + \Delta E_v}{kT} \right) \frac{D_p}{L_p} + N_c \exp\left(-\frac{\Delta\varphi_c + \Delta E_c}{kT} \right) \frac{D_n}{L_n} \right]. \tag{16}$$

3.4. Bulk resistance limited region (Regime III)

The current in the high injection regime is limited by the bulk resistances of the active layers. The band offset at interface blocks the movement of charge carrier resulting in charge accumulation at the interface thus external voltage needs to exceed some critical value which is proportional to the sum of V_{bi} and band edge offset at the interface. The critical voltage is considered at which the J-V curve enters in regime III and is named as threshold voltage. The electric field across the active layer is $E = (V_a - V_{th})/d$. Charge transport in this regime is drift dominant with field-dependent carrier mobility. Poole-Frenkel model of field-dependent mobility is given as [96]

$$\mu = \mu_0 exp\left(\gamma\sqrt{E} \right) \tag{17}$$

where, μ_0 is the zero-field carrier mobility and γ is a constant. Thus, the drift current can be written as [92, 97]

$$J_{drift} = G(V_a - V_{th}) \exp\left(\frac{\sqrt{V_a - V_{th}}}{\sqrt{V_{pf}}} \right) \tag{18}$$

23

where, conductance (G) and voltage term (V_{pf}) are the fitting parameters and depend on zero-field mobility, injected carrier concentration and distribution of HOMO/LUMO levels respectively.
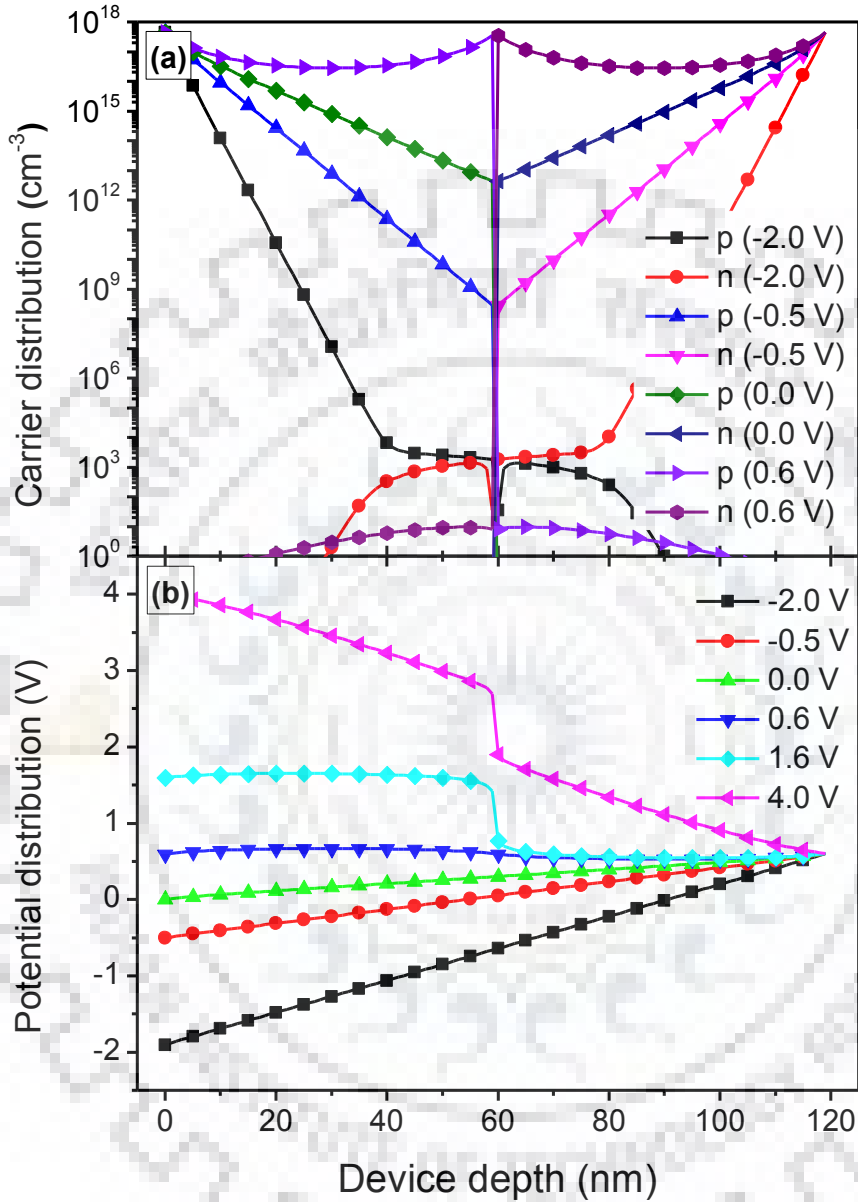
Figure 2.2 (a) Charge carrier and (b) potential distribution in the device at various applied biases.

Thus, the forward J-V characteristic of a bilayer organic diode is separated in three regimes of operation (i) recombination dominant current ($V_a < V_{bi}$) (ii) diffusion dominant current ($V_{bi} < V_a < V_{th}$) and (iii) bulk resistance limited current ($V_a > V_{th}$).

4. Model Validation and Analysis with Simulation Results

In order to obtain simulated current-voltage characteristics of a bilayer organic semiconductor diode, a computer code with quad-precision (128 bits) is written to solve the

24

basic semiconductor equations (continuity equations for electron and hole and Poisson equation). The drift-diffusion approximation with Shockley-Read-Hall and bimolecular recombination process has been used in the numerical analysis of the diode. The exciton diffusion equation can be solved independently with the equilibrium carrier distributions so the integration of exciton continuity equation in the simulation has been ignored. The Gaussian statistics and electrode work function are used as boundary conditions to obtain carrier concentration and potential at the metal/organic interfaces [98-99].

For the numerical analysis of the schematic device, the HTL and ETL thicknesses are assumed to be equal and total device thickness is 120 nm. Band gaps of each (HTL and ETL) material are $E_{g1}=E_{g2}=2.0$ eV and $\Delta E_v=\Delta E_c=1.0$ eV are discontinuities present in their band edges. At the metal/organic interfaces, the energy barriers are also assumed to be the same and equal to 0.2 eV. Thus, from the energy diagram, V_{bi} and V_{th} are equal to 0.6 V and 1.6 V respectively.

Before comparing the simulated J-V characteristic with the model, charge and potential distribution in the device must be analyzed to understand the variation in transport processes in various regimes. Thus, variations in carrier concentration and potential distribution at various applied biases are shown in Fig. 2.2. At 2.0 V reverse bias, the majority carrier concentration shifts towards the electrodes in respective transport layers consequently, effective depletion width changes to ~40 nm where electron and hole concentration is almost equal and the reverse saturation currents obtained by numerical analysis (4.51×10^{-15} A/cm^2) and Eq. 12 are approximately same. Reduction in reverse bias results in increase in majority carrier concentration while the minority carrier concentration is reducing due to increase in recombination rate and reduction in electric field in the device. In equilibrium, minority carrier concentration reaches its minimum value; the carrier distribution is constant throughout the transport layer as applied bias reaches near the built-in-potential. At $V_a=V_{bi}$, the electric field in the device is reduced to zero and transport layers are just like a neutral region in p-n junction diode and the current in the device is dominated by the diffusion process. Further increase in forward bias causes an increase in charge accumulation at the interface barrier and the additional applied voltage drops across the junction only. At the threshold voltage, the voltage drop across the junction becomes equal to the barrier at the interface and the electric field in the transport layers still remains to zero. Additional forward bias drops across the transport layers while the junction voltage remains the same. Thus, beyond threshold voltage, the current in the device is limited by the bulk resistance of the device.
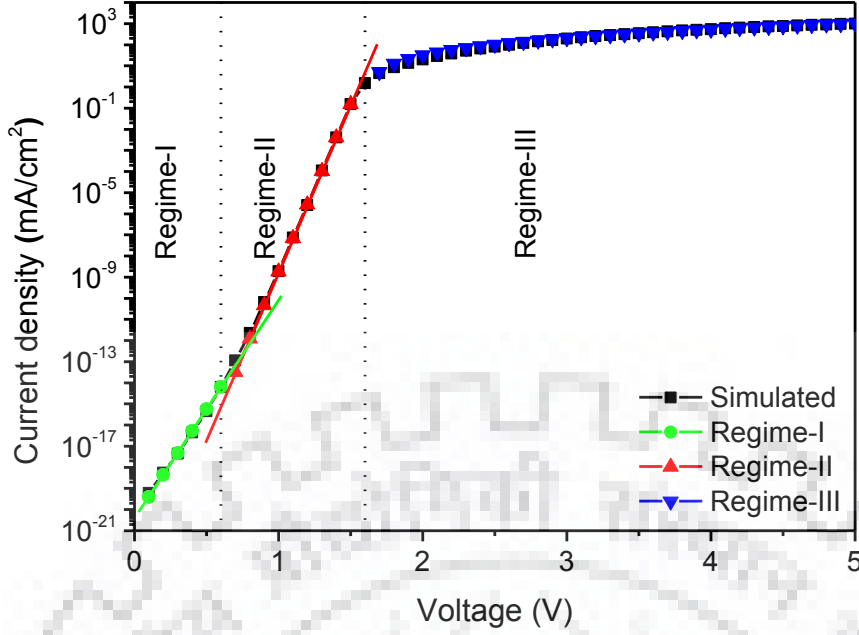
Figure 2.3 Simulated current-voltage characteristics fitted with the current in different regimes.

TABLE-2.1 Fitting parameters and corresponding reduced Chi-square and adj. R-square values in the different regimes (Where J_{r0}, J_s are in mA/cm^2 and G is in S/cm^2)

Model	Parameter Value (Standard error)	Reduced Chi-Square	Adj. R-Square
Regime-I	J_{r0}=6.31×10^{-24} (1.39×10^{-24}) η=1.72 (0.035)	4.53×10^{-42}	0.9998
Regime-II	J_s=2.56×10^{-28} (2.51×10^{-30}) η=1.053 (0.0002)	5.29×10^{-18}	0.9999
Regime-III	G=.0415 (0.00223) V_{th}=1.61 V_{pf}=0.857 (0.051)	2.31×10^{-4}	0.9977

Fitting of simulated J-V characteristic with the proposed current-voltage model in different voltage regimes has been performed. Fitted curves in separate regimes are plotted in Fig. 2.3 over the simulated J-V characteristic. In regime-I, the simulated J-V characteristic is well fitted with the model for J_{r0} in the order of 10^{-24} mA/cm^2 and the ideality factor η =1.72 which shows that current in the device is dominated by recombination process while in regime-II, ideality factor changed to η =1.05 thus, the current is dominant by diffusion process. The third regime is bulk resistance limited regime in which the current is mainly limited by conductance and field-dependent mobility in transport layers. According to the model, the simulated J-V characteristic well fitted for G =4.15×10^{-2} S/cm^2, V_{pf} =0.86 and V_{th} =1.61 V.

Thus, overall diode characteristic obtained by numerical analysis have been traced with the models in the specific regimes. The fitting parameters in different regimes and corresponding fitting goodness parameters (reduced Chi-Square and adjusted R-Square) are tabulated in Table-2.1 which provide good agreement of acceptance of the models.

4.1. Effects of band parameters on J-V characteristic

The interface barrier at the band edges plays an important role in charge transport in the device. It creates an energy barrier in the path of respective charge carriers consequently, the reverse saturation current (J_{r0}) is reduced. The energy barrier is also responsible for the charge accumulation at the interface so the applied bias beyond V_{bi} drops across the interface and the transport layers behave as neutral region thus, current in the device is due to diffusion of carriers. This shows that the interface barriers affect the J-V characteristics in the low voltage region by limiting the minority carrier injection at the interface. The J-V curves with varying band edge discontinuities (keeping $\Delta E_v = \Delta E_c$) are plotted in Fig. 2.4 (a) for equal HTL and ETL thicknesses. From the figure, it is clearly seen that the slopes of the curves are changing as the band edge discontinuity increases after a certain voltage. This voltage is found to be approximately same as the built-in-voltage of the device. For $V_a < V_{bi}$, the ideality factor is ~2; current in the device is recombination dominant. At $V_a = V_{bi}$, the flat band condition is reached and concentration of accumulated carriers at the interface barrier increases exponentially with V_a which increases the minority carrier injection in the corresponding transport layers and the diffusion process is dominated over the recombination of carriers. The bulk resistance limitation in the current starts at a fixed V_a which is approximately equal to the sum of built-in-potential and band edge discontinuity at the junction.

The device is again simulated for different values of metal/organic interface barrier; here wider bandgap for HTL and ETL is chosen to observe the effect on J-V curves of a large variation in $\Delta\varphi_a/\Delta\varphi_c$. It is shown in Fig. 2.4 (b) that as the $\Delta\varphi_a/\Delta\varphi_c$ increases, the J-V curves are saturated at lower voltages and lower current densities because metal/organic interface barrier affects the concentration of space charge injected from metal to semiconductor. It decays exponentially with increasing energy barrier and causes high bulk resistance of the transport layers but the carrier distribution profile in the device does not change. Thus, it significantly affects the J-V curve in bulk resistance limited region (regime-III) and current is limited by high resistive transport layer while the band edges discontinuities mainly affect the J-V characteristic in regime-I and II by blocking the carriers at the organic/organic interface barriers.
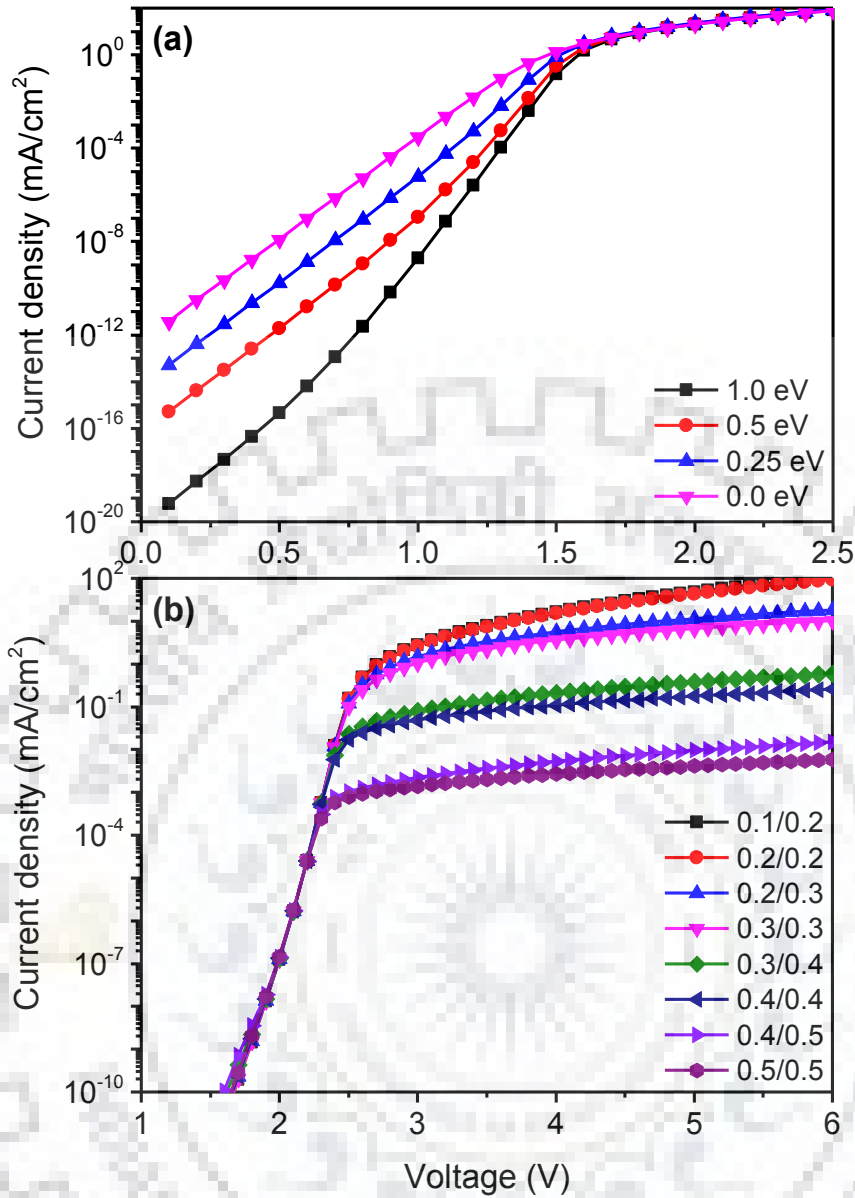
Fig. 2.4 (a) Effects of band-edge discontinuities at the heterojunction and (b) energy barriers at the metal-organic interface (anode/cathode) on the J-V characteristics.

4.2. Effect of position of heterojunction

In a bilayer device, the depth of the hetero-junction is an important fabrication parameter which controls the device performance primarily by controlling the bulk resistance of the device. The simulated J-V curves with varying junction depth are plotted in Fig. 2.5 and other parameters are kept same in order to obtain same conductivity of HTL and ETL. For the same carrier mobility, intrinsic concentration, and metal/organic interface barrier, the J-V curves are overlapping each other in the whole voltage range except for the lower applied bias. The behavior of the J-V curve in a low applied bias regime can be attributed to the change in carrier distribution inside the device on varying the thickness ratio of the HTL to ETL. As

carrier concentration exponentially decays with device depth, the junction near to either electrode leads to an increase in carrier concentration at the interface thus, diffusion of electrons/holes is dominating. Further increase in applied forward bias, the recombination rate at the heterojunction increases more rapidly than the centered heterojunction, thus near built-in-potential, the recombination current dominates and a kink in the J-V curve is observed. Hence, the position of hetero-junction is more important for an OPV performance but no significant effects are visualized in the working regime of an OLED.
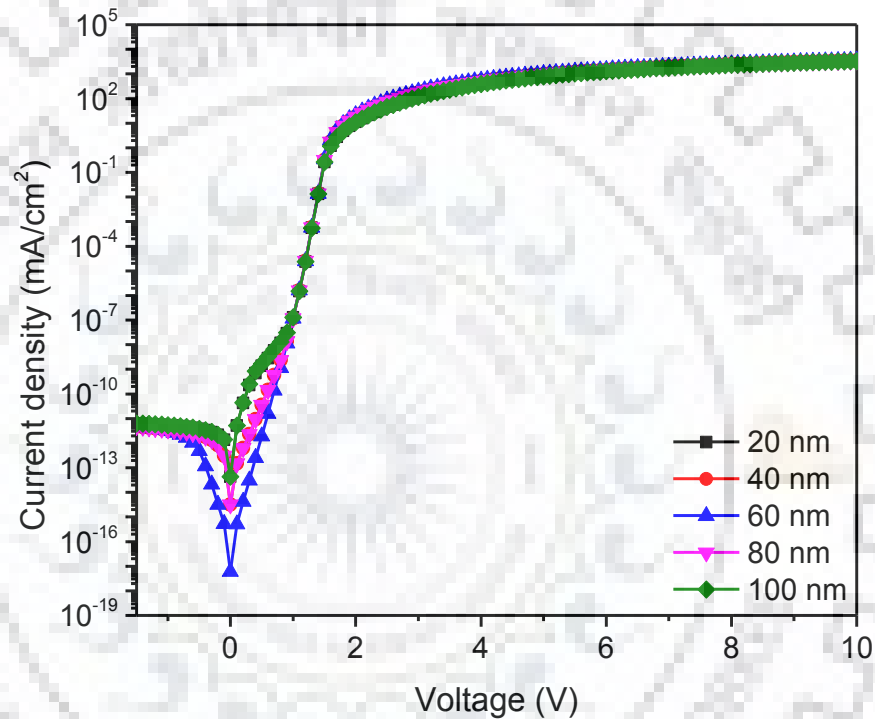
Figure 2.5 Effects of heterojunction depth on the J-V characteristics.

5. Model Validation with Experimental Data

In the context of model validation with experimental J-V curve of the bilayer organic diodes, a PV cell and an OLED have been fabricated using P3HT/PCBM and PVK/AlQ3 as the starting materials respectively according to methods given in Ref. [100-101]. Both the devices are fabricated on ITO (anode) coated glass substrate and thermally evaporated Al contacts are used as a cathode thus, built-in-potential (~0.7 volts) is same for both and band edge discontinuities and trap state density controls the threshold voltage in the devices.
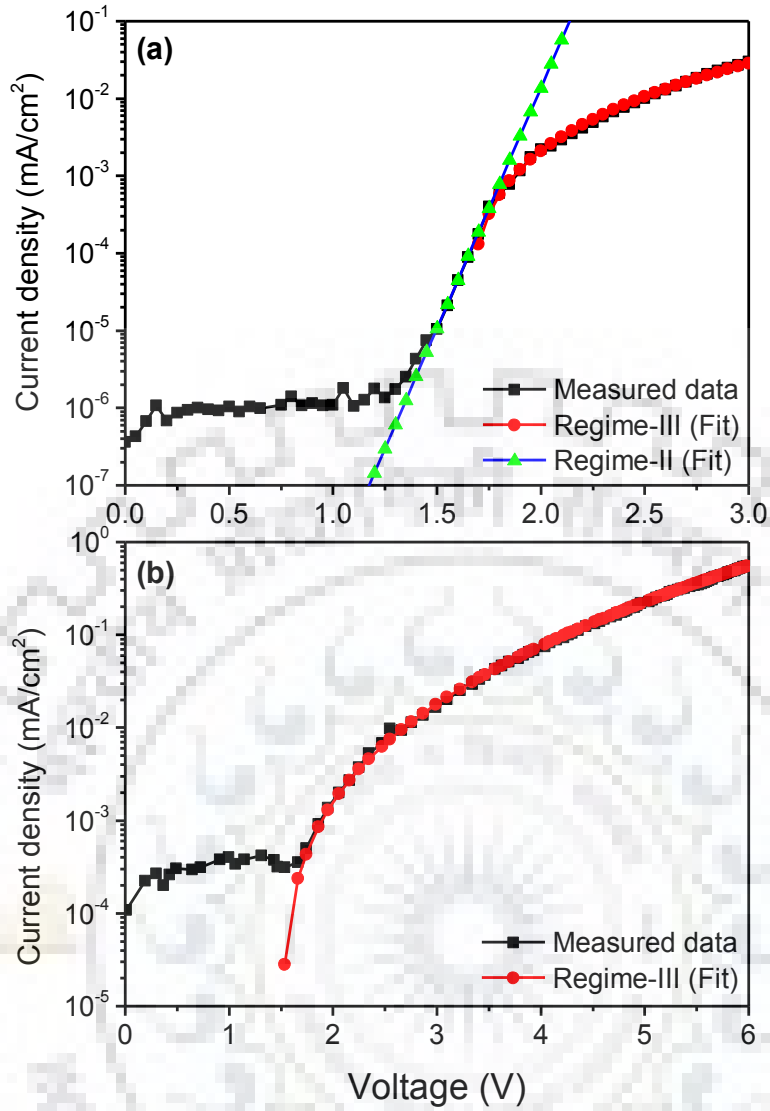
Figure 2.6 Fitting of experimental J-V characteristics of (a) P3HT/PCBM (PV Cell) and (b) PVK/AlQ3 (OLED) bilayer organic diode with the current in various regimes.

The J-V characteristics shown in Fig. 2.6 of the fabricated devices have been measured using a probe station and HP parameter analyzer. The ohmic current in low applied bias is due to shunt paths in the thin-film and limitation of measuring instrument is superimposed on the current in regime I and II; the current only in regime III is clearly visible. In Fig. 2.6 (a), some part of J-V characteristic in regime II is free from the effect of ohmic current which is fitted with the model and gives good agreement with the measured data having ideality factor of η ≈ 2.6 and saturation current density of $J_s = 5 \times 10^{-15}$ mA/cm^2. The band discontinuities are of ΔE_v $\approx \Delta E_c \approx 1.0$ eV at the P3HT-PCBM interface thus, fitted V_{th} (1.65 V) is approximately same as calculated (1.7 V). The model in regime III also covers whole measured data with $G = 1.6 \times 10^{-3}$ mS/cm^2 and $V_{pf} = 0.45$ V. Similarly, for regime III, the model excellently fits the experimental data of the OLED with $G = 5.0 \times 10^{-4}$ mS/cm^2, $V_{th} = 1.5$ V and $V_{pf} = 0.38$ V.

30

In the chapter, a piece-wise current-voltage model has been developed for bilayer organic diodes on the basis of the energy band diagram. The current-voltage characteristic is separated into three regimes of operation that are individually governed by recombination, diffusion and bulk resistance limited charge transport processes. The models in separate regions are compared with the results from the numerical solution of semiconductor equations with excellent agreements in respective regimes. It is observed that the band parameters: band edge discontinuity and metal interface barriers affect J-V characteristic below and above the threshold voltage by blocking charge transport and reducing carrier injection in transport layers respectively; it is negligibly affected by any variation in the position of heterojunction. The proposed models are also compared with experimental J-V characteristics of an OLED and photovoltaic diode. Thus, the model is able to predict the current and affected regimes of J-V characteristics of a diode on the basis of the energy band diagram and material parameters. Applicability of the model can be improved by interfacing it to the trap state model in the organic materials to analyze the effects of concentration of trap states, their spatial and energy distribution, etc. on the current-voltage characteristic.

Chapter 3

Modeling Quantum Dot Solar Cells

1. Introduction

In the recent years, organic photovoltaic devices (OPV) have attracted researcher's attention due to their low cost, ease of fabrication, flexible devices, and eco-friendly manufacturing [4-7]. Usually, OPVs have low power conversion efficiency. To improve the performance of these devices, researchers have used various methods such as the addition of metal nanoparticles, semiconducting quantum dots, and various nano-structured elements in the active layer. The nano-structured elements are primarily used to improve the absorption of photons or/and electrical parameters of active layer in the photovoltaic device [57-59].

Due to tunable bandgap and carrier confinement [102, 103], nanostructures such as quantum dots are extensively used in the light-emitting devices to achieve wavelength-tunable luminescence and efficient light sources. The QDs simplify the process of device fabrication because the only structural feature that tunes the properties of the device is the size of the QDs. The fabrication process to achieve various sizes remains essentially the same, other than varying a few parameters such as growth time and temperature [104-105].

In addition, the charge transport and recombination in OPVs play a crucial role in the device performance. In OPVs, high efficiency can be achieved if charge transport efficiently extracts the charge carriers from the active region and the recombination loss is minimum [106-107]. Generally, QDs are used as photon absorbing elements in OPVs but, the addition of QDs can alter the mechanism of charge transport and carrier recombination in the device due to various phenomena such as carrier injection/extraction between bulk material and QDs, tunneling of carriers among QDs, and recombination in QDs. So, a model that includes the above-stated mechanisms in QDs is needed to analyze the effects of altered transport and recombination phenomenon on the device performance.
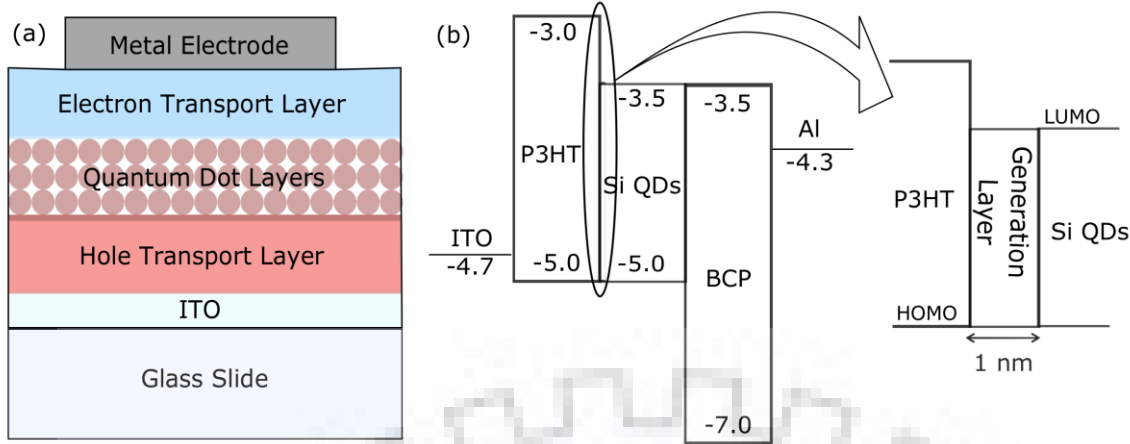
Figure 3.1 (a) Schematic of the modeled device and (b) corresponding flat band energy band diagram of a quantum dot organic solar cell. The energy levels are taken in *eV* with respect to the vacuum level.

I have earlier modeled a simple p-n junction organic diode and validated our modeled results through device fabrication. As the same model can be used for OPVs, I have extended this model for the study of QD based solar cells. I have modeled a photovoltaic device based on Si QDs because Si QDs are easy to fabricate and have a wide range of bandgap tunability [102, 108]. Silicon quantum dots (Si QDs) have good compatibility with poly (3-hexylthiophene) (P3HT) and bathocuproine (BCP) materials due to suitable energy level alignment as shown in Fig. 3.1(b), so those two materials are chosen as hole and electron transport layers, respectively.

S. Gustavsson *et al.* [75] and D. Weinmann *et al.* [76] have reported an exhaustive study on the microscopic single-electron transport through the QDs at low temperatures. The present work entails modeling the charge transport in quantum dots and subsequently, makes a complete model for the quantum dot organic photovoltaic device. The developed model starts from the photon absorption, all the way to the charge collection at electrodes by considering the charge transport through the QDs, recombination in QDs and charge transport through the bulk materials [28].

2. Model Description

The schematic of the proposed device structure and corresponding band energy diagram are shown in Fig. 3.1 (a) and (b) respectively. The QD layers are sandwiched between P3HT and BCP layers. The P3HT layer in the device acts as a photon-absorber and hole transport layer while the BCP layer acts as the electron transport layer. Indium tin oxide, the transparent front electrode acts as the anode of the device and also allows photon penetration in the device. Aluminum acts as a back contact which collects the electrons from the device (cathode) and at

the same time, acts as a reflective layer which increases the absorption of photons in the device. The photons reach the active region of the device through the transparent anode and get absorbed in the P3HT layer causing exciton generation. These excitons, then, diffuse through the P3HT and reach the interface of the P3HT and QD layer. Then, they dissociate into free carriers by transferring the electrons to the LUMO of QDs while hole remains in HOMO of P3HT, so, there is a mismatch in the boundary conditions of electron and hole currents at the interface (from a simulation point of view). To avoid the mismatch condition in currents, a thin layer so called generation layer with appropriate energy level alignment is assumed between P3HT and QD layers, whose HOMO and LUMO are equal to the HOMO of P3HT and LUMO of QDs layer respectively. Zinc phthalocyanine (ZnPc) is a well-suited material for the generation layer [109]. Free carrier generation occurs only in this layer with the rate of exciton dissociation and due to small thickness and perfect band alignment, hole generation in P3HT and electron generation in QDs can be considered as hole and electron generation in the generation layer thus, the mismatch in boundary condition is resolved [110-111]. Unabsorbed photons from P3HT are transmitted into the QD layer which generates free carriers in the quantum dots without excitonic charge transfer. Finally, the free carriers are transported and collected by the respective electrodes. So, the device can be modeled by including the following processes:

a.   Carrier injection/extraction between transport layers and QD layers
b.   Charge transport through the QD layers
c.   Recombination in quantum dots
d.   Exciton generation and dissociation into free carriers
e.   Coupled rate equations in the various regions of QD layers
f.   Charge transport in HTL and ETL
g.   Charge collection at electrodes
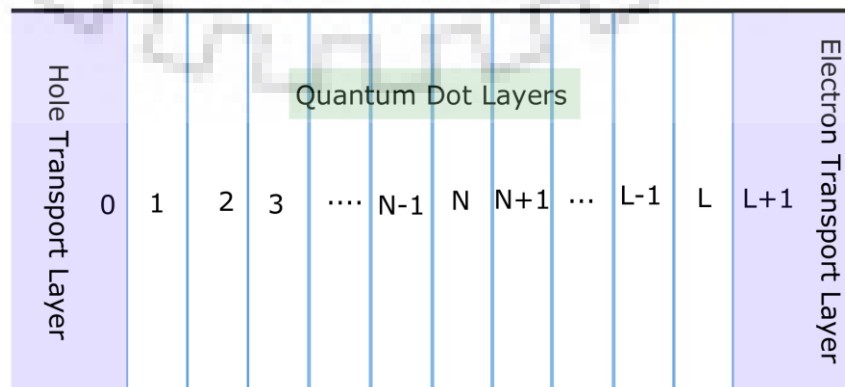
Figure 3.2 Discretization scheme for quantum dot layers in the device.

a. Carrier injection/extraction between transport layers and QD layers

To model the transfer of charges from transport layers to QD layers, the first QD layer can be considered as carrier traps. In the state of equilibrium, the emission and capture rates at the traps must be equal. For holes, that can be written mathematically as

$$e_0 p_0(1) = c_0 p_0(0)[N_T - p_0(1)] \qquad (1a)$$

where c is the capture rate coefficient and e is the emission rate coefficient for the trap sites, $p(1)$ is the hole concentration in the first QD layer and $p(0)$ is the hole concentration in the transport layer at the interface, N_T is the density of trap sites in the QD layer. The trap density is limited by the number of QDs in a layer because each quantum dot can trap only few carriers. In the equation, the subscript (0) stands for equilibrium.

The rate of change of hole concentration is the difference between emission and capture rates and can be written as

$$\frac{\partial p}{\partial t} = cp(0)[N_T - p(1)] - ep(1) \qquad (1b)$$

If the device is not too far from the equilibrium, the emission and capture rate coefficients can be assumed to be equal to the equilibrium values. Assuming the hole concentration to be much smaller than the density of traps, Eq. 1b can be written as

$$\frac{\partial p}{\partial t} = \frac{1}{\tau_{pl}}\left[\frac{p(0)}{p_0(0)}p_0(1) - p(1)\right] \qquad (1c)$$

where $\tau_{pl}(= 1/e_0)$ is the emission/capture time constant and depends on the materials at the interface. Similarly, the rate of change of electron concentration can be derived.

b. Charge transport through the QD layers

The charge transport among the QDs is not possible through the band transport mechanism because an insulating layer surrounds the QDs. The insulating layer is used to protect or control the size of quantum dots or do both [112]. The thin insulating layer creates a narrow potential barrier between two QDs and quantum dot itself acts as a potential well. Hence, charge carriers move from one quantum dot to another through tunneling process.

The tunneling probability from QD layer 1 to layer 2 (see Fig. 3.2) can be approximated by one-dimensional WKB approximation and written as [45]

$$T_{12} = \exp\{-2\kappa(2d_{Barrier})\} \tag{2}$$

where $\kappa = \sqrt{\frac{2m}{\hbar^2}(V_0 - E)}$ is the inverse characteristic length for tunneling and $d_{Barrier}$ is the thickness of potential barrier which is equal to the thickness of insulating layer around the quantum dot core.

The electrons in the potential well can be assumed to be oscillating with oscillation frequency,

$$\nu = \frac{v_{th}}{2d_{Well}} \tag{3}$$

where v_{th} is the thermal velocity of electrons and d_{Well} is the width of the potential well i.e. diameter of the quantum dot core.

The number of electrons tunneling per second from layer 1 to layer 2 is given by

$$N_{1 \to 2} = n_1 \nu T_{12} \tag{4a}$$

where n_1 is the number of electrons in layer 1.

The tunneling probability and the oscillation frequency are same in all QDs for all layers. Thus, the total number of electrons tunneled per second from layer 2 to layer 1 is

$$N_{2 \to 1} = n_2 \nu T_{21} \tag{4b}$$

Now, net flow of electrons from layer 1 to layer 2 is

$$N_{1 \to 2} - N_{2 \to 1} = n_1 \nu T_{12} - n_2 \nu T_{21} \tag{4c}$$

Hence, the above balance equation can be rewritten in terms of equilibrium carrier concentrations as

$$N_{1 \to 2} - N_{2 \to 1} = w_{12}\left(n_1 - \frac{n_{1_0}}{n_{2_0}}n_2\right) \tag{4d}$$

where $w_{12} = \nu T_{12}$ and n_{1_0} and n_{2_0} are the equilibrium electron concentrations in layer 1 and layer 2 respectively. Similar equations can be written for the hole transport.

c. Recombination in quantum dots

Direct band to band recombination of charge carriers in the QDs can be defined in a similar way to the Langevin bimolecular recombination mechanism because QDs are generally undoped and recombination rate depends on the concentration of both types of carriers, hence the bimolecular recombination rate is [98][23]

$$R_{Bimolecular} = \gamma(np - n_i^2) \tag{5a}$$

where γ is the bimolecular recombination coefficient, n, p, and n_i are the electron, hole, and intrinsic concentrations, respectively.

Furthermore, trap assist recombination process is also in the context of carrier recombination. Trap assist recombination rate can be described as Shockley-Read-Hall (SRH) recombination

$$R_{SRH} = \frac{np - n_i^2}{\tau_n(p + n_1) + \tau_p(n + p_1)} \tag{5b}$$

where τ_n and τ_p are the electrons and holes lifetime respectively.

Assuming the lifetime of electrons and holes are equal and the carrier concentrations are much higher than n_1 and p_1.

Now, the recombination rate can be rewritten as

$$R_{SRH} = \frac{np - n_i^2}{\tau_r(p + n)} \tag{5c}$$

For the quantum dots, both recombination processes take place simultaneously, so total recombination rate is

$$R = R_{Bimolecular} + R_{SRH} = \gamma(np - n_i^2) + \frac{np - n_i^2}{\tau_r(p + n)} \tag{5d}$$

d. Exciton generation and dissociation into free carriers

Organic materials have low dielectric constant and on absorption of light, the excitons are generated in absorbing layer. The excitons are hard to dissociate into free carriers by themselves, so excess energy is needed to dissociate them. The presence of discontinuity in electron affinity at the donor-acceptor interface causes efficient dissociation of exciton into free carriers.

The whole process, from photon absorption to free carrier generation is modeled by including the following set of equations:

i.   It is assumed that excitons are generated only in the absorbing layer. The profile of exciton generation rate in the absorbing layer can be described by

$$G_{ex}(x) = \int_0^\infty N_{ph}(\lambda).\alpha(\lambda)(1 - R_{loss}).\exp(-\alpha(\lambda).x)d\lambda \tag{6a}$$

where $N_{ph}(\lambda)$ is the number of photons of wavelength λ per unit time, $\alpha(\lambda)$ is the absorption coefficient of the absorbing material, R_{loss} is the reflection loss at front surface and x is the depth inside the device measured from the front surface.

ii. The exciton concentration at both electrodes is assumed to be zero due to infinite relaxation rate and the exciton dissociation into free electron and hole is significant in the presence of discontinuity in electron affinities at the heterojunction so, the excitons not only diffuse towards the dissociating interface but also diffuse towards the electrodes, hence exact exciton distribution can be obtained by solving the diffusion equation

$$\frac{\partial s(x)}{\partial t} = G_{ex}(x) - \frac{s(x)}{\tau_{ex}} - k_{diss}(x)s(x) + \frac{L_D^2}{\tau_{ex}}\frac{\partial^2 s(x)}{\partial x^2} \tag{6b}$$

where $s(x)$ is the exciton concentration, τ_{ex} is the exciton lifetime, $k_{diss}(x)$ is the exciton dissociation rate coefficient and L_D is the diffusion length of excitons.

iii. Finally, the free carriers generation rate which is equal to the rate of exciton dissociation is written as

$$G(x) = k_{diss}(x) \times s(x) \tag{6c}$$

e. **Coupled rate equations**

Fig. 3.2 shows the way the quantum dot layers have been modeled and labeled with label 1 denoting the first QD layer and L denoting the Lth QD layer. Label 0 and L+1 correspond to points in HTL and ETL, respectively, at the QD-transport layer interfaces. The transport equations for electrons can be written as [28]

$$\frac{dn(1)}{dt} = \frac{1}{\tau_{n,0\to1}}\left[\frac{n(0)}{n_0(0)}n_0(1) - n(1)\right] - w_{n,1\to2}\left[n(1) - \frac{n_0(1)}{n_0(2)}n(2)\right] - \gamma_2[n(2)p(2) - n_{i2}^2] -$$

$$\gamma_1\left[\frac{n(1)p(1)-n_i^2}{\tau_r(n(1)+p(1))}\right] + G(1) \tag{7a}$$

$$\frac{dn(2)}{dt} = w_{n,1\to2}\left[n(1) - \frac{n_0(1)}{n_0(2)}n(2)\right] - w_{n,2\to3}\left[n(2) - \frac{n_0(2)}{n_0(3)}n(3)\right] - \gamma_2[n(2)p(2) - n_{i2}^2] -$$

$$\left[\frac{n(2)p(2) - n_{i2}^2}{\tau_r(n(2)+p(2))}\right] + G(2) \tag{7b}$$

$$\frac{dn(N)}{dt} = w_{n,N-1\to N}\left[n(N-1) - \frac{n_0(N-1)}{n_0(N)}n(N)\right] - w_{n,N\to N+1}\left[n(N) - \frac{n_0(N)}{n_0(N+1)}n(N+1)\right] -$$

$$\gamma_N[n(N)p(N) - n_{iN}^2] - \left[\frac{n(N)p(N) - n_{iN}^2}{\tau_r(n(N)+p(N))}\right] + G(N) \tag{7c}$$

$$\frac{dn(L)}{dt} = w_{n,L-1\to L}\left[n(L-1) - \frac{n_0(L-1)}{n_0(L)}n(L)\right] - \frac{1}{\tau_{n,L\to L+1}}\left[n(L) - \frac{n_0(L)}{n_0(L+1)}n(L+1)\right] -$$

$$\gamma_L[n(L)p(L) - n_{iL}^2] - \left[\frac{n(L)p(L) - n_{iL}^2}{\tau_r(n(L)+p(L))}\right] + G(L) \tag{7d}$$

The transport equations for holes can be written in a similar fashion.

f.   Charge transport in HTL and ETL

The drift-diffusion approximation is used to describe the charge transport in each transport layer. It is described by a set of continuity equations for holes and electrons and Poisson's equation as follows:

$$\frac{\partial p}{\partial t} = -\frac{1}{q}\cdot\frac{\partial J_p}{\partial x} - R + G \tag{8a}$$

$$\frac{\partial n}{\partial t} = \frac{1}{q}\cdot\frac{\partial J_n}{\partial x} - R + G \tag{8b}$$

$$\frac{\partial^2 \psi}{\partial^2 x} = -\frac{q}{\varepsilon}(N_d - N_a + p - n) \tag{8c}$$

where,

$$J_p = -qD_p\frac{\partial p}{\partial x} - qp\mu_p\frac{\partial \psi}{\partial x} \tag{8d}$$

$$J_n = qD_n\frac{\partial n}{\partial x} - qn\mu_n\frac{\partial \psi}{\partial x} \quad . \tag{8e}$$

The generation rate is assumed to be zero under dark condition but under illumination, the generation rate is significant only at donor-acceptor heterojunction (i.e. in generation layer) and negligible in bulk material. Generation has already been explained in section D and the generation profile is assumed to be the same for all calculations. Recombination in the transport

layers is modeled by Shockley-Read-Hall recombination. Assuming trap centers are at intrinsic energy level, the recombination rate is given by,

$$R = \frac{pn - n_i^2}{\tau_p(n + n_i) + \tau_n(p + n_i)} \qquad (9)$$

g. Charge collection at electrodes

The transport layers are doped with respective n-type or p-type impurities to minimize the effects of low carrier mobility. Both the electrodes are assumed to be ohmic, so these metal-semiconductor interfaces will be in thermal equilibrium and the carrier concentrations are equal to the equilibrium concentration. These relations are considered as the boundary conditions for our calculations [33, 98]

At the anode:

$$p(0).n(0) = n_i^2(0) \qquad (10a)$$

$$N_d(0) - N_a(0) + p(0) - n(0) = 0 \qquad (10b)$$

$$\psi(0) = V_{app} - \frac{kT}{q}\ln\left[\frac{p(0)}{n(0)}\right] \qquad (10c)$$

And at the cathode:

$$p(L).n(L) = n_i^2(L) \qquad (10d)$$

$$N_d(L) - N_a(L) + p(L) - n(L) = 0 \qquad (10e)$$

$$\psi(L) = \frac{kT}{q}\ln\left[\frac{p(L)}{n(L)}\right] - \left(\frac{\Delta E_C + \Delta E_V}{2}\right) \qquad (10f)$$

where N_a and N_d are the doping concentrations of P3HT and BCP, respectively, V_{app} is the applied bias, kT/q is the thermal potential, and ΔE_C, & ΔE_V are the discontinuities in the conduction and valence bands, respectively. Detailed analysis of electrode potential in presence of band discontinuities is given by Anderson [113] and K. Yang *et. al.* [114] The electrode potential is not affected by energy levels of QD layers; it only depends on the Fermi levels of end materials.

3. Results and Discussions

The schematic of the photovoltaic device is shown in Fig. 3.1(a). The thickness of P3HT which is considered as the photon absorbing HTL is 60.0 nm while the thickness of BCP, acting as ETL is 55.0 nm. 5 quantum dot layers have been sandwiched between the P3HT and BCP layers. Each quantum dot has 4.0 nm core diameter and 0.5 nm thick silicon oxide (SiO₂) shell as a passivation layer. A 1.0 nm ZnPc (generation layer) is assumed between the P3HT and QDs resulting in the total device thickness of 141.0 nm.

Furthermore, in chapter 2, it is found that the charge transport in the device is very sensitive to the change in electrode barriers, carrier mobility, and device thickness etc. To analyze the effect of quantum dots on the device performance, it is required to minimize the effects of other parameters on charge transport so, both the transport layers are doped with majority carriers ($5{\times}10^{16}$ cm^{-3}) which improves the transport properties of respective layers and reduces the effects of low carriers mobilities, imbalanced mobilities, nature of contacts, etc. on the device performance [111, 115]. The electrical parameters for the P3HT and BCP layers are taken from the previous reports and assumed constant as listed in Table 3.1.

TABLE 3.1 The parameters of P3HT and BCP used for the model device.

Parameters (symbol)	P3HT	BCP
Doping Concentration	$N_A = 5 \times 10^{16}\ cm^{-3}$	$N_D = 5 \times 10^{16}\ cm^{-3}$
Hole mobility, μ_p [116]	$0.1\ cm^2/Vs$	$0.001\ cm^2/Vs$
Electron mobility, μ_n	$0.001\ cm^2/Vs$	$0.1\ cm^2/Vs$
Band gap, E_g [108]	$2.0\ eV$	$7.0\ eV$
Electron affinity, χ	$3.0\ eV$	$3.5\ eV$
Carrier Lifetime, $\tau_p = \tau_n$	$1.0\ \mu s$	$1.0\ \mu s$
Dielectric constant, ε [117]	$4.5\ \varepsilon_0\ F/cm$	$4.5\ \varepsilon_0\ F/cm$

Various electrical parameters for the quantum dots are given in table 3.2. The electron affinity and bandgap of silicon quantum dots as a function of particle size are well explored by D. Das and A. Samanta [118]. Intrinsic carrier concentration is obtained from the exponential relation between n_i and the bandgap of QDs. Tunneling probability is calculated by assuming WKB approximation, which gives the tunneling coefficient between QDs. We have assumed that the tunneling coefficient is same for electrons and holes. The SRH recombination time constant for QDs has been taken from the work by Sobolev *et al.* [119].

TABLE 3.2 The parameters of quantum dot layers used in the model.

Parameters (symbol)	Values (unit)
Tunneling coefficient, w [28]	$1.42 \times 10^{10}\ s^{-1}$
Capture/emission coefficient, $\tau_{pl} = \tau_{nl} = \tau$	$1.0 \times 10^{-10}\ s$
Bimolecular recombination coefficient, γ	$4 \times 10^{-10}\ cm^3 s^{-1}$
SRH recombination lifetime, $\tau_p = \tau_n$	$1.2\ \mu s$
Bandgap, E_g [118]	$1.5\ eV$
Electron affinity, χ	$3.5\ eV$

The wavelength-dependent photon flux is calculated by Plank radiation law, assuming the sun's temperature to be 5700 K. Theoretical calculations revealed that about 1×10^{17} photons per cm^2/s are equivalent to 100 mW/cm^2 solar power density. The bandgap of P3HT is around 2.0 eV hence it absorbs radiation below 620 nm [120]. Absorption coefficient has been assumed to be independent of the wavelength. Absorption in QDs has been neglected because it is very low compared to the absorption in the P3HT layer.

3.1. Simulation results

The device shown in Fig. 3.1(a) is simulated in dark condition, for zero bias and 0.7 volts forward bias and corresponding carrier density and potential distribution profiles are plotted in Fig. 3.3. The potential across the device decreases from 0.9 V (built-in potential) to 0.2 V for 0.7 V applied bias. The logarithmic plot of carrier distribution is in good agreement with the position of Fermi level and band bending in equilibrium. Due to large bandgap and significant doping in transport layers, the minority carrier concentrations are negligible and do not play any significant role in charge transport. The QD layers are undoped and respective carriers are injected from the HTL and ETL, hence the carrier densities are much larger than the intrinsic carrier concentration in the QD layers. The high electron and hole densities are responsible for charge transport in QD layers. On applying forward bias, the carrier density in the transport layers increases, hence carrier injection at the interfaces between the transport layers and QD layer also increases, which results in an increase in carrier concentration in QD layers and the current in the device.
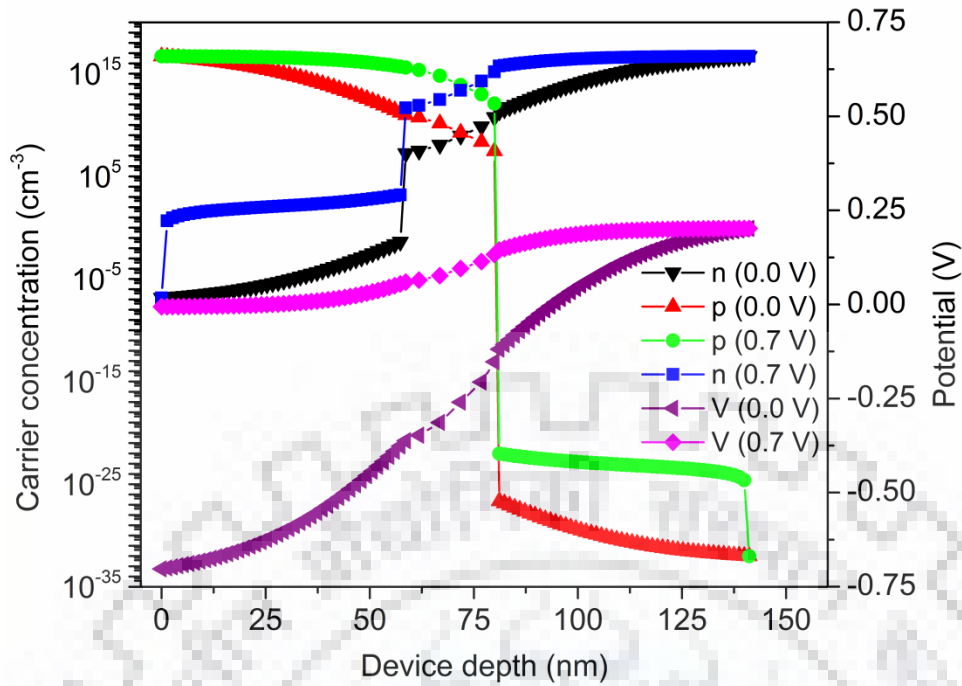
Figure 3.3 Carrier concentration and potential distribution in the device at equilibrium and 0.7 V applied bias under dark condition.

The QD parameters capture time constant, bimolecular recombination coefficient, and SRH recombination lifetime are assumed to be 1×10^{-9} s, 4×10^{-10} cm^3/s, and 1×10^{-6} s, respectively. The current density-voltage (J-V) characteristics of the device are plotted in Fig. 3.4 for the chosen parameters. The applied voltage is varied from -1.0 V to 10.0 V and current density and magnitude of current density are mapped on linear and logarithmic scales, respectively. The value of current is found to be almost constant (0.5 pA/cm^2) under reverse bias condition. The current density increases exponentially with increasing forward bias (up to 1.5 V). At the higher applied bias, the current is limited by the series resistance of the bulk material and increases linearly.

It is difficult to estimate the capture/emission time constant (τ) between the QDs and transport layers. To illustrate the effects of τ on the J-V curve, τ is varied over a large range (1×10^{-6} s to 1×10^{-12} s) and corresponding magnitude of current densities are plotted (Fig. 3.4) against applied voltage on a semi-logarithmic scale. The graph shows a reduction in current density when τ is in the range of few microseconds and the J-V curves for $\tau = 1\ ns$ and $\tau = 1\ ps$ overlap perfectly. Thus, J-V characteristic is unaffected below $1\ ns$ capture/emission time constant. At large values of τ, the series resistance of the device increases, resulting in decrease in current density.
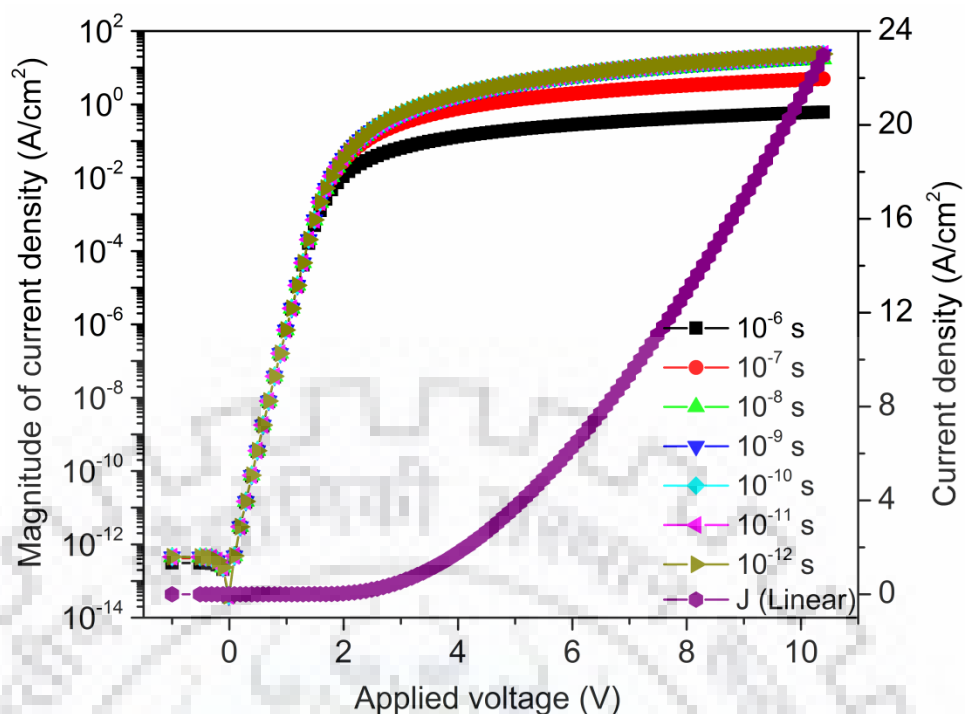
Figure 3.4 Magnitude of current density vs applied voltage for the various values of the capture/emission coefficient on a logarithmic scale and on a linear scale, current density vs applied voltage at 1.0 ns capture/emission coefficient.

3.2. Device under illumination
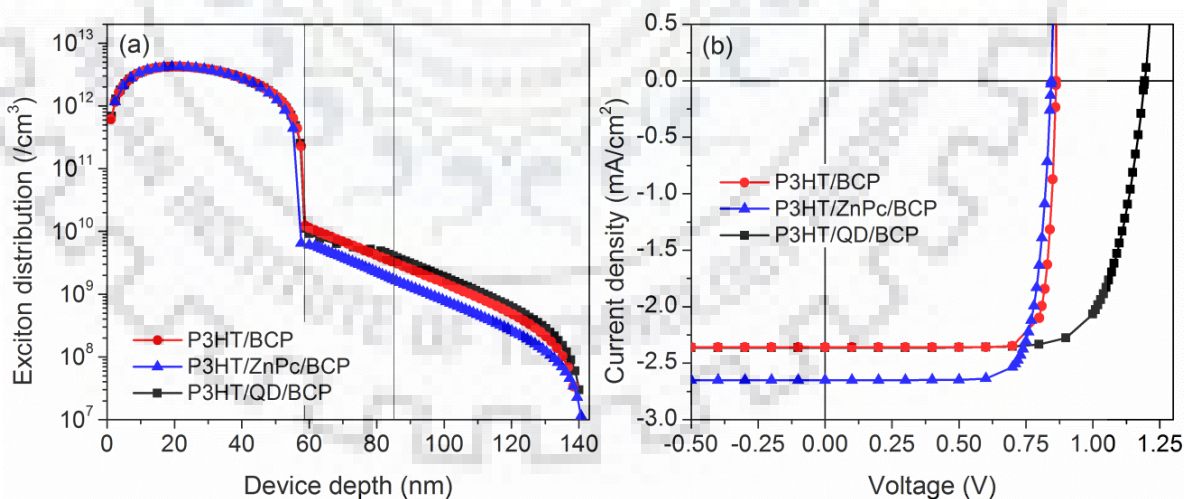
Figure 3.5 (a) Exciton distribution and (b) J-V characteristics of corresponding devices (bilayer, trilayer, and modeled QD based device) under illuminated conditions.

To illustrate the effect of the addition of cascaded QD layers on the performance of OPVs, we compare the exciton density profile and J-V curves of a bilayer (P3HT/BCP) structure, a trilayer (P3HT/ZnPc/BCP) structure, both without QDs, and the modeled device

which contains QDs. The total device thickness and absorbing layer thickness are kept same in all devices and the thickness of ZnPc layer in trilayer structure is kept equal to the thickness of QD layers. All the devices are illuminated at a power density of 100 mW/cm^2. Fig. 3.5(a) shows the exciton distribution in various devices, the exciton densities in all the devices are approximately same hence; changes in J-V characteristic of corresponding devices (Fig. 3.5(b)) are mainly due to the variation in charge transport and recombination in central layer. Further, we have extracted the short circuit current density (J_{SC}) and the open-circuit voltage (V_{OC}) for QD based devices which are found to be 2.36 mA/cm^2 and 1.19 V respectively. The V_{OC} for the device with QDs is significantly higher compared to devices without QDs. J-V characteristic also revealed a good fill factor (FF)~0.73 and improved power conversion efficiency (PCE) of 2.06 % as compared to bilayer (PCE=1.67 %) and trilayer (PCE=1.78 %) structures. These calculations clearly show that QDs significantly improve device characteristics.
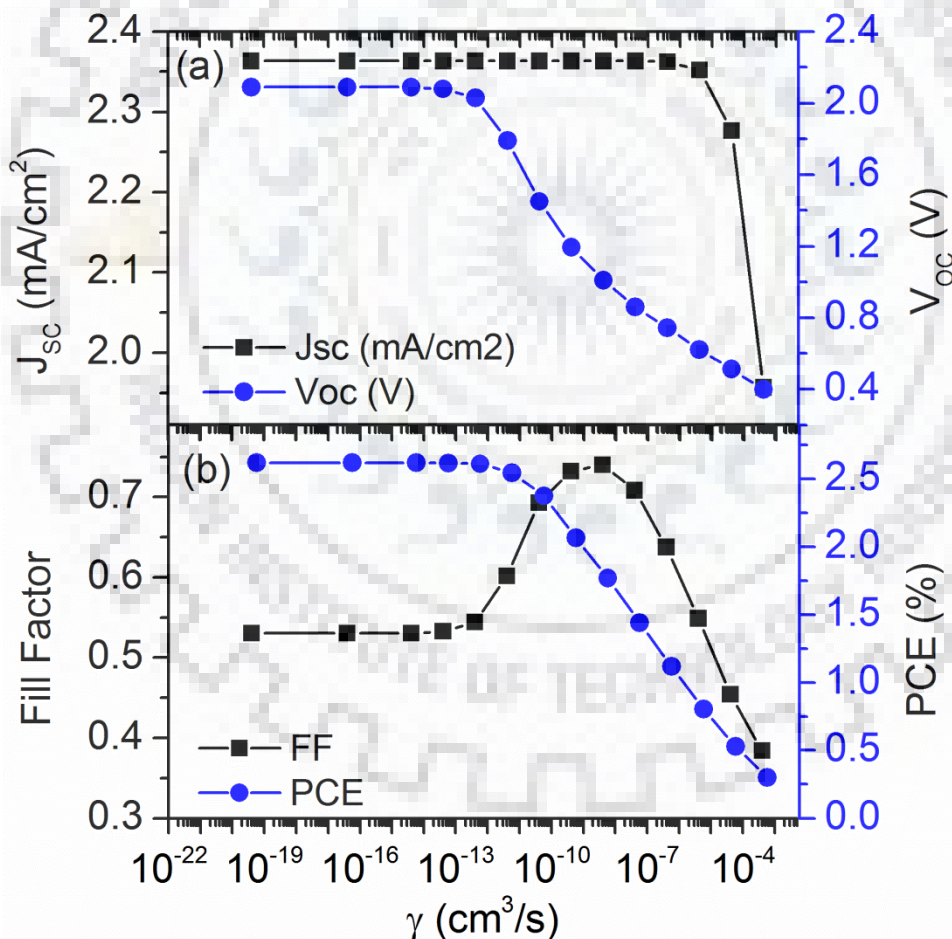
Figure 3.6 (a) Variation in the J_{SC} and V_{OC} and (b) variation in FF and PCE with bimolecular recombination coefficient in quantum dots.

Now that we have established that QDs can improve device performance, let us study how a QD based solar cell can be improved to give the best possible performance. Bimolecular recombination coefficient (γ) and size are the important design parameter for the quantum dots. These parameters may be easily tuned according to the requirement [121-122]. To illustrate the effects of γ on the solar cell parameters, γ is varied from 4×10^{-4} cm^3/s to 4×10^{-20} cm^3/s, keeping all other parameters constant and corresponding J_{SC}, V_{OC}, FF, and PCE are plotted in Fig. 3.6. The short circuit current density is observed to decrease linearly from 2.35 to 1.95 mA/cm^2 on increasing γ from 4×10^{-6} to 4×10^{-4} cm^3/s. However, the V_{OC} is found to be 0.4 V when γ is 4×10^{-4} cm^3/s and increases exponentially on reducing γ and finally it gets saturated to 2.09 V for the values of γ below 10^{-13}cm^3/s. At higher values of γ, optically generated excess carriers in the QD layers quickly recombine and do not play any role in photovoltaic phenomenon resulting in low values of V_{OC} and J_{SC}. Enhanced V_{OC} at lower values of γ may be attributed to reduced dark current and enhanced charge concentration in the device due to reduction in recombination in QD layers [123]. Fill factor has a complex relationship with γ, it can be attributed to variation in parasitic resistances of the device with γ, as shown in Fig. 3.7. It is observed that the shunt resistance (R_{sh}) increases with decreasing γ due to diminishing photocarrier recombination in QD layers but the series resistance (R_s) is varying non-monotonically possibly due to the competition between resistance of the QD layers and that of the transport layers. At higher values of γ (4×10^{-4} to 4×10^{-9} cm^3/s), recombination in QD layers is very fast which causes reduction in R_s and hence, the resistance of transport layer dominates the series resistance of the device. At lower values of γ, the resistance of QD layers dominates the series resistance of the device. It is observed that the FF strongly follows the variation in R_s. At lower values of γ, the fill factor is saturated to 0.53 and increases to a maximum value of 0.74 when γ is 4×10^{-9} cm^3/s and again decreases exponentially at higher values. As J_{SC}, V_{OC}, and FF get saturated for the lower values of γ, corresponding PCE also gets saturated to a value of 2.62 % and when γ increases above 4×10^{-12} cm^3/s, PCE decreases exponentially.
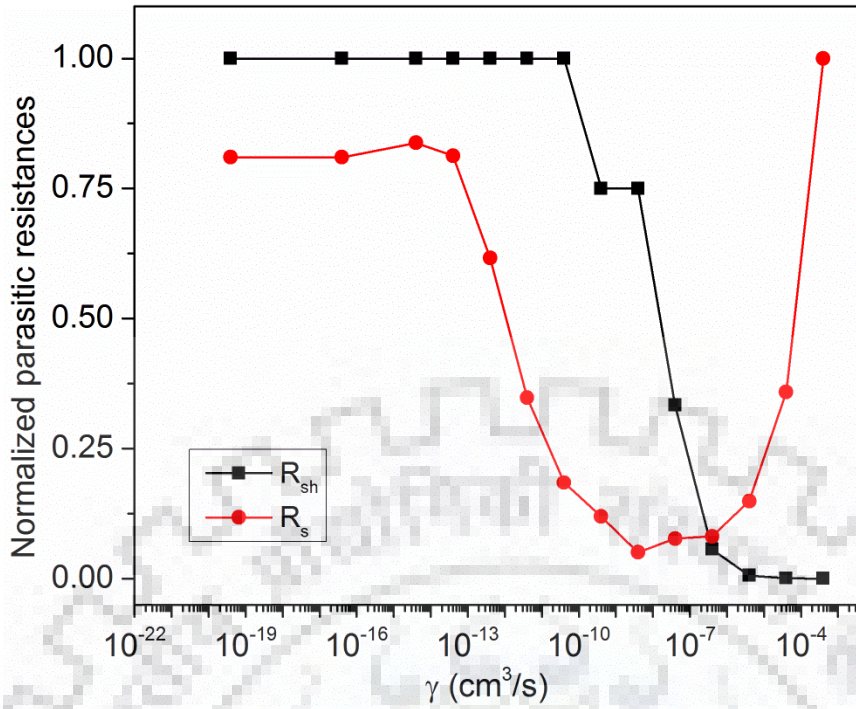
Figure 3.7 Variation in parasitic resistances (normalized) of the device with bimolecular recombination coefficient.
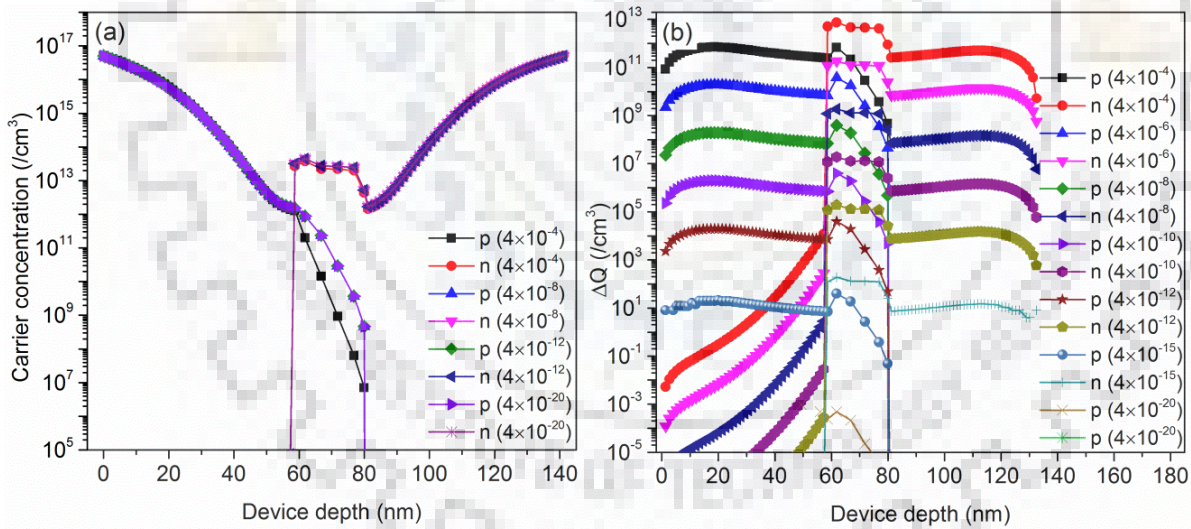
Figure 3.8 (a) Carrier distribution in the device at various values of γ (b) change in carrier concentrations in the device for different values of γ with respect to carrier concentration when γ is zero.

Fig. 3.8 (a) shows the charge distribution in the device under short circuit conditions for various values of bimolecular recombination coefficient, keeping all other parameters constant. From the plot, it is evident that in QD layers the electron concentration is of the order of 10^{14} cm^{-3} which is much higher than the concentration of holes; hence, the electron current controls

the total current in the QD layers. Negligible change in electron concentration gradient in the QDs is the reason why J_{SC} remains constant over the wide range of γ. Fig. 3.8 (b) shows the change in charge concentration (ΔQ) for various values of γ with respect to charge concentration when γ equal to zero (no bimolecular recombination). ΔQ decreases exponentially with decreasing γ. Variations in V_{OC} can be correlated with the change in charge concentration; ΔQ becomes insignificant for values of γ below 10^{-11} cm^3/s and no substantial change in V_{OC} has been observed. As the recombination rate is a non-linear function of charge concentration, J-V curve has a complex relation with γ.

In the chapter, we have modeled a quantum dot organic solar cell that includes several phenomena: carrier injection/extraction between bulk material and QDs, tunneling among QDs, and recombination in QDs at room temperature. When compared to the bilayer and trilayer device structures without QDs, the device performance is improved by adding cascaded QD layers due to better control on charge transport in the device. 1-D numerical analysis of the model is able to explore important parameters that affect the characteristics of the solar cell. The solar cell characteristics mainly controlled by the QD layers [124-127]. Increasing capture/emission time constant restricts the charge transfer between the transport layer and QD layer that results in attenuation in device current due to rise in series resistance of the device. The charge transport and recombination in the device are primarily controlled by the bimolecular recombination coefficient which can be used to tune solar cell parameters, primarily, Voc. At lower values of bimolecular recombination coefficient in QDs, charge carriers escape recombination and reach high enough concentrations so that no significant change is observed in power conversion efficiency on further reduction in the bimolecular recombination coefficient.

Chapter 4

Fabrication of Quantum Dot Solar Cells

1. Introduction

Metal nanoparticles, semiconducting quantum dots, and various nano-structured elements in the active layer are primarily used to improve the absorption of photons and/or electrical parameters of active layer in the photovoltaic devices [59-60]. Efficient charge extraction from the active region and minimum recombination losses are the basic requirements to achieve an efficient photovoltaic device [106]. As it is known that QDs are used as photon absorbing elements in a solar cell but, the addition of QDs can also alter the mechanism of charge transport and carrier recombination in the device due to various phenomena such as carrier injection/extraction between bulk material and QDs, tunneling of carriers among QDs, and recombination in QDs. In our previous study [128], 1-D numerical analysis has been done by considering drift-diffusion approximation of charge transport in HTL and ETL while conduction and recombination in the quantum dot layers are described by a system of coupled rate equations incorporating tunneling and bimolecular recombination in QDs (Chapter-3). It is observed that insertion of QD layers at the interface of traditional donor and acceptor material in a bilayer heterojunction organic solar cell shows improved device performance by controlling the charge transport and carrier recombination in the device with bimolecular recombination coefficient in QDs. So, the direct impact of addition of QDs can be shown on the electrical characteristics of conventional solar cells but such multilayered structures are difficult to fabricate and compare the electrical characteristics with the simulated results.
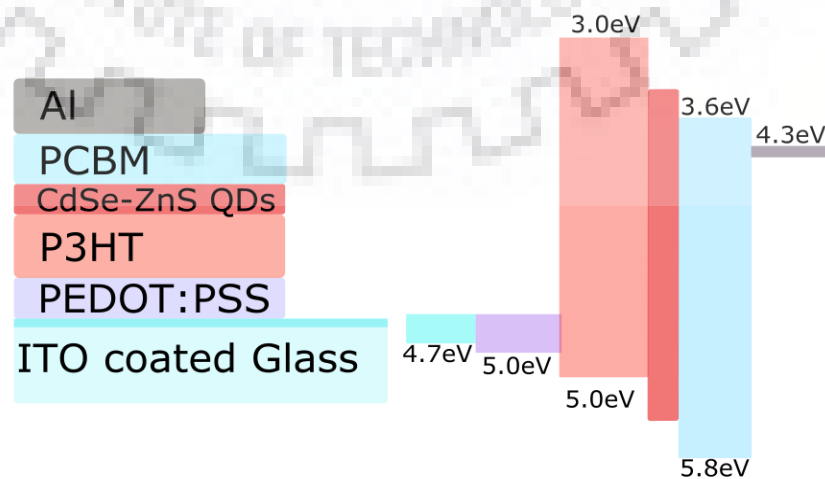
Figure 4.1 Schematic and corresponding energy band diagram of the fabricated device.

In this chapter, experimental results of various fabricated devices have been presented. Various QD based solar cells were fabricated and analyzed the experimental results in order to verify our model of QD-solar cells. To that end, various core-shell quantum dots are synthesized and a thin film of QDs is applied between the donor-acceptor (D-A) interface. But, in physical realization of the device, some additional factors: imbalanced carrier mobility, poor extraction of the carriers at electrodes, injection/extraction barrier between electrodes and active material result in an s-kink in the fourth coordinate of the I-V characteristics of the device which drastically reduces the device performance mainly by reducing the fill factor [129-133]. The effects on the solar cell parameters and the appearance of s-kink in J-V characteristics on insertion of QDs are further analyzed in chapter 5 with the help of our proposed model.

2. Experimental Details

2.1. Quantum Dot Synthesis

a. CdSe-ZnS core-shell QDs

The CdSe-ZnS core-shell QDs have been synthesized by a single-step non-injection technique using CdO (1.6 mmol), $Zn(NO_3)_2.6H_2O$ (0.8 mmol), Se (0.4 mmol), and S (0.8 mmol) as starting materials. The materials were mixed in 20 mL of 1-octadecene (ODE) together with 3.0 mL of trioctylphosphine (TOP) and (4 mmol) of stearic acid (SA) in a 100 mL three-necked flask. The mixture was heated to 250 ˚C under nitrogen environment for 30 minutes with vigorous stirring. Afterward, the solution was cooled down to room temperature and further purified by centrifugation in a 1:3 chloroform/ acetone solvent [49-50]. Finally, the precipitate was collected and dried in vacuum and dispersed in chloroform to make a colloidal solution of QDs.

b. CdS-ZnS white light-emitting QDs (WQD)

The CdS-ZnS core-shell QDs were synthesized using a single-step non-injection process. CdO (2.0 mmol), $Zn(OAc)_2$ (1.0 mmol), S (1.0 mmol), and stearic (4.0 mmol) acid, were mixed in 20 ml of 1-ODE in a three-neck flask at room temperature with constant stirring. The mixture temperature was slowly increased to 100 °C for proper mixing and after 5 min; the temperature was set to 260 °C for 30 min. The collected samples were washed multiple times with mixture of chloroform and acetone (1:3) and centrifuged at 10000 rpm for 10 min. Thus, precipitated QDs were collected and stored by dispersing in chloroform to form a colloidal solution.

2.2. Device Fabrication

Schematic of the device is shown in Fig. 4.1 which is realized with the given fabrication procedure. ITO coated glass (~280 nm; ~10 Ω/sq) substrates were cleaned in ultrasonic bath sequentially with DI-water, acetone, and 2-propanol for 10 minutes each at 50 ˚C and dried by blowing nitrogen gas. The cleaned ITO substrates were then ozonized for 15 minutes to remove organic contaminants and provide better adhesion to poly (3,4-ethylene dioxythiophene): poly (styrene sulfonate) (PEDOT:PSS) layer.

The PEDOT:PSS solution was filtered by PVDF filters of pore size of 0.45 μm and spin-coated on the ITO glass substrates at a spin speed of 4000 rpm for 30 seconds. The samples were annealed for 15 minutes at 110˚C. Afterward, the solutions for active layers were prepared by dissolving poly (3-hexylthiophene) (P3HT), Phenyl-C60-butyric acid methyl ester (PCBM), and QDs in dichlorobenzene (DCB), dichloromethane (DCM), and dimethylformamide (DMF) respectively, keeping 10 mg/ml concentration of each. Used solvents are orthogonal which avoids dissolving of already deposited layers. For bulk heterojunction, dichlorobenzene is used in which required materials are added at a time in the solvent. The filtered P3HT and QD solutions were spin-coated one by one at 2000 rpm for 2 minutes to get dried film after that PCBM solution was coated at 5000 rpm for 30 seconds. The samples were prebaked at 100 ˚C for 15 minutes. Finally, the samples were transferred into thermal evaporator chamber and aluminum contacts of thickness 150 nm were deposited at a base pressure of 10^{-6} Torr and deposition rate of 1 Å/s. The final devices were heated at 150 ˚C for 15 minutes in an inert environment and thus the devices are ready for further electrical, optical, and structural/morphological characterizations.

2.3. Characterizations Tools

a. Optical Measurement (absorption and emission spectrum) of dispersed QDs and active layer were carried out with the help of a USB 4000 Ocean Optics spectrometer attached to a cuvette holder and an integrating sphere.

b. Electrical Measurements (J-V characteristics) of the devices were measured with HP parameter analyzer and probe station integrated with xenon lamp and optical power meter.

c. Structural/morphological Measurement such as XRD diffractogram of the fabricated QDs was recorded by Bruker, D8-Advance XRD system. To know the size and shape of the QDs, the carbon-coated copper grid of 300 mesh was used for taking transmission electron microscopy (TEM) image using JEOL JEM-3200 FS. The layer cross-section and surface roughness were characterized by Carl Zeiss Ultra Plus Field Emission Scanning Electron

Microscope (FESEM) and NT-MDT NATEGRA Atomic Force Microscope (AFM) respectively.

3. Results and Discussions

3.1. CdSe-ZnS QDs based solar cell

The CdSe-ZnS quantum dots were synthesized according to the process mentioned in previous section 2.1.1. Initially, the QDs were dispersed in chloroform and absorption & photoluminescence (PL) spectra were recorded. As shown in Fig. 4.2 (a), the first absorption peak and PL emission measured at excitation wavelength of 405 nm correspond to the bandgap of ~2 eV of the QDs. Transmission electron microscopy image shown in Fig. 4.2 (b) indicates ~6 nm diameter of particles which also corresponds to ~2.0 eV bandgap according to the plot of radius versus band gap variation of CdSe QDs [134] and highest occupied molecular orbital & lowest unoccupied molecular orbital levels of the QDs are compatible with used donor and acceptor materials.
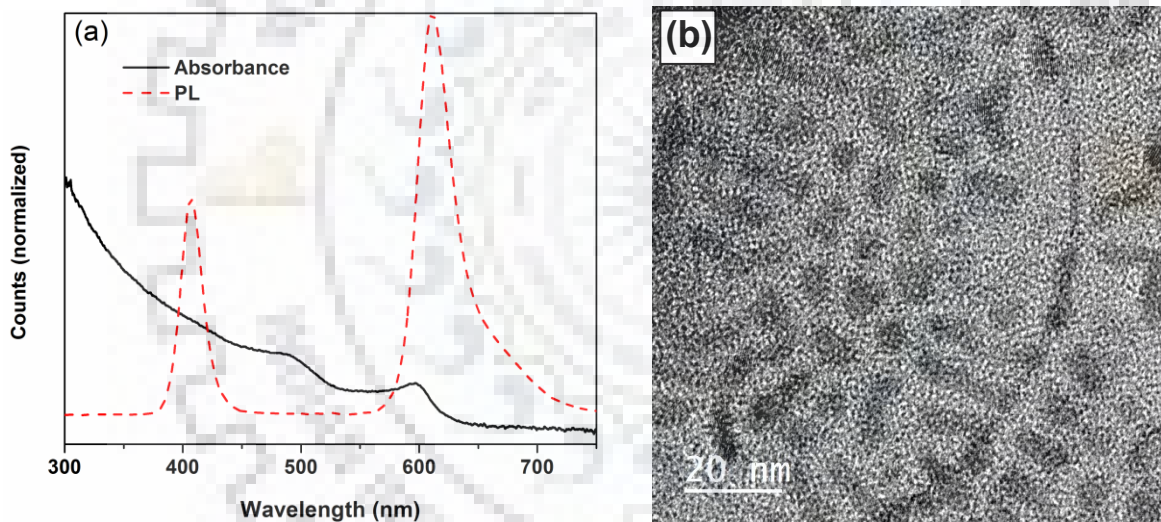
Figure 4.2 (a) Photoluminescence and absorbance spectra (b) Transmission electron microscopy image of CdSe-ZnS core-shell quantum dots

The absorption spectrum of the final device integrated with QDs interlayer is compared with the spectrum of a bilayer heterojunction device without QDs and the recorded spectra are plotted in Fig. 4.3. The QDs in the device enhance the photon absorption for a specific wavelength range below 600 nm as expected from the PL and absorbance spectra (Fig. 4.2 (a)) of chloroform dispersed QDs.
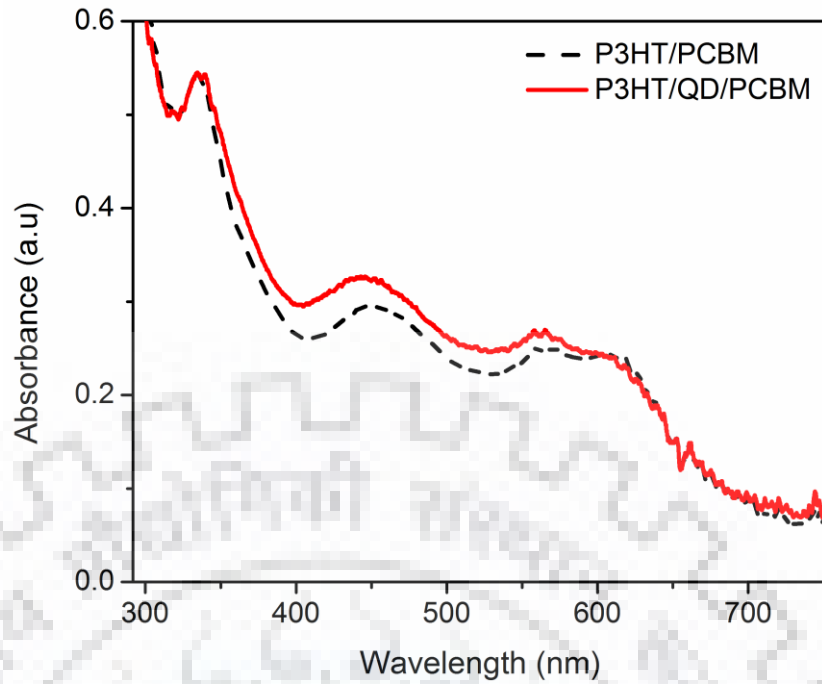
Figure 4.3 Variation in optical absorbance of the bilayer (P3HT/PCBM) heterojunction solar cell on introducing QD layer at the donor-acceptor interface.

Figure 4.4 shows the J-V characteristics of the device. They are measured with HP parameter analyzer and probe station integrated with xenon lamp and optical power meter. In the numerical simulation, optical absorption in QDs was assumed to be zero so that the photocurrent did not increase and variations in fill factor were directly attributed to improvement in charge transport in the device. The J-V characteristic of the device with QD interlayer shows increase in J_{SC} from 0.21 mA/cm^2 to 0.41 mA/cm^2 due to the enhancement in optical absorption in QDs. But, the fill factor and shunt resistance of the device is drastically reduced along with decrease in series resistance of the device (see Table-4.1). Consequently, the device performance is reduced.

TABLE 4.1 Solar cell parameters in the devices.

Parameters	P3HT/PCBM	P3HT/CdSe-ZnS/PCBM
V_{OC} (V)	0.4	0.45
J_{SC} (mA/cm^2)	0.216	0.41
FF	34.38	23.27
R_S (ohm/cm^2)	1088.76	819.84
R_{SH} (ohm/cm^2)	2638.65	897.14
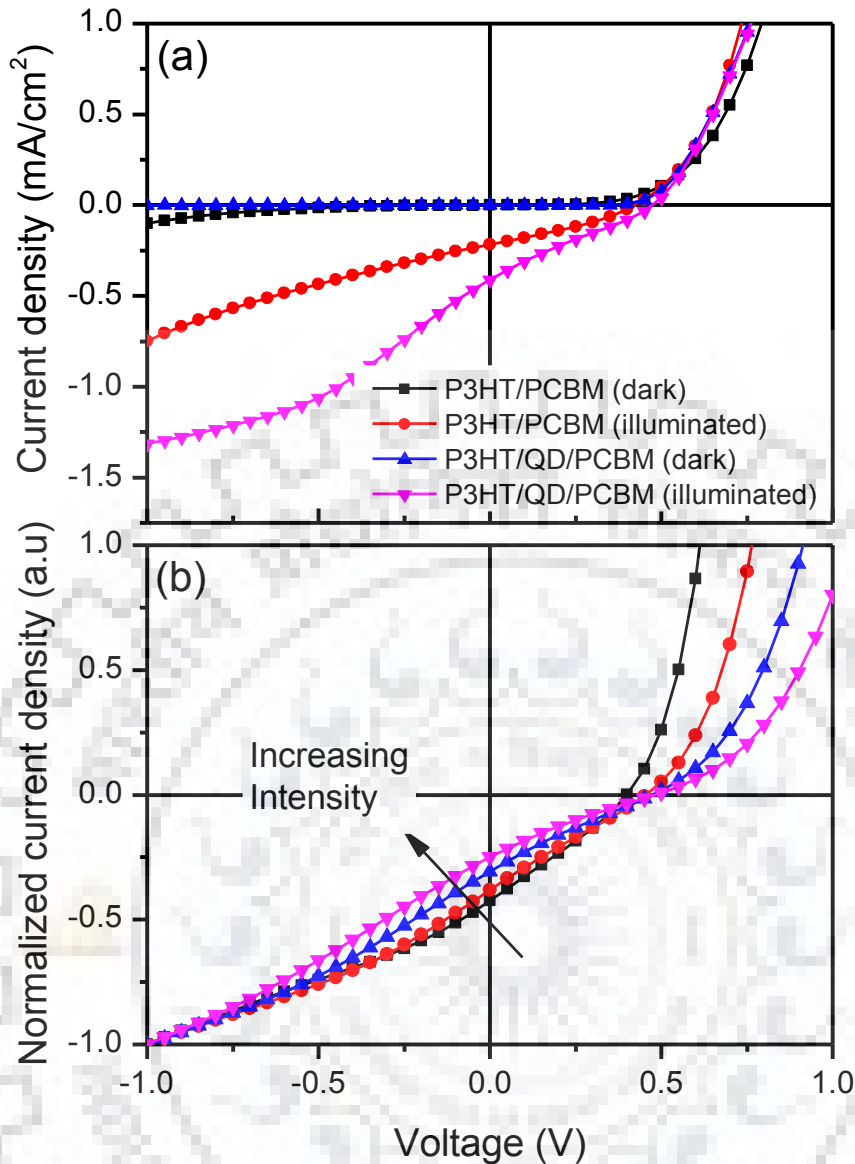
Figure 4.4 (a) Dark and illuminated J-V characteristics of P3HT/PCBM bilayer organic solar cell with and without QD interlayer, (b) normalized current density vs voltage characteristics with varying illumination intensity in the QD integrated solar cell.

In order to investigate the reason behind the s-shape J-V characteristics of QD integrated (QD Interlayer between conventional donor and acceptor layer) organic solar cells, the model is numerically analyzed with the variation of capture/emission time constant [135]. Charge injection/extraction rate depends upon structural/energetic disorders at the interface and electronic coupling between the used materials and the range can be varied from 10^3 s^{-1} to 10^{10} s^{-1} [136-137]. In the model, the capture/emission time constant (which is equal to the inverse of injection/extraction rate) was varied and found as a responsible factor for s-kink in the J-V characteristics. It was also observed that the degree of s-kink increased with increasing illumination intensity. So, it is concluded that the degree of s-kink is directly proportional to the

magnitude of accumulated photo carriers at the interface. The J-V characteristics plotted in Fig. 4.4 (b) were measured with increasing illumination intensity. The fill factor decreased with increasing illumination intensity in a similar way as we found in numerical analysis of the device [135].

Fill factor is directly related to the charge transport in the device. On addition of QDs in the device, the fill factor reduces with increase in illumination intensity as shown in Fig. 4.4 (b) which can be attributed to the increase in accumulated photo carriers in the device.

3.2. CdS-ZnS WQDs Solar Cell

The white light-emitting CdS-ZnS QDs were synthesized whose absorption and PL spectra are shown in the Fig.4.5. First absorption peak at approx. 430 nm corresponds to the bandgap of the QDs. The PL spectrum has a sharp peak at 445 nm along with emission in wide range between 500 nm to 800 nm which is due to band edges and trap state emission respectively [138].

Thus, short-wavelength spectrum mainly below 430 nm is absorbed in the QDs and is emitted in the longer wavelength so it may work as a down converter in photovoltaic devices. The down-converted photons belong to the absorption range of P3HT.
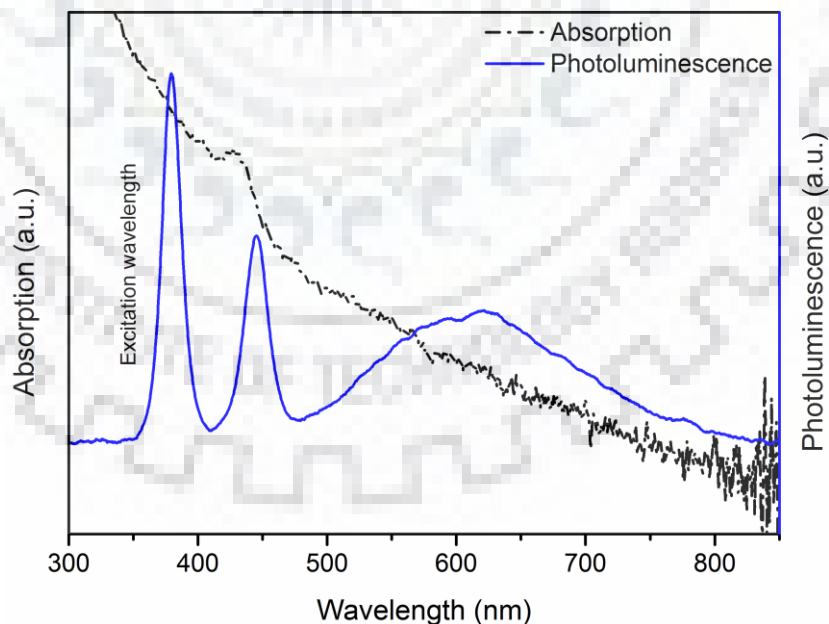
Figure 4.5 Absorption and PL spectra of CdS-ZnS QDs dispersed in chloroform.

These QDs were used in the P3HT-PCBM based solar cells and the behavior of the device was studied.

3.2.1. Bilayer Heterojunction Solar cell

The white light emission in the QDs is due to the emission from the trap states. Thus, trap states play active role in optical properties of the QDs and it may affect the charge transport in the device. The dark and illuminated J-V characteristics of the bilayer heterojunction solar cells with sandwiched QD layer at the donor-acceptor interface are plotted in Fig. 4.6. The dark characteristic shows that the knee voltage of the device is reduced to about 0.25 V which is approximately half of the knee voltage of conventional P3HT/PCBM bilayer heterojunction (dark characteristic in Fig. 4.4 (a)). The V_{OC} is much higher as compared to the knee voltage and degrades with time in an unusual manner which can be attributed to the effects of the presence of trap states at the QD's surface. The s-kink in the illuminated J-V characteristics does not appear which shows the improvement in charge transport consequently; fill factor of the device is improved but overall device performance is degraded.
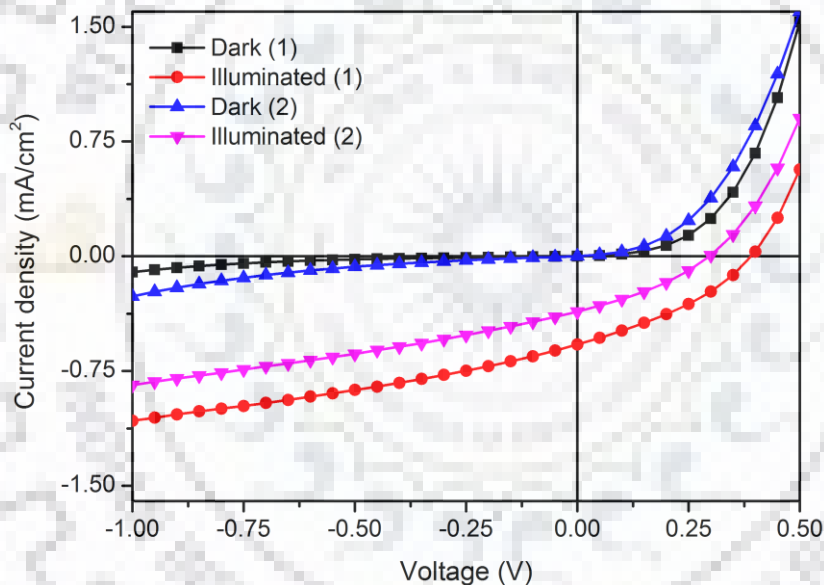
Figure 4.6 J-V characteristics of the bilayer heterojunction solar cell with sandwiched layer of WQDs between D-A layer under the dark and illuminated condition measured at two times of interval 5 min.

3.2.2. Bulk Heterojunction Solar Cell

Furthermore, the bulk heterojunction solar cell was fabricated by mixing of WQDs in 1:1 solution of P3HT and PCBM. The final solution was diluted in order to keep concentration same as before the addition of WQDs in P3HT:PCBM solution. Two devices were fabricated according to the procedure given in experimental details.

Optical absorption spectra of the bulk P3HT:PCBM with and without WQDs were recorded using USB 4000 spectrometer and plotted in Fig. 4.7. The addition of WQDs in the

device improved optical absorption in wavelength from 360 nm to 470 nm and wavelength more than 575 nm. The absorption spectra of the dispersed WQDs in chloroform was showed a single absorption peak as usual but absorption spectra of the thin film of bulk P3HT:PCBM heterojunction solar cell is affected on mixing with WQDs in the layer differently. This may be due to the incorporation of additional trap states.
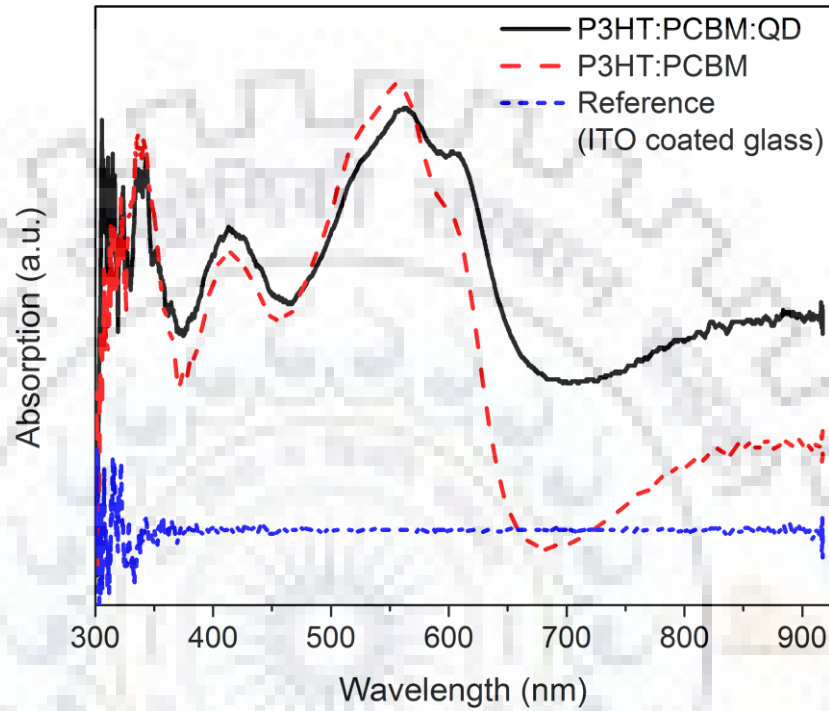
Figure 4.7 Optical absorption of P3HT:PCBM bulk heterojunction thin film with and without WQDs.

Electrical characteristics of the solar cell are shown in Fig. 4.8. The knee voltage of the bulk heterojunction diode is highly affected with the addition of WQDs in bulk heterojunction diode. Dark characteristics show that the knee voltage of BHJ diode is reduced; it is approximately half of the BHJ diode without WQDs. On illumination of the device with 1 sun intensity, the cell gives V_{OC} =0.4 V, J_{SC} =0.57 mA/cm^2, and FF ~ 34%. But, device with added WQDs shows degraded PCE along with other solar cell parameters. The V_{OC} in the WQD added device is much higher with respect to the knee voltage of that found previously in the bilayer solar cell.
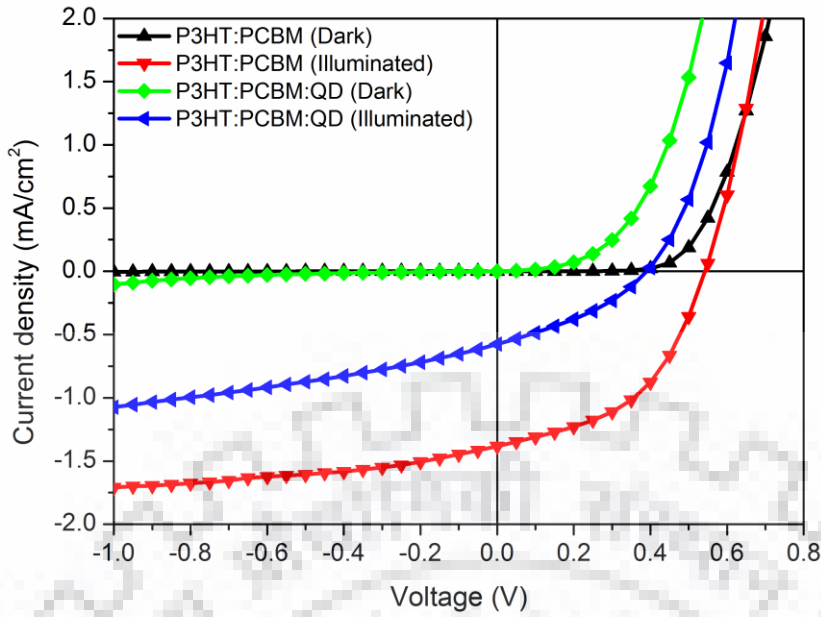
Figure 4.8 Dark and illuminate J-V characteristics of the P3HT:PCBM and P3HT:PCBM:WQD bulk heterojunction solar cells.

Thus, in the above discussion, it has been observed that solar cell performance can be improved by integrating the QDs in conventional organic solar cells. But, to achieve that, the synthesized QDs must be well controlled. Primarily the trap state distributions with respect to energy as well as spatial distribution must be controlled as the efficient charge transport is an essential requirement of a good device.

In summary, the CdSe-ZnS and CdS-ZnS core-shell QDs were fabricated and integrated into the photovoltaic devices. This results in enhancement in solar cell parameters, J_{SC} and V_{OC}, which is due to the enhancement in photon absorption and the reduction in series resistance attributed to improved charge transport in the device. A drastic change in fill factor with the appearance of s-kink in J-V characteristic is mainly due to low injection rate of photoelectrons in the QDs which results in accumulation of carriers at the interface, promotes the recombination of photo-carriers and degrades the shunt resistance. Improvement in fill factor (reduction in degree of s-kink) with illumination intensity indicates the concentration of accumulation of photo-carriers should be minimum for efficient photovoltaic devices. It can be achieved by minimizing the structural disorders in the vicinity of the donor-QD interface.

Chapter 5

S-shaped Current-Voltage Characteristics

1. Introduction

Currently, the field of organic solar cells is concentrated on the development of novel materials, interface engineering, and the addition of nano-elements for light management and/or improvement in conduction and recombination mechanisms in the devices [139-140]. Although the various efforts are leading us towards improved performance, sometimes they cause an undesirable s-kink in the fourth quadrant of current density-voltage characteristics which drastically reduces fill-factor and open-circuit voltage of the solar cell [132].

In order to reveal the origins of undesirable s-kink in J-V characteristics, researchers have fabricated various device structures, performed numerical simulations, and modeled equivalent circuits which intentionally produce s-kink and found that the imbalanced carrier mobility, poor extraction of the carriers at electrodes, injection/extraction barrier between electrodes and active material, etc. are the primary factors responsible for the s-shaped J-V characteristics [131, 133, 141-143]. The s-kink in J-V curve is mainly due to the unbalanced carrier extraction from the active region of the device. In this order, (1) the charge injection at the donor-acceptor (D-A) interface and (2) tunneling rate among the quantum dots play an important role in determining the J-V characteristic of the device.

1.1. Distribution of Trap State at Donor-Acceptor Interface

In the development of quantum dot organic solar cells, the carrier injection in the QDs is very sensitive to the change in morphology by thermal annealing, surface roughness at the interface and electronic coupling between the QDs and neighbor material [144-145]. Although there are no dangling bonds at the surface of a molecular crystal, the structural disorder at the D-A interface creates energetic disorder with a variance of several tenths of eV which is responsible for the generation of widely distributed trap sites in the forbidden energy gap. The trap states having trap energy up to few $k_B T$ eV and trap sites with trap energy more than 0.25

eV are known as shallow traps and deep traps respectively. The mobility of charge carriers in the bulk semiconductor varies several orders of magnitude depending on positions of traps and corresponding capture/emission time constants in the material [146]. The traps in the vicinity of interface and electronic coupling between the materials have jointly changed the scenario of the carrier injection between donor and acceptor layers.

1.2. Tunneling Coefficient among the Quantum Dots

The tunneling rate is also an essential constraint to determine the charge transport in the device. Tunneling rate basically depends on the tunneling coefficient and the carrier concentration gradient.

In the synthesis of colloidal QDs, long organic ligands such as oleic acid (OA), trioctylphosphine (TOP), and oleylamine, etc. are commonly used which allow low surface defect, controlled growth, and good stability in dispersed solvents. Such long organic ligands are electrically insulating and form a large potential barrier as well as the shell thickness. Consequently, it results in inefficient charge transport among the QDs and limits the applicability of QDs in the electronic devices. Although, high-temperature treatment of QDs is removed the ligands but carbon/organic residues are still on the surface of QDs and responsible for the poor electrical performance.

In the chapter, I have used our previously proposed QD organic solar cell model [128] and examine the effects of capture/emission time constant and tunneling coefficient which control carrier injection/extraction rate between QDs and neighbour material and tunneling rate among the QDs on the performance of solar cell and thoroughly analyzed the appearance of s-kink in J-V characteristics.

2. Theory and Model

The band diagram of the schematic device under the equilibrium condition is shown in Fig. 5.1(a). The whole process of electrical energy generation can be summarized as follows. The photons of sufficient energy get absorbed and generate excitons in the absorber layer. These excitons diffuse towards the D-A interface and dissociate into free carriers at the interface by transferring electrons to the acceptor and leaving holes in donor material [13]. A thin generation layer between poly (3-hexylthiophene) (P3HT) layer and QD layer with highest occupied molecular orbital equal to HOMO of donor and lowest unoccupied molecular orbital equal to LUMO of acceptor layer is assumed and free carriers are generated only in this layer. The free holes are moved towards the anode via hole transport layer and free electrons are first

injected into QDs and tunnel among several QD layers then reach the electron transport layer and are finally collected by the cathode. The detailed modeling of various processes is given in Ref. [128].

TABLE-5.1 Electrical parameters used in the model for transport (P3HT, BCP) layer and quantum dots

Parameters (symbol)	Transport layers	QD layers
SRH recombination lifetime	1.0 μs	1.2 μs
Dielectric constant	4.5 ε_0 F/cm	11.3 ε_0 F/cm
Tunneling coefficient	-	1.42×10^{10} /s (10^5-10^{10} /s)
Capture/emission time constant, τ	-	1 ms to100 ps (1 ns)
Bimolecular recombination coefficient	-	4.0×10^{-10} cm^3/s

2.1. Charge Transfer at Donor-Acceptor Interface

Charge hopping is one of the most common regimes for transport in organic semiconductors. The hopping mechanism is well described by Marcus [147]. The Marcus theory directly gives the probability of a transition from an initial state to final state but, for device application, electron transfer rate is more useful than the probability. So, if it is assumed that the distribution of final energy state has vibrational energy significantly lower than thermal energy and probability density is integrated over all possible values, the rate of electron transfer between initial and final state can be written as

$$k_{if} = \frac{2\pi}{\hbar}\left|\left\langle\psi_i\left|V\right|\psi_f\right\rangle\right|^2\left\{\frac{1}{\sqrt{4\pi\lambda k_B T}}\exp\left[\frac{-\left(\Delta G^0+\lambda\right)^2}{4\lambda k_B T}\right]\right\}$$ (1)

where, ΔG^0 is the change in Gibbs free energy, λ is reorganization energy and $\left|\left\langle\psi_i\left|V\right|\psi_f\right\rangle\right|$ is the electronic coupling between materials. The role of energetic disorder, electronic coupling, etc. on the charge transfer rate between radical sites are well studied by T. W. Kemper and the typical rate is found to be 10^7 s^{-1} whereas some sites have rate $\sim10^{10}$ s^{-1} [136].

Due to weak coupling within the molecules, the band like transport rarely occurs in organic semiconductors. The charge transport follows via multiple trapping de-trapping mechanisms, so deep traps drastically increase the emission time constant and degrade the charge transport [148]. Lifetime of the carrier in its free state depends on the concentration and nature of trap sites. A carefully prepared organic crystal can contain about 10^{15} cm^{-3} traps and

carrier spends about 10^{-7} s in the trapped state. The typical trapping time for a disordered semiconductor varies in the range of 10^{-5}-10^{-3} s [137].

Thus, there are two factors which control the injection rate of carriers at the D-A interface; first, electron transfer rate described by Marcus based on electronic coupling, reorganization energy and Gibbs free energy between the materials and second, the hopping rate in presence of deep traps in the vicinity of the D-A interface. I have taken time constants corresponding to the rate described by Marcus theory and rate controlled by deep traps. Thus, the overall time constant (capture/emission time constant) is determined by the combined effect of both phenomena and net injection rate is limited by the slower one. The parameter, capture/emission time constant represents mean-time that is required by an electron/hole to transfer from one site to another site at the QD and transport layers interfaces.

2.2. Tunneling Rate among Quantum Dots

Tunneling rate among the quantum dots mainly depends on the shell thickness and energy barrier between core and shell of that. The simplified tunneling coefficient can be written as [45]

$$T \approx 16 \left(\frac{E}{V_0} \right) \left(1 - \frac{E}{V_0} \right) exp\{-2k(2d_{Barrier})\}, \tag{2}$$

where, $k = \sqrt{\frac{2m}{\hbar^2}(V_0 - E)}$, E is the electron energy less than the energy barrier (V_0) between core and shell of the QD, and $d_{Barrier}$ is the thickness of potential barrier which is equal to the thickness of insulating shell around the quantum dot core.

The electrical properties of the quantum dot-based devices have a direct dependency on the tunneling rate among the QDs. In the QD based electronic devices, mobility is an essential property which is well studied with respect to the synthesis process, shape and size of QDs, ligand length, doping etc. In previous study, it is found that halide ions (Cl^-, Br^-, I^-, etc.), metal chalcogenide (MCC) capping ligands ($Sn_2S_6^{4-}$, $In_2Se_4^{2-}$, and $Cu_7S_4^-$), oxoanions (PO_4^{3-} and MoO_4^{2-}) etc, short inorganic ligands have excellent charge carrier mobilities and provide better electrical characteristics and high photovoltaic efficiencies as compared to organic ligands. S. M. Jung et al. [149] studied ligand-dependent electrical performance of QD thin-film transistors and found that the MCC ligands $Sn_2S_6^{4-}$, $Sn_2Se_6^{4-}$, and $In_2Se_6^{2-}$ on CdSe QDs cause large variation in the field-effect mobilities, the typical values are of 4.8, 12.0, and 44.2 cm^2/Vs respectively. The short ligands of length few tenths of nm could reduce the inter particle distance between QDs, compared to long ($\geq$1.0 nm) organic ligands. Further, on thermal

decomposition of MCC ligands, the interspacing among the QDs is reduced significantly consequently, reduced interspacing among the QDs significantly improves the tunneling coefficient consequently, the electric conductivity.

In addition, film morphology, roughness, non-homogeneous films are considerably affecting the potential distribution in the QD thin film. So, energy barrier between QDs no longer periodic and formed trap state and non-uniformity directly affect the tunneling coefficient among the QDs. Core size of the quantum dots determines the attempt frequency of electron and hole localized at the QD.

$$\nu = \frac{v_{th}}{2d_{Well}} \tag{3}$$

where v_{th} is the thermal velocity of electrons and d_{Well} is the width of the potential well i.e. diameter of the quantum dot core.

3. Results and Discussions

3.1. Effects of capture/emission time constant

In the schematics, the thicknesses of P3HT and bathocuproine layers are 55.0 nm and 60.0 nm respectively and 5 silicon QD layers are cascaded between them. Each QD layer has 4.0 nm diameter of silicon core and 0.5 nm thick SiO_2 shell around the core and the generation layer of thickness is 1.0 nm, thus total device thickness becomes 141.0 nm. Furthermore, to make device characteristic unaffected by low carrier mobility, imbalance mobility and nature of contacts, the transport layers are intentionally doped and electrode contacts are assumed to be ohmic because metal work functions are closer to the HOMO and LUMO of respective organic semiconductors [128], [111]. The tunneling probability of carriers among the QDs through the SiO_2 barrier is calculated by WKB approximation.

The tunneling coefficient is assumed to be same for electrons and holes. The behavior of the device can be observed by varying τ from few milliseconds to few hundreds of picoseconds in order to analyze the impact on J-V characteristic of the solar cell. And, various electrical parameters used in the model are listed in Table-5.1. The model device is illuminated with solar radiation of power 100 mW/cm^2.
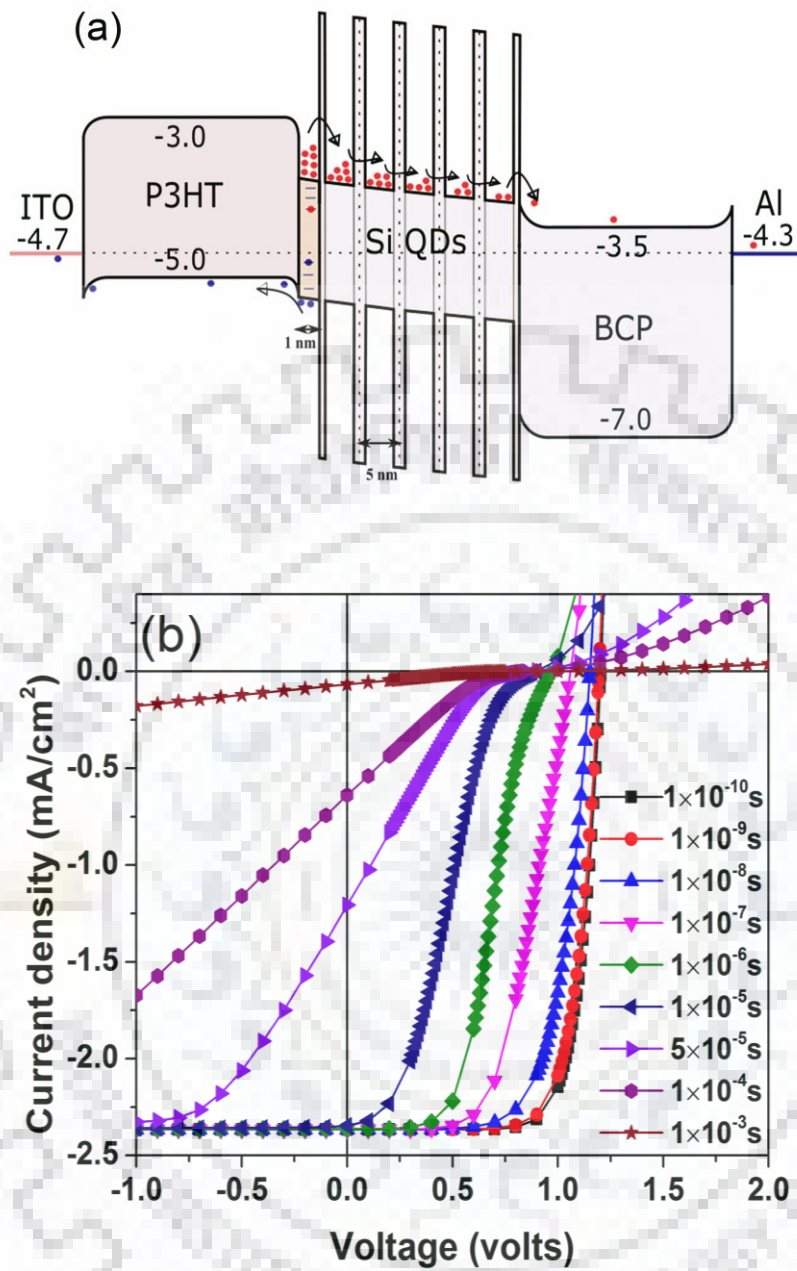
Figure 5.1 (a) Energy band diagram of Si quantum dot based organic solar cell in thermal equilibrium. (b) Current-voltage characteristic for various values of capture/ emission time constant under constant light illumination intensity of 100 mW/cm^2.

TABLE-5.2 Solar cell parameters extracted from J-V characteristic corresponding to capture/emission time constant.

τ (s)	V_{OC} (V)	J_{SC} (mA /cm^2)	FF (%)	R_S ($\Omega.cm^2$)	R_{Sh} ($\Omega.cm^2$)	J-V curve
1×10^{-10}	1.20	2.37	75.3	31.62	7.7×10^6	Exponential
1×10^{-9}	1.19	2.37	73.8	44.31	6.9×10^6	Exponential
1×10^{-8}	1.15	2.37	68.8	50.99	6.8×10^6	Exponential
1×10^{-7}	1.05	2.37	59.5	1.2×10^2	3.5×10^6	Exponential
1×10^{-6}	0.96	2.36	48.8	4.5×10^2	4.4×10^5	Semi-exp.
1×10^{-5}	**0.88**	**2.34**	**31.3**	**2.5×10^3**	**6.2×10^3**	**S-shaped**
5×10^{-5}	0.85	1.2	18.9	8.2×10^3	5.4×10^2	Semi-s-shape
1×10^{-4}	0.84	0.6	18.8	1.5×10^4	9.8×10^2	Semi-linear
1×10^{-3}	0.80	0.06	19.6	1.1×10^5	9.3×10^3	Linear

The J-V characteristics under illumination are plotted in Fig. 5.1(b) with varying capture/emission time constant from 1×10^{-3} s to 1×10^{-10} s and it is clearly shown that as the τ reduces from 1×10^{-3} s, the shape of J-V characteristic is improving. The improvement continues with an s-kink in J-V characteristic for a range (~ 10^{-6} s to 10^{-4} s) of τ. The J-V curves at $\tau=1\times10^{-9}$ s and 1×10^{-10} s are approximately overlapping hence no further effects/improvements are observed when τ is below 1 ns. The series resistance (R_S) for different J-V curves is continuously decreasing with τ and pinned to a minimum value while the shunt resistance (R_{Sh}) varies non-monotonically (see Table-5.2). For higher values of τ, the carrier transport is hindered, thus, the variation in J-V characteristics can be attributed to slow down in the injection rate of electrons at the QD-generation layer interface and increase in space charge concentration in the device. The solar cell parameters (V_{OC}, J_{SC}, and FF) are extracted from the J-V curves at various capture/emission time constants. For τ in the range of 1×10^{-8} s to 1×10^{-4} s, the V_{OC} and FF decrease exponentially, and J_{SC} remains almost constant upto $\tau=1\times10^{-5}$ s. Increasing value of τ causes the accumulation of photo-generated carriers which are more likely to recombine than being collected at the electrodes; degrading V_{OC}, J_{SC}, and FF. The carrier injection depends on the concentration gradient at the interface as well as τ. As τ increases, the emission process gets slower and carriers spend more time in the generation layer which causes an increase in the concentration gradient at the interface, and hence the behavior of J_{SC} is the result of the above two competitive processes. At lower values of τ, J_{SC} is limited by the

concentration gradient while at higher values of τ, it is limited by capture/emission time constant itself.
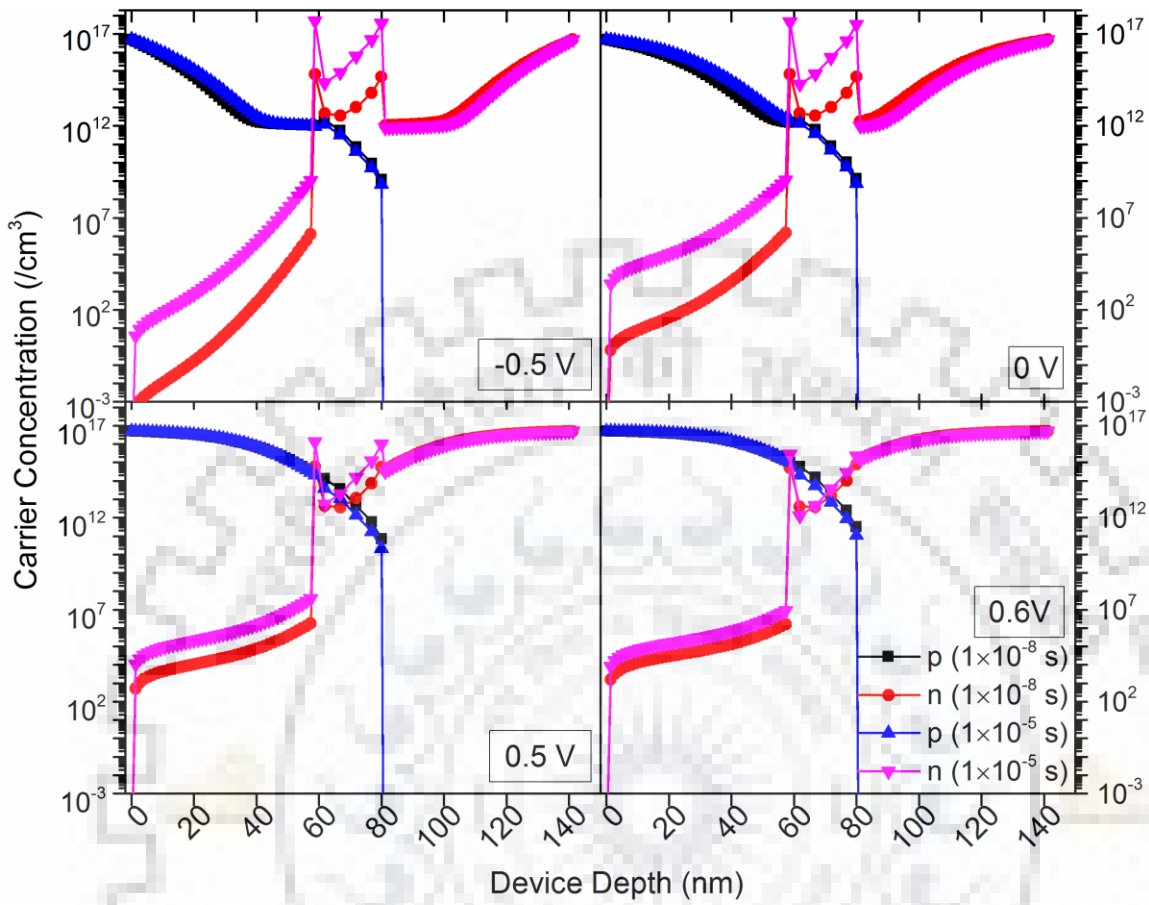
Figure 5.2 Carrier distributions in the device for $\tau=10^{-5}$ s and 10^{-8} s at various applied biases (-0.5, 0.0, 0.5, and 0.6 volts).

The charge distribution in the device for $\tau =1\times10^{-5}$ s (s-shaped) and 1×10^{-8} s (exponential) at various applied biases (-0.5, 0.0, 0.5, and 0.6 volts) are compared and plotted in Fig. 5.2. At negative applied bias, the carriers are efficiently extracted from the transport layers but the carrier concentration in QD layers and at its interfaces remains unaffected; this can be seen from the plots at -0.5 V and 0.0 V together. The constant current density for negative biases indicates that the current in the device depends on the concentration gradient at the interfaces for lower values of τ. Further increase in forward bias raises the carrier concentrations (see plots at 0.5 V and 0.6 V) in respective transport layers due to fast injection at QD interfaces for lower values of τ while at higher values of τ, the majority concentration increases due to increased injection from electrodes and minority concentration decreases due to poor injection of minority carriers from QD interfaces and increased recombination rate in transport layers. Also, at increasing forward bias, the electron concentration in QD layers is

decreasing and hole concentration is increasing because the recombination of photo-carrier (electrons) is increasing with increasing hole concentration in generation layer. Thus, a non-monotonic variation in accumulated charge concentration with applied voltage, mostly for higher values of τ, changes the scenario of carrier recombination in the device.
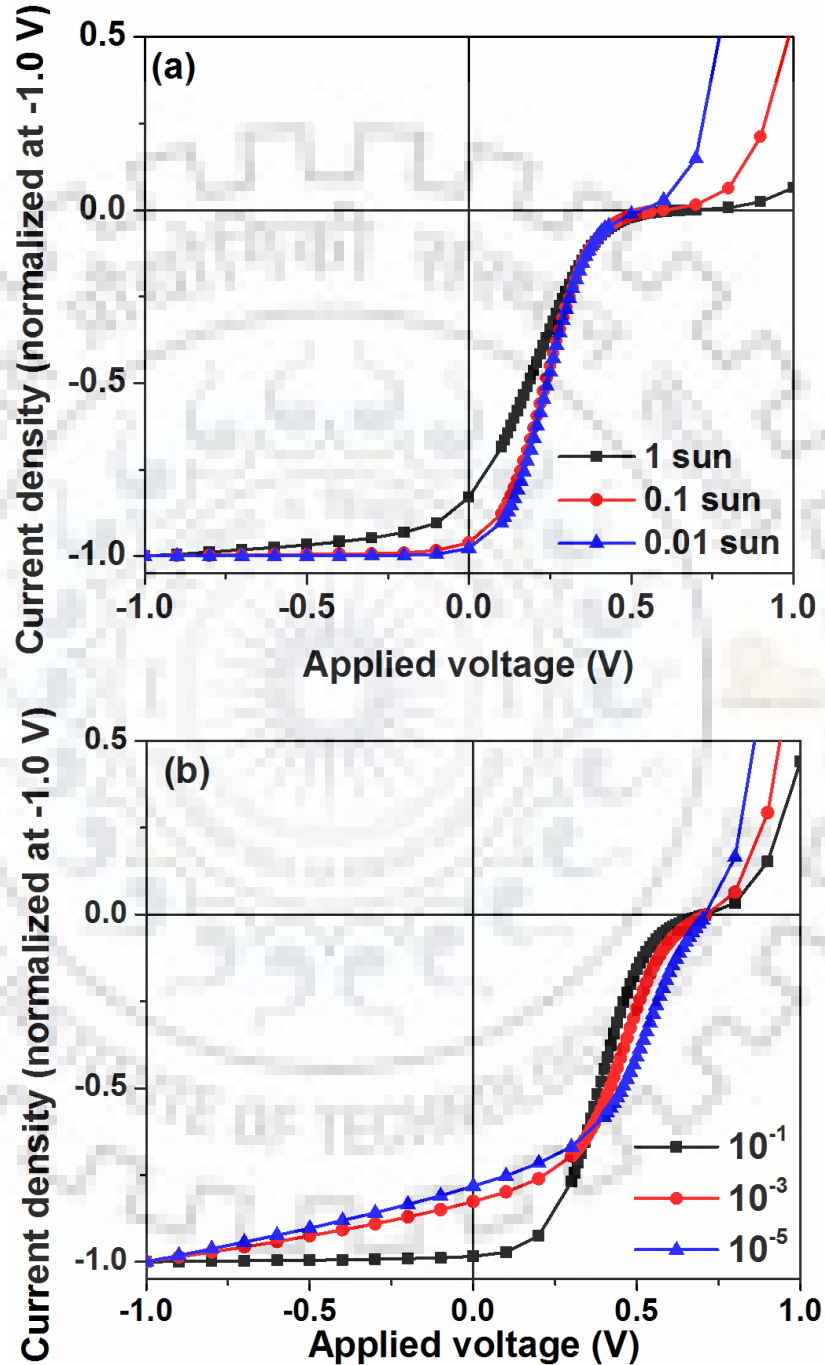
Figure 5.3 Normalized J-V characteristics where current density is normalized at -1.0 V applied bias under various (a) illumination intensities and (b) hole mobilities in HTL.

For efficient organic solar cells, the SRH recombination was proposed as a dominant mechanism at interfacial traps. The time delay between first and second carrier capture makes SRH recombination first order (monomolecular) process. The J-V characteristics, from short circuit condition to maximum power point and from maximum power point to open circuit condition are limited by monomolecular and bimolecular recombination respectively [150]. In Fig. 5.3, the normalized J-V characteristics (a) at varying illumination intensity and (b) at varying hole mobility of HTL are plotted for $\tau = 10^{-5}$ s. Figure 5.3 (a) shows that the monomolecular recombination rate is relatively high for higher illumination intensity, and overlapped curves near the V_{OC} indicates the bimolecular recombination rate is unaffected with illumination intensity. Here, excess holes are quickly swept from the active region of the device but the electrons require more time in being collected at the electrode. Therefore, to match the imbalance in holes and electrons collection, the mobility of holes in active layer has been reduced. The result shows that the monomolecular and bimolecular recombination rates are increasing with decreasing hole mobility and the degree of s-kink is also decreasing as hole mobility is decreasing. Thus, the quantity of accumulated photo-carrier and mismatched charge collection are the factors that control the degree of s-kink in J-V characteristic of QD solar cells.

3.2. Effect of Tunneling Rate

The tunneling rate among the quantum dots is found very sensitive to the ligand length, film defects, and its spatial and energetic distribution in the QD thin films. The range of tunneling coefficient is calculated with shell thickness for Si:SiO$_2$ core-shell QDs. A minor change of ~1 nm in order of ligand length in shell thickness causes large variation over several orders of magnitude. The overall tunneling rate coefficient can be varied from ~1×10^5 /s to ~1×10^{12} /s by considering combined effects of ligands, film defects, and its distribution. In the QDs at low tunneling rates, the charge carriers are more localized and significantly blocked the charge transport. Here, the effect of tunneling rate coefficient is analyzed on the J-V characteristics of QD solar cells.

In Fig. 5.4, the J-V characteristics are shown at varying tunneling rate coefficients. The J-V characteristics of the solar cell are continuously degrading with decreasing tunneling rate coefficient. For higher values of tunneling rate coefficient mainly above ~1×10^9 /s, the characteristics are overlapping and showing no significant effect on the characteristics but w lower than ~1×10^9 /s rapidly degrade the device performance. The reduction in tunneling rate coefficient causes localization of carriers on the quantum dots and promotes carrier recombination in quantum dots and its interfaces so device parameters are degraded

continuously with decreasing tunneling coefficient. The J-V characteristics show non-monotonic variation in the solar cell parameters that can be attributed to the competition between recombination rate and carrier concentration gradient in quantum dots. Carrier accumulation at interfaces as well as concentration gradient in the quantum dots is raised up due to blocking of carriers. That's why J_{SC} degrade quickly but at very low tunneling rates and appearance of S-shaped J-V characteristics is the result of an accumulation of charge carriers as explained previously.
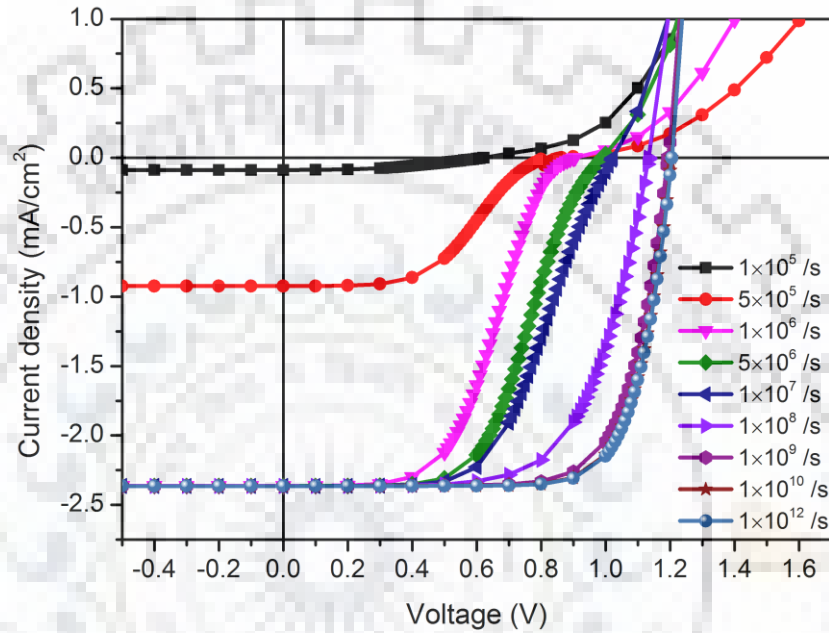
Fig. 5.4 Current-voltage characteristics of QD solar cell at various tunneling rate coefficients among the quantum dots.
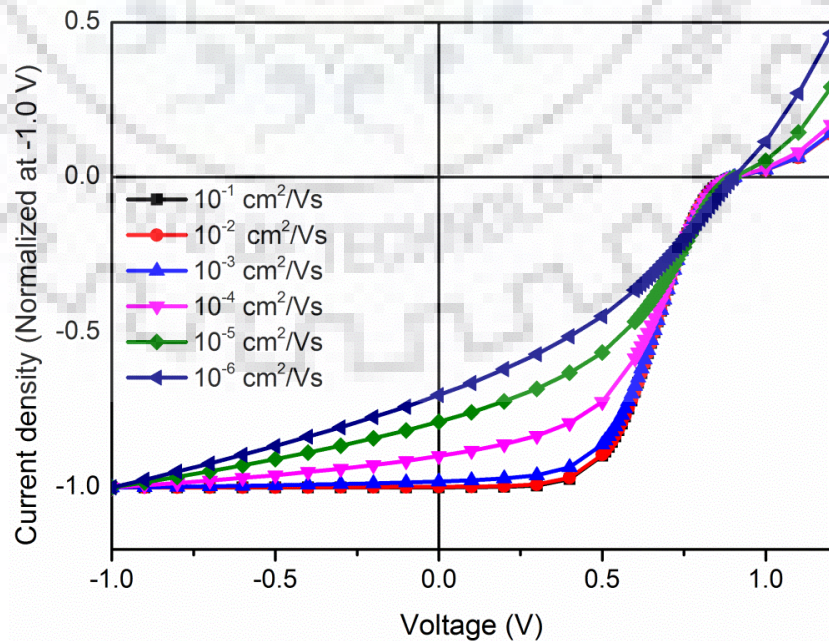
Figure 5.5 Normalized J-V characteristics of QD solar cell with decreasing hole mobility (from $0.1-10^{-6}$ cm^2/Vs) of hole transport (P3HT) layer. The current density is normalized at -1.0 V applied bias.

The normalized J-V characteristics at various hole mobilities in the hole transport layer are shown in Fig. 5.5. In order to balance the carrier extraction from the photovoltaic device, the hole mobility of HTL has been varied from 0.1 cm^2/Vs to 10^{-6} cm^2/Vs. Large variation in the normalized curves for lower voltages is showing the dominating monomolecular recombination in the active layer [150]. Degree of s-kink is reducing with decreasing hole mobility but improvement in FF is not observed which indicating that extraction of holes and electrons is balancing while raise up in bulk resistance of HLT restrict the improvement in FF.

Thus, capture/emission time constant and tunneling coefficient among the QDs are the prime factors that control J-V characteristic of the device. It is responsible for the change in shape of J-V curve from a diode (exponential) to a resistive (linear) curve via an s-shape characteristic. The series resistance increases and the shunt resistance decreases with increasing τ due to reduction in injection rate and accumulation of charge at the interface respectively. Thus, the deep traps (>0.3 eV) in the polymer at the vicinity (few $\mathring{A}$) of the interface for which τ is more than a micro-second cause s-shaped J-V characteristic and drastically reduce the fill factor as well as performance of the solar cells. Tunneling coefficient is mainly dependent on the height and width energy barrier and it can be easily tuned for efficient performance while capture/emission time constant is determined by energetic as well as spatial distribution of traps and vary over a wide range with interface roughness and morphology so it needs well-controlled fabrication handling. The varying illumination intensity and hole mobility in HTL reveals that quantity of accumulated photo-generated carriers and imbalance in charge extraction from active region of the device are the prime factors for the appearance of undesirable s-kink in J-V characteristic.

Chapter 6

Conclusions and Scope for Future Work

Firstly, I have modeled a bilayer heterojunction diode and analysis of simulation results leads us to model a piece-wise current-voltage characteristic model in bilayer organic diodes on the basis of the energy band diagram. The current-voltage characteristic is separated into three regimes of operation that are individually governed by the recombination, diffusion and bulk resistance limited charge transport processes and experimentally verified fabricated bilayer diodes. The model is able to predict the current-voltage characteristics of a diode on the basis of the energy band diagram and material parameters. Further, the charge transport in the quantum dot has been modeled and analysis of the effects of insertion of QD layer on the device performance has been carried out. The charge transport and recombination in the device are largely controlled by the bimolecular recombination coefficient which can be used to tune solar cell parameters, primarily, V_{OC}. Device performance can be optimized by some essential parameters namely: bimolecular recombination rate, capture/emission time constant, and tunneling coefficient among the quantum dots. Numerical analysis of the S-shaped J-V characteristics that appeared in the fabricated QDs based solar cells reveals the capture/emission time constant and tunneling coefficient are the prime factors that control J-V characteristic of the device. They are responsible for the change in the shape of J-V curve from a diode (exponential) to a resistive (linear) curve via an s-shape characteristic. The capture/emission time constant is strongly related to interfacial structural and energetic disorder and tunneling coefficient can be tuned on the basis of chosen materials (core and shell), shell thickness. Synthesis processes of quantum dots and fabrication conditions of the device have unintentionally varied these parameters. The poor capture/emission time constant (longer value) and tunneling coefficient (lower value) have degraded the device performance instead of improvement.

There are many aspects that remain untouched in the study of charge transport in quantum dots and integration in solar cells. Such as, the interface engineering can be performing with suitable bandgap and band alignment at D-A interface which intentionally block/allow charge carriers to transfer in a certain direction. The measured current in various devices with the above state of art can provide information about the dominant process of exciton dissociation. The buffer layer at the D-A interface can be replaced by inorganic thin

layer of high-k materials which may reduce the binding energy of exciton in the vicinity of the dissociating interface and enhance the performance.

Bibliography

1. L. Lu, T. Zheng, Q. Wu, A. M. Schneider, D. Zhao, and L. Yu, "Recent advances in bulk heterojunction polymer solar cells," *Chem. Rev.*, vol. 115, no. 23, pp. 12666–12731, 2015.

2. C. J. Brabec, S. Gowrisanker, J. J. M. Halls, D. Laird, S. Jia, and S. P. Williams, "Polymer-Fullerene bulk-heterojunction solar cells," *Adv. Mater.*, vol. 22, no. 34, pp. 3839–3856, 2010.

3. J. Nelson, "Polymer: Fullerene bulk heterojunction solar cells," *Mater. Today*, vol. 14, no. 10, pp. 462–470, 2011.

4. S. E. Shaheen, R. Radspinner, N. Peyghambarian, and G. E. Jabbour, "Fabrication of bulk heterojunction plastic solar cells by screen printing," *Appl. Phys. Lett.*, vol. 79, no. 18, pp. 2996–2998, 2001.

5. K. X. Steirer, J. J. Berry, M. O. Reese, M. F. A. M. van Hest, A. Miedaner, M. W. Liberatore, R. T. Collins, and D. S. Ginley, "Ultrasonically sprayed and inkjet printed thin film electrodes for organic solar cells," *Thin Solid Films*, vol. 517, no. 8, pp. 2781–2786, 2009.

6. W. Brütting, "*Physics of Organic Semiconductors*," Wiley-VCH Verlag GmbH & Co. KGaA, 2006.

7. J. L. Brédas, J. P. Calbert, D. A. da Silva Filho, J. Cornil, "Organic semiconductors: A theoretical characterization of the basic parameters governing charge transport," *Proceedings of the National Academy of Sciences*, vol. 99, no. 9, pp. 5804-5809, 2002.

8. G. Li, R. Zhu, and Y. Yang, "Polymer solar cells," *Nat. Photonics*, vol. 6, pp. 153–161, 2012.

9. Y. Liu, J. Zhao, Z. Li, C. Mu, W. Ma, H. Hu, K. Jiang, H. Lin, H. Ade, and H. Yan, "Aggregation and morphology control enables multiple cases of high-efficiency polymer solar cells," *Nat. Commun.*, vol. 5, p. 5293, 2014.

10. L. J. A. Koster, V. D. Mihailetchi, and P. W. M. Blom, "Ultimate efficiency of polymer/fullerene bulk heterojunction solar cells," *Appl. Phys. Lett.*, vol. 88, no. 9, p. 093511, 2006.

11. M. A. Green, K. Emery, Y. Hishikawa, W. Wart and E. D. Dunlop, "Progress in photovoltaics: research and applications," *Prog. Photovolt: Res. Appl.* vol. 23, pp. 1–9, 2015.

12. Y. Hsiao, H. Zang, L. Yu and Bin Hu, "Dielectric interface effects on surface charge accumulation and collection towards high-efficiency organic solar cells," *J. Appl. Phys.*, vol. 115, no. 15, pp. 154506, 2014.

13. T. Goh, J. S. Huang, B. Bartolome, M. Y. Sfeir, M. Vaisman, M. L. Leec, and A. D. Taylor, "Panchromatic polymer–polymer ternary solar cells enhanced by Forster resonance energy transfer and solvent vapor annealing," *J. Mater. Chem. A*, vol. 3, pp. 18611–18621, 2015.

14. W. L. Xu, B. Wu, F. Zheng, X. Y. Yang, H. D. Jin, F. Zhu, and X. T. Hao, "Förster resonance energy transfer and energy cascade in broadband photodetectors with ternary polymer bulk heterojunction," *J. Phys. Chem. C*, vol. 119, pp. 21913−21920, 2015.

15. V. Bharti, A. Sharma, V. Gupta, G. D. Sharma, and S. Chand, "Improved hole mobility and suppressed trap density in polymer-polymer dual donor based highly efficient organic solar cells," *Appl. Phys. Lett.* vol. 108, no. 7, p. 073505, 2016.

16. A. Tada, Y. Geng, Q. Wei, K. Hashimoto and K. Tajima, "Tailoring organic heterojunction interfaces in bilayer polymer photovoltaic devices," *Nat Mater*, vol. 10, pp. 450-455, 2011.

17. W. Ting, Y. C. Hsiao, M. Li, N. G. Kang, J. W. Mays, and B. Hu, "Dynamic coupling between electrode interface and donor/acceptor interface via charge dissociation in organic solar cells at device-operating condition," *J. Phys. Chem. C*, vol. 119, pp. 2727−2732, 2015.

18. P. A. Cox, M. S. Glaz, J. S. Harrison, S. R. Peurifoy, D. C. Coffey, and D. S. Ginger, "Imaging charge transfer state excitations in polymer/fullerene solar cells with time-resolved electrostatic force microscopy," *J. Phys. Chem. Lett.,* vol. 6, pp. 2852−2858, 2015.

19. F. Wang, Z. Chen, L. Xiao, B. Qu, and Q. Gong, "Enhancement of the power conversion efficiency by expanding the absorption spectrum with fluorescence layers," *Optics Express,* vol. 19, no. S3, pp. A361-A368, 2011.

20. M. Hiramoto, H. Fukusumi, and M. Yokoyama, "Organic solar cell based on multistep charge separation system," *Appl. Phys. Lett.,* vol. 61, no. 21, p. 2580, 1992.

21. M. Hallermann, and E. von Hauff "Correlation between charge transfer exciton recombination and photocurrent in polymer/fullerene solar cells," *Appl. Phys. Lett.,* vol. 97, no. 2, p. 023301, 2010.

22. K. Kenan, F. Z. Tepehan, G. G. Tepehan, "Growth of MPS-capped ZnS quantum dots in self-assembled thin films: Influence of heat treatment," *Superlattices and Microstructures*, vol. 88, pp. 527-535, 2015.

23. Y. Al-Douri, K. D. Verma, and D. Prakash, "Optical investigations of blue shift in ZnS quantum dots," *Superlattices and Microstructures*, vol. 88, pp. 662-667, 2015.

24. Y. Cheng, M. Zhang, G. Yao, L. Yang, J. Tao, Z. Gong, G. He, Z. Sun, "Band gap manipulation of cerium doping TiO_2 nanopowders by hydrothermal method," *Journal of Alloys and Compounds*, vol. 662, pp. 179–184, 2016.

25. Z. N. Kayani, A. Afzal, M. Z. Butt, I. Batool, S. Arshad, Y. Ali, S. Riaz, S. Naseem, "Structural, optical and magnetic properties of iron oxide nano-particles," *Materials Today: Proceedings*, vol. 2, no. 10B, pp. 5660–5663, 2015.

26. N. G. Imam, M. B. Mohamed, "Optical properties of diluted magnetic semiconductor Cu:ZnS quantum dots," *Superlattices and Microstructures*, vol. 73, pp. 203-213, 2014.

27. M. Hari, S. A. Joseph, S. Mathew, P. Radhakrishnan, and V. P. N. Nampoori, "Band-gap tuning and nonlinear optical characterization of $Ag:TiO_2$ nanocomposites," *J. Appl. Phys.*, vol. 112, no.7, pp. 074307, 2012.

28. B. Kumar, S. A. Campbell, and P. P. Ruden, "Modeling charge transport in quantum dot light emitting devices with NiO and ZnO transport layers and Si quantum dots," *J. Appl. Phys.*, vol. 114, no. 4, pp. 044507, 2013.

29. W. Vervisch, S. Biondo, G. Rivière, D. Duché, L. Escoubas, P. Torchio, J. J. Simon, and J. Le Rouzo, "Optical-electrical simulation of organic solar cells: excitonic modeling parameter influence parameter influence on electrical characteristics," *Appl. Phys. Lett.*, vol. 98, no. 2, p. 253306, 2011.

30. H. Fardi, "Numerical analysis of semiconductor P-N junctions using MATLAB," *JSRR*, vol. 6, no. 2, pp. 84-98, 2015.

31. S. Yin, W. Nie, A. D. Mohite, A. Saxena, D. L. Smith, and P. P. Ruden, "Current-voltage characteristics of organic heterostructure devices with insulating spacer layers," *Organic Electronics*, vol. 24, no. 26, 2015.

32. Mark S. Lundstrom, and Robert J. Schuelke, "Numerical analysis of hetero-structure semiconductor devices," *IEEE Trans. on Electron Devices*, vol. 30, no. 9, 1983.

33. M. Kurata, "*Numerical Analysis for Semiconductor Devices,*" Lexington, D.C. Heath and Company, Ch. 1-4, 1982.

34. M. S. Mock, "On the convergence of Gummel's numerical algorithm," *Solid State Electronics,* Vol. 15, pp. l-4, 1972.

35. H. K. Gummel, "A self-consistent iterative scheme for one-dimensional steady state transistor calculations," *IEEE Trans. Electron Devices,* vol. 11, p. 455, 1964.

36. A. DeMari, "An accurate numerical steady-state one-dimensional solution of the P-N junction," *Solid State Electron*., vol. 11, p. 33, 1968.

37. D. L. Scharfetter, H. K. Gummel, "Large-signal analysis of a silicon read diode oscillator," *IEEE Trans. on Electron Devices*, vol.16, no.1, 1969.

38. L. F. H. García, V. Cabrera-Arenas, L.M. Reséndiz-Mendoza, "On the convergence of the algorithm for simulating organic solar cells," *Computer Physics Communications,* vol. 196, pp. 372–379, 2015.

39. C. Falco, R. Sacco and M. Verri, "Analytical and numerical study of photocurrent transients in organic polymer solar cells," *Computer Methods in Applied Mechanics and Engineering,* vol. 199, pp. 1722–1732, 2010.

40. N. Agnihotri, "Computational studies of charge transfer in organic solar photovoltaic cells: A review," *Journal of Photochemistry and Photobiology C: Photochemistry Reviews*, vol. 18, pp. 18–31, 2014.

41. M. M. Chowdhury, M. K. Alam, "An analytical model for bulk heterojunction organic solar cells using a new empirical expression of space dependent photocarrier generation," *Solar Energy,* vol. 126, pp. 64–72, 2016.

42. D. Çakir, M. Bokdam, M. P. de Jong, M. Fahlman and G. Brocks, "Modeling charge transfer at organic donor-acceptor semiconductor interfaces," *Appl. Phys. Lett.,* vol. 100, no.20, p. 203302, 2012.

43. G. Sixto, A. L. Rogach, A. A. Lutich, D. Gross, A. Poeschl, A. S. Susha, I. Mora-Sero, and J. Bisquert, "Energy transfer versus charge separation in hybrid systems of semiconductor quantum dots and Ru-dyes as potential co-sensitizers co-sensitizers of TiO2-based solar cells," *J. Appl. Phys*., vol. 110, no.1, pp. 014314, 2011.

44. U. Wurfel, D. Neher, A. Spies, and Albrecht, "Impact of charge transport on current-voltage charecteristics and power-conversion efficiency of organic solar cells," *Nat. Commun.*, vol. 6, p. 6951, 2015.

45. D. J. Griffiths, "*Introduction to Quantum Mechanics,"* Prentice Hall International, USA, 2005.

46. J. Ramanujam, D. Shiri, and A. Verma, "silicon nanowire growth and properties: a review," *Materials Express*, vol. 1, no. 2, p. 105, 2011.

47. A. Sahu, A. Khare, D. D. Deng, and D. J. Norris, "Quantum confinement in silver selenide semiconductor nanocrystals†," *Chem. Commun.*, vol. 48, pp. 5458-5460, 2012.

48. B. Liu, A. Khare and E. S. Aydil, "Synthesis of single-crystalline anatase nanorods and nanoflakes on transparent conducting substrates†," *Chem. Commun.,* vol. 48, pp. 8565-8567, 2012.

49. T. R. Ravindran, A. K. Arora, B. Balamurugan, and B. R. Mehta, "In homogenous broadening in the photoluminescence spectrum of CdS nanoparticles," *Nanostructured Materials*, vol. 11, p. 603, 1999.

50. B. Balamurugan, S. K. Sharma, and B. R. Mehta, "Fabrication and characterization of $Cd_X Zn_{(1-X)} S$ semiconductor nanoparticles," *Nanostructured Materials*, vol. 12, p. 151, 1999.

51. C. R. Gorla, S. Liang, G. S. Tompa, W. E. Mayo, Y. Lu, "Silicon and germanium nanoparticle formation in an inductively coupled plasma reactor," *J. Vac. Sci. Technol. A.*, vol. 15, pp. 860-864, 1997.

52. X. Pi, R. Liptak, J. D. Nowak, N. Wells, C. Carter, S. Campbell, and U. Kortshagen, "Air-stable full-visible-spectrum emission from silicon nanocrystals synthesized by an all-gas-phase plasma approach," *Nanotechnology.*, vol. 19, no. 24, p. 245603, 2008.

53. M. Wolkin, J. Jorne, P. Fauchet, G. Allan, and C. Delerue., "Electronic states and luminescence in porous silicon quantum dots: the role of oxygen," *Phys. Rev. Lett.*, vol. 82, p. 197-200, 1999.

54. P. P. Ahonen, J. Joutsensaari, O. Richard, U. Tapper, D. P. Brown, J. K. Jokiniemi, E. I. Kauppinen, "Mobility size development and the crystallization path during aerosol decomposition synthesis of TiO2 particles," *J. Aerosol Sci.,* vol. 32, no. 5, pp. 615-630, 2001.

55. J. H. Kim, T. A. Germer, G. W. Mulholl, and, S. H. Ehrman, "Size-monodisperse metal nanoparticles via hydrogen-free spray pyrolysis," *Adv Mater.*, vol. 14, pp. 518-521, 2002.

56. C. Murray, D. Norris, and M. Bawendi, "Synthesis and characterization of nearly monodisperse CdE (E= sulfur, selenium, tellurium) semiconductor nanocrystallites," *J. Am. Chem. Soc.,* vol. 115, pp. 8706-8715, 1993.

57. J. Yun, W. Wang, S. M. Kim, T.-S. Bae, S. Lee, D. Kim, G.-H. Lee, H.-S. Lee, and M. Song, "Light trapping in bendable organic solar cells using silica nanoparticle arrays," *Energy Environ. Sci.*, vol. 8, no. 3, pp. 932–940, 2015.

58. N. Kalfagiannis, P. G. Karagiannidis, C. Pitsalidis, N. T. Panagiotopoulos, C. Gravalidis, S. Kassavetis, P. Patsalas, and S. Logothetidis, "Plasmonic silver nanoparticles for improved organic solar cells," *Sol. Energy Mater. Sol. Cells*, vol. 104, pp. 165–174, 2012.

59. S.-S. Kim, S.-I. Na, J. Jo, D.-Y. Kim, and Y.-C. Nah, "Plasmon enhanced performance of organic solar cells using electrodeposited Ag nanoparticles," *Appl. Phys. Lett.*, vol. 93, no. 7, p. 3307, 2008.

60. T. Sogabe, Q. Shen, and K. Yamaguchi, "Recent progress on quantum dot solar cells: a review," *J. Photon. Energy*, vol. 6, no. 4, p. 040901, 2016.

61. A. T. Mallajosyula, S. S. K. Iyer, and B. Mazhari, "Improving the efficiency of charge extraction limited P3HT: PCBM solar cells using SWNTs with metallic characteristics," *J. Appl. Phys.*, vol. 109, no. 12, p. 124908, 2011.

62. A. T. Mallajosyula, S. S. K. Iyer, and B. Mazhari, "Role of single walled carbon nanotubes in improving the efficiency of Poly-(3-hexylthiophene) based organic solar cells," *J. Appl. Phys.*, vol. 108, no. 9, p. 094902, 2010.

63. A. Khare, A. W Wills, B. D. Chernomordik, D. J. Norris, E. Aydil, "Towards quantum-dot solar cells from abundant nontoxic materials," *11AIChE - 2011 AIChE Annual Meeting, Conference Proceedings*, 2011.

64. U. Kortshagen, R. Anthony, R. Gresback, Z. Holman, R. Ligman, C-Yi Liu, L. Mangolini, and S. A. Campbell, "Plasma synthesis of group IV quantum dots for luminescence and photovoltaic applications*," *Pure Appl. Chem.*, vol. 80, no. 9, pp. 1901–1908, 2008.

65. K. Vandewal, "Interfacial charge transfer states in condensed phase systems," *Annu. Rev. Phys. Chem*, vol. 67, pp. 113-133, 2016.

66. M. Dandu, R. Biswas, S. Das, S. Kallatt, S. Chatterjee, M. Mahajan, V. Raghunathan, and K. Majumdar, "Strong single- and two-photon luminescence enhancement by non-radiative energy transfer across layered heterostructure," *ACS Nano*, DOI: 10.1021/acsnano.9b01553, 2019.

67. G. Gupta, S. Kallatt, and K. Majumdar, "Direct observation of giant binding energy modulation of exciton complexes in monolayer MoSe2," *Physical Review B (Rapid Communication)*, vol. 96, p. 081403(R), 2017.

68. D. Somvanshi, S. Kallatt, C. Venkatesh, S. Nair, G. Gupta, J. Anthony, D. Karmakar, and K. Majumdar, "Nature of carrier injection in metal/2D semiconductor interface and its implications to the limits of contact resistance," *Physical Review B*, vol. 96, p. 205423, 2017.

69. V. Dixit, H. F. Liu, and N. Xiang, "Study of thermal-anneal-induced rearrangement of N-bonding configurations in GaInNAs/GaAs quantum well," *Advanced Materials Research*, vol. 31, pp. 209-211, 2007.

70. H. F. Liu, V. Dixit, and N. Xiang, "Effect of indium segregation on optical and structural properties of GaInNAs/GaAs quantum wells at emission wavelength of 1.3μm," *J. Appl. Phys.*, vol. 100, no. 8, p. 083518, 2006.

71. M. Katiyar, "Hydrogenated amorphous silicon thin films for photovoltaic technology: optical probes of growth kinetics," in Research Reports of the Link Energy Fellows, vol.8, *University of Rochester Press*, pp. 79-95, 1993.

72. M. Katiyar and A. H. Kitai, "Effect of organized doping on concentration quenching in ZnS:Mn," *J. Lumin.*, vol. 52, pp. 309-312, 1992.

73. M. D. Bhise, M. Katiyar, and A. H. Kitai, "Effect of Mn concentration on the cathodo- and photoluminescence of ZnS:Mn," *J. Appl. Phys.*, vol. 67, no. 3, pp. 1492-1498, 1990.

74. C. M. Chuang, P. R. Brown, V. Bulović, and M. G. Bawendi, "Improved performance and stability in quantum dot solar cells through band alignment engineering," *Nature Materials*, vol. 13, pp. 796–801, 2014.

75. S. Gustavsson, R. Leturcq, B. Simovič, R. Schleser, T. Ihn, P. Studerus, K. Ensslin, D. C. Driscoll, and A. C. Gossard, "Counting statistics of single electron transport in a quantum dot," *Phys. Rev. Lett.*, vol. 96, no. 7, pp. 6605, 2006.

76. D. Weinmann, W. Häusler, and B. Kramer, "Spin blockades in linear and nonlinear transport through quantum dots dietmar," *Phys. Rev. Lett.*, vol. 74, no. 6, pp. 984–987, 1995.

77. A. Verma, A. K. Buin, and M. P. Anantram, "High-field hole transport in silicon nanowires," *J. of Appl. Phys.*, vol. 106, p. 113713, 2009.

78. M. Z.Kauser, A. Verma, and P. P. Ruden, "Low and high field transport for semiconducting carbon nanotubes," *Physica E*, vol. 34, p. 666, 2006.

79. V. Dokania, A. Islam, V. Dixit, and S. P. Tiwari, "Analytical modeling of wrap-gate carbon nanotube FET with parasitic capacitances and density of states, *IEEE Trans. Electron Devices*, vol. 63, no. 8, pp. 3314–3319, 2016.

80. B. Geffroy, P. Le Roy, and C. Prat, "Organic light-emitting diode (OLED) technology: Materials, devices and display technologies," *Polym. Int.*, vol. 55, no. 6, pp. 572–582, 2006.

81. V. C. Bender, T. B. Marchesan, and J. M. Alonso, "Solid-state lighting: a concise review of the state of the art on LED and OLED modeling," *IEEE Ind. Electron. Mag.*, vol. 9, no. 2, pp. 6–16, 2015.

82. S. R. Forrest and M. E. Thompson, "Introduction: Organic electronics and optoelectronics," *Chem. Rev.*, vol. 107, no. 4, pp. 923–925, 2007.

83. P. P. Kumavat, P. Sonar, and D. S. Dalal, "An overview on basics of organic and dye sensitized solar cells, their mechanism and recent improvements," *Renew. Sustain. Energy Rev.*, vol. 78, pp. 1262–1287, 2017.

84. P. López Varo, J. A. Jiménez Tejada, J. A. López Villanueva, J. E. Carceller, and M. J. Deen, "Modeling the transition from ohmic to space charge limited current in organic semiconductors," *Org. Electron. physics, Mater. Appl.*, vol. 13, no. 9, pp. 1700–1709, 2012.

85. P. Kumar, S. C. Jain, V. Kumar, S. Chand, and R. P. Tandon, "A model for the J-V characteristics of P3HT:PCBM solar cells," *J. Appl. Phys.*, vol. 105, no. 10, p. 104507, 2009.

86. M. L. Inche Ibrahim, Z. Ahmad, and K. Sulaiman, "Analytical expression for the current-voltage characteristics of organic bulk heterojunction solar cells," *AIP Adv.*, vol. 5, no. 2, p. 27115, 2015.

87. P. K. Manda, S. Ramaswamy, and S. Dutta, "Extraction of the built-in potential for organic solar cells from current-voltage characteristics," *IEEE Trans. Electron Devices*, vol. 65, no. 1, pp. 184–190, 2018.

88. P. De Bruyn, A. H. P. Van Rest, G. A. H. Wetzelaer, D. M. De Leeuw, and P. W. M. Blom, "Diffusion-limited current in organic metal-insulator-metal diodes," *Phys. Rev. Lett.*, vol. 111, no. 18, p. 186801, 2013.

89. M. Mingebach, C. Deibel, and V. Dyakonov, "Built-in potential and validity of the Mott-Schottky analysis in organic bulk heterojunction solar cells," *Phys. Rev. B - Condens. Matter Mater. Phys.*, vol. 84, no. 15, p. 153201, 2011.

90. E. Tutiš, D. Berner, and L. Zuppiroli, "Internal electric field and charge distribution in multilayer organic light-emitting diodes," *J. Appl. Phys.*, vol. 93, no. 8, pp. 4594–4602, 2003.

91. J. H. Lee, J. H. Jeong, C. H. Suh, Y. K. Kim, N. G. Park, and Y. S. Kim, "Numerical analysis of OLED using the hetero electrode," *Curr. Appl. Phys.*, vol. 6, no. 4, pp. 654–657, 2006.

92. L. Zhang, L. Wang, W. J. Wu, and M. Chan, "Modeling current-voltage characteristics of bilayer organic light-emitting diodes," *IEEE Trans. Electron Devices*, vol. 66, no. 1, pp. 139–145, 2018.

93. G. Malliaras, J. Salem, P. Brock, and C. Scott, "Electrical characteristics and efficiency of single-layer organic light-emitting diodes," *Phys. Rev. B - Condens. Matter Mater. Phys.*, vol. 58, no. 20, pp. R13411–R13414, 1998.

94. M. S. Tyagi, "*Introduction to Semiconductor Materials and Devices,*" 1st ed. New Delhi: Wiley India, 2012.

95. S. M. Sze, "*Physics of Semiconductor Devices Physics of Semiconductor Devices,*" 3rd ed. New Delhi: Wiley India, 2008.

96. L. B. Schein, A. Peled, and D. Glatz, "The electric field dependence of the mobility in molecularly doped polymers," *J. Appl. Phys.*, vol. 66, no. 2, pp. 686–692, 1989.

97. A. Ioannidis, E. Forsythe, Y. Gao, M. W. Wu, and E. M. Conwell, "Current-voltage characteristic of organic light emitting diodes," *Appl. Phys. Lett.*, vol. 72, no. 23, pp. 3038–3040, 1998.

98. G. Lakhwani, A. Rao, and R. H. Friend, "Bimolecular recombination in organic photovoltaics," *Annu. Rev. Phys. Chem.*, vol. 65, no. 1, pp. 557–581, 2014.

99. B. Perucco, N. A. Reinke, D. Rezzonico, E. Knapp, S. Harkema, and B. Ruhstaller, "On the exciton profile in OLEDs-seamless optical and electrical modeling," *Org. Electron. physics, Mater. Appl.*, vol. 13, no. 10, pp. 1827–1835, 2012.

100. M. Sharma, A. N. Bhatt, and B. Kumar, "Study of variation in thickness of poly(n-vinylcarbazole) [PVK] thin films in different solvents for static dispense spin coating method," *2nd International Conference on Electronics, Materials Engineering & Nano-Technology (IEMENTech)*, 2018, no. 1978, pp. 1–3.

101. A. L. Ayzner, C. J. Tassone, S. H. Tolbert, and B. J. Schwartz, "Reappraising the need for bulk heterojunctions in polymer−fullerene photovoltaics: the role of carrier transport in all-solution-processed P3HT/PCBM bilayer solar cells," *J. Phys. Chem. C*, vol. 113, no. 46, pp. 20050–20060, 2009.

102. P. O. Anikeeva, J. E. Halpert, M. G. Bawendi, and V. Bulović, "Quantum dot light-emitting devices with electroluminescence tunable over the entire visible spectrum," *Nano Lett.*, vol. 9, no. 7, pp. 2532–2536, 2009.

103. Y. Shirasaki, G. J. Supran, M. G. Bawendi, and V. Bulović, "Emergence of colloidal quantum-dot light-emitting technologies," *Nat. Photonics*, vol. 7, no. 1, pp. 13–23, 2012.

104. S. Huang and G. Conibeer, "Sputter-grown Si quantum dot nanostructures for tandem solar cells," *J. Phys. D. Appl. Phys.*, vol. 46, no. 2, p. 4003, 2013.

105. B. Ghosh, and N. Shirahata, "Colloidal silicon quantum dots: synthesis and luminescence tuning from the near-UV to the near-IR range," *Sci. Technol. Adv. Mater.*, vol. 15, no. 1, p. 14207, 2014.

106. Y. Firdaus, E. Vandenplas, A. Khetubol, D. Cheyns, R. Gehlhaar, and M. Van der Auweraer, "Charge transport and recombination in P3HT:PbS solar," *J. Appl. Phys.*, vol. 117, no. 9, p. 5503, 2015.

107. C. Liu, K. Chang, W. Guo, H. Li, L. Shen, W. Chen, and D. Yan, "Improving charge transport property and energy transfer with carbon quantum dots in inverted polymer solar cells," *Appl. Phys. Lett.*, vol. 105, no. 7, p. 3306, 2014.

108. J. Lee, S. Park, Y. Lee, H. Kim, D. Shin, J. Jeong, K. Jeong, S. W. Cho, H. Lee, and Y. Yi, "Electron transport mechanism of bathocuproine exciton blocking layer in organic photovoltaics," *Phys. Chem. Chem. Phys.*, vol. 18, no. 7, pp. 5444–5452, 2016.

109. M. Hiramoto, M. Kubo, Y. Shinmura, N. Ishiyama, T. Kaji, K. Sakai, T. Ohno, and M. Izaki, "Bandgap science for organic solar cells," *Electronics*, vol. 3, no. 2, pp. 351–380, 2014.

110. J. Cuiffi, T. Benanti, W. J. Nam, and S. Fonash, "Modeling of bulk and bilayer organic heterojunction solar cells," *Appl. Phys. Lett.*, vol. 96, no. 14, p. 3307, 2010.

111. V. A. Trukhanov, V. V. Bruevich, and D. Y. Paraschuk, "Effect of doping on performance of organic solar cells," *Phys. Rev. B*, vol. 84, no. 20, p. 5318, 2011.

112. D. Das and A. Samanta, "Size effect on electronic transport in nC–Si/SiOx core/shell quantum dots," *Mater. Res. Bull.*, vol. 47, no. 11, pp. 3625–3629, 2012.

113. R. L. Anderson, "Experiments on Ge-GaAs heterojunctions," *Solid-State Electron.*, vol. 5, pp. 341–351, 1962.

114. K. Yang, J. R. East, and G. I. Haddad, "Numerical modeling of abrupt heterojunctions using a thermionic-field emission boundary condition," *Solid State Electron.*, vol. 36, no. 3, pp. 321–330, 1993.

115. B. Lüssem, M. Riede, and K. Leo, B. Lüssem, M. Riede, and K. Leo, "Doping of organic semiconductors," *Phys. Status Solidi A*, vol. 210, no. 1, pp. 9-43, 2013.

116. K. Tremel, and S. Ludwigs, "Morphology of P3HT in thin films in relation to optical and electrical properties" *Adv. Polym. Sci.*, vol. 265, pp. 39-82, 2014.

117. H. Sirringhaus, N. Tessler, and R. H. Friend, "Integrated optoelectronic devices based on conjugated polymers," *Science*, vol. 280, no. 12, pp. 1741-1744, 1998.

118. D. Das and A. Samanta, "Quantum size effects on the optical properties of nc-Si QDs embedded in an a-SiOx matrix synthesized by spontaneous plasma processing," *Phys. Chem. Chem. Phys.*, vol. 17, no. 7, pp. 5063–5071, 2015.

119. N. A. Sobolev, A. M. Emel'yanov, E. I. Shek, and V. I. Vdovin, "Extended structural defects and their influence on the electroluminescence in efficient Si light-emitting diodes," *Phys. B Condens. Matter*, vol. 340, pp. 1031–1035, 2003.

120. Y. S. Cho, and R. R. Franklin, "Conducting polymer material characterization using high frequency planar transmission line measurement," *Trans. Electr. Electron. Mater.*, vol. 13, no. 5, pp. 237–240, 2012

121. G. Juška, M. Viliunas, K. Arlauskas, and J. Kočka, "Space-charge-limited photocurrent transients: The influence of bimolecular recombination," *Phys. Rev. B*, vol. 51, no. 23, pp. 16668–16676, 1995.

122. A. Pivrikas, G. Juška, A. J. Mozer, M. Scharber, K. Arlauskas, N. S. Sariciftci, H. Stubb, and R. Österbacka, "Bimolecular recombination coefficient as a sensitive testing parameter for low-mobility solar-cell materials," *Phys. Rev. Lett.*, vol. 94, no. 17, pp. 1–4, 2005.

123. M. A. Stevens and A. C. Arango, "Open-circuit voltage exceeding the outermost HOMO-LUMO offset in cascade organic solar cells," *Org. Electron. physics, Mater. Appl.*, vol. 37, pp. 80–84, 2016.

124. D. Yu, R. W. Liptak, G. Aggarwal, A.-J. Cheng, S. A. Campbell, "Tunneling conduction in dense silicon quantum dot/poly(methyl methacrylate) composites," *Thin Solid Films*, vol. 527, pp. 261–266, 2013.

125. A. Melianas, V. Pranculis, D. Spoltore, J. Benduhn, O. Inganäs, V. Gulbinas, K. Vandewal M. Kemerink, "Charge Transport in Pure and Mixed Phases in Organic Solar Cells," *Adv. Energy Mater.*, vol. 7, no. 20, p. 1700888, 2017.

126. A. T. Mallajosyula, S. S. K. Iyer, and B. Mazhari, "Charge Transport in Polythiophene:Fullerene:Nanotube Bulk Heterojunction Photovoltaic Devices Investigated by Impedance Spectroscopy, *C. Appl. Phys.*, vol. 13, no. 4, pp. 677-683, 2013.

127. A. T. Mallajosyula, S. S. K. Iyer, and B. Mazhari, "Capacitance-Voltage characteristics of P3HT:PCBM bulk heterojunction solar cells with ohmic contacts and the impact of single walled carbon nanotubes on them," *Org. Electronics*, vol. 13, no. 7, 2012.

128. U. K. Verma and B. Kumar, "Charge transport in quantum dot organic solar cells with Si quantum dots sandwiched between poly (3-hexylthiophene) (P3HT) absorber and bathocuproine (BCP) transport layers," *J. Appl. Phys.*, vol. 122, p. 153104, 2017.

129. Sherafatipour, J. Benduhn, B. R. Patil, M. Ahmadpour, D. Spoltore, H.-Günter Rubahn, K. Vandewal, and M. Madsen, "Degradation pathways in standard and inverted DBP-C70 based organic solar cells," *Scientific Reports*, vol. 9, no. 4024, 2019

130. S. N. Sharma, U. Kumar, T. Vats, M. Arora, V. N. Singh, B. R. Mehta, K. Jain, R. Kakkar, and A. K. Narula, "Hybrid organic-inorganic (MEH-PPV/P$_3$HT: CdSe) nanocomposites: linking film morphology to photostability," *The European Physical Journal Applied Physics*, vol. 50, no. 2, p. 20602, 2010

131. W. Tress, A. Petrich, M. Hummert, M. Hein, K. Leo, and M. Riede, "Imbalanced mobilities causing S-shaped IV curves in planar heterojunction organic solar cells," *Appl. Phys. Lett.,* vol. 98, p. 063301, 2011.

132. M. Zhang, H. Wang, and C. W. Tang, "Hole-transport limited S-shaped I-V curves in planar heterojunction organic photovoltaic cells," *Appl. Phys. Lett.,* vol. 99, no. 21, p. 213506, 2011.

133. B. Romero, G. del Pozo, B. Arredondo, D. Martin-Martin, M. Gordoa, A. Pickering, A. Perez-Rodriguez, E. Barrena, and F. J. Garcia-Sanchez, "S-Shaped I-V characteristics of organic solar cells: Solving Mazhari's lumped-parameter equivalent circuit model," *IEEE Trans. Electron Devices*, vol. 64, no. 11, pp. 4622–4627, 2017.

134. J. Jasieniak, M. Califano, and S. E. Watkins, "Size-dependent valence and conduction band-edge energies of semiconductor nanocrystals," *ACS Nano,* vol. 5, pp. 5888-5902, 2011.

135. U. K. Verma, A. N. Bhatt and B. Kumar, "Impact of capture/emission time constant at donor–acceptor interface on current–voltage characteristics of hybrid organic/inorganic quantum dot solar cells," *IEEE Electron Device Letters,* vol. 39, pp. 1588-1591, 2018.

136. T. W. Kemper, R. E. Larsen, and T. Gennett, "Density of states and the role of energetic disorder in charge transport in an organic radical polymer in the solid state," *J. Phys. Chem. C,* vol. 119, pp. 21369−21375, 2015.

137. D. C. Hoesterey and G. M. Letson, "The trapping of photocarriers in anthracene by anthraquinone, anthrone and naphthacene*," *J. Phys. Chem. Solids,* vol. 24, pp. 1609-1615, 1963.

138. A. N. Bhatt, U. K. Verma, and B. Kumar, "Temporal evolution of white light emitting CdS core and Cd$_{1-x}$Zn$_x$S graded shell quantum dots fabricated using single step non-injection technique," *Optical materials*, vol. 92, pp. 143-149, 2019.

139. M. Graetzel, R. A. J. Janssen, D. B. Mitzi, and E. H. Sargent, "Materials interface engineering for solution-processed photovoltaics," *Nature*, vol. 488, no. 7411, pp. 304–312, 2012.

140. N. Ali, A. Hussain, R. Ahmed, M. K. Wang, C. Zhao, B. U. Haq, and Y. Q. Fu, "Advances in nanostructured thin film materials for solar cell applications," *Renew. Sustain. Energy Rev.*, vol. 59, pp. 726–737, 2016.

141. J. C. Wang, X. C. Ren, S. Q. Shi, C. W. Leung, and P. K. L. Chan, "Charge accumulation induced S-shape J-V curves in bilayer heterojunction organic solar cells," *Org. Electronics*, vol. 12, no. 6, pp. 880–885, 2011.

142. W. Tress, and O. Inganäs, "Solar energy materials & solar cells simple experimental test to distinguish extraction and injection barriers at the electrodes of (organic) solar cells with S-shaped current–voltage characteristics," *Sol. Energy Mater. Sol. Cells*, vol. 117, pp. 599–603, 2013.

143. A. Kumar, S. Sista, and Y. Yang, "Dipole induced anomalous S-shape I-V curves in polymer solar cells," *J. Appl. Phys.*, vol. 105, no. 9, p. 94512, 2009.

144. Y. H. Huh, B. Park, and I. Hwang, "Investigating the origin of S-shaped photocurrent-voltage characteristics of polymer : fullerene bulk-heterojunction organic solar cells," *J. Appl. Phys.*, vol. 115, no. 12, p. 124504, 2014.

145. S. V. Novikov and G. G. Malliaras, "Roughness-induced energetic disorder at the metal/organic interface," *Phys. Rev. B*, vol. 73, no. 3, p. 033302, 2006.

146. C. Li, L. Duan, H. Li, and Y. Qiu, "Universal trap effect in carrier transport of disordered organic semiconductors: Transition from shallow trapping to deep trapping," *J. Phys. Chem. C*, vol. 118, no. 20, pp. 10651–10660, 2014.

147. R. A. Marcus and N. Sutin, "Electron transfers in chemistry and biology," *BBA Rev. Bioenerg.*, vol. 811, no. 3, pp. 265–322, 1985.

148. X. Lu, K. Yu, H. Jiang, A. Zhang, and K. M. Lau, "Study of interface Traps in AlGaN/GaN MISHEMTs Using LPCVD SiNx as Gate Dielectric," *IEEE Trans. Electron Devices*, vol. 64, no. 3, pp. 824-831, 2017.

149. S. M. Jung, H. L. Kang, J. K. Won, J. Kim, C. Hwang, K. Ahn, I. Chung, B.-K. Ju, M.-G. Kim, and S. K. Park, "High-performance quantum dot thin-film transistors with environmentally benign surface functionalization and robust defect passivation," *ACS Appl. Mater. Interfaces*, vol. 10, pp. 3739−3749, 2018.

150. S. R. Cowan, A. Roy, and A. J. Heeger, "Recombination in polymer-fullerene bulk heterojunction solar cells," *Phys. Rev. B*, vol. 82, no. 24, p. 245207, 2010.

LIST OF PUBLICATIONS

1. Upendra Kumar Verma and Brijesh Kumar, "Charge transport in quantum dot organic solar cells with Si quantum dots sandwiched between poly(3-hexylthiophene) (P3HT) absorber and bathocuproine (BCP) transport layers", *Journal of Applied Physics*, 122, 0153104 (2017).

2. Upendra Kumar Verma, Aditya Nath Bhatt, and Brijesh Kumar, "Impact of capture/emission time constant at donor-acceptor interface on current-voltage characteristics of hybrid organic/inorganic quantum dot solar cells", *IEEE Electron Device Letters*, 39, 10, 1588 (2018).

3. Aditya Nath Bhatt, Upendra Kumar Verma, and Brijesh Kumar, "Temporal evolution of white light emitting CdS core and $Cd_{1-x}Zn_xS$ graded shell quantum dots fabricated using single step non-injection technique", *Optical Materials*, 92, 143 (2019).

4. Aditya Nath Bhatt, Upendra Kumar Verma, and Brijesh Kumar, "Size and shape dependent luminescence properties of trioctylphosphine (TOP) capped CdSe quantum dots", *JOSA B*, 36, 6, 1466 (2019).

5. Upendra Kumar Verma, Aditya Nath Bhatt, and Brijesh Kumar, "Tunneling rate controlled current-voltage characteristics of hybrid organic/inorganic quantum dot solar cells" (Under Preparation).

6. Upendra Kumar Verma, Aditya Nath Bhatt, and Brijesh Kumar, "Enhancement in Open Circuit Voltage by Introducing Cascaded Silicon Quantum Dot Layers in Multi-Layer Organic Solar Cell", *International Conference on Advanced Semiconductor Materials and Devices (ICASMD-2018),* March, 2018 organized by: C-MET, Hyderabad, INDIA, 2018.

7. Upendra Kumar Verma, Aditya Nath Bhatt, and Brijesh Kumar, "S-shape Current-Voltage Characteristics in Quantum Dot Integrated Multi-layer Organic Solar Cells", Electron Devices Technology and Manufacturing Conference **(EDTM-2020)** (Accepted).